INSTYTUT FIZYKI
WYDZIAŁ FIZYKI, ASTRONOMII
I INFORMATYKI STOSOWANEJ
UNIWERSYTETU JAGIELLOŃSKIEGO

Badanie korelacji kątowych w anihilacji orto-pozytonium przy pomocy detektora J-PET w celu poszukiwania łamania symetrii CPT.

Muhsin Mohammed

Praca doktorska

opiekun:

Prof. dr hab. Paweł Moskal– promotor,

dr Aleksander Gajos – promotor pomocniczy.

Kraków, 2020

INSTITUTE OF PHYSICS
FACULTY OF PHYSICS, ASTRONOMY
AND APPLIED COMPUTER SCIENCE
JAGIELLONIAN UNIVERSITY

Study of angular correlations in the ortho-positronium annihilation with the J-PET detector for the search of CPT symmetry violation

Muhsin Mohammed

Ph.D. Dissertation

Prof. dr hab. Paweł Moskal - Supervisor

dr Aleksander Gajos - Auxiliary supervisor

Kraków, 2020

Wydział Fizyki, Astronomii i Informatyki Stosowanej
Uniwersytet Jagiellonski

Oswiadczenie

Ja nizej podpisany Muhsin Mohammed (nr indeksu: 1105849), doktorant Wydziału Fizyki Astronomii i Informatyki Stosowanej Uniwersytetu Jagiellonskiego, oswiadczam, ze przedłozona przeze mnie rozprawa doktorska pt. ,, Study of angular correlations in the ortho-positronium annihilation with the J-PET detector for the search of CPT symmetry violation.'' jest oryginalna i przedstawia wyniki badan wykonanych przeze mnie osobiscie, pod kierunkiem prof. dr. hab. Pawła Moskala oraz dr. Aleksandra Gajosa. Prace napisałem samodzielnie.

Oswiadczam, ze moja rozprawa doktorska została opracowana zgodnie z Ustawa o prawie autorskim i prawach pokrewnych z dnia 4 lutego 1994 r. (Dziennik Ustaw 1994 nr 24 poz. 83 wraz z pózniejszymi zmianami). Jestem swiadom, ze niezgodnosc niniejszego oswiadczenia z prawda ujawniona w dowolnym czasie, niezaleznie od skutków prawnych wynikajacych z ww. ustawy, moze spowodowac uniewaznienie stopnia nabytego na podstawie tej rozprawy.

Kraków, dnia ....

Abstract

Testing the conservation of the CPT symmetry is one of the most important issues for modern physical science. CPT is the only combination of charge conjugation, parity, and time-reversal that is observed to be an exact symmetry of nature at the fundamental level. Several experiments are currently performed to test the symmetry in the leptonic sector, e.g. in neutrino oscillations. CPT can be tested also by using charged leptons by searching for the electric dipole moment, e.g. of the electron. In this thesis, we present a test of CPT invariance in the decays of positronium as the lightest purely leptonic bound system.

Positronium is a viable system for the investigation of possible violations of the discrete symmetries in the leptonic sector. We search for CPT-violating decay processes of positronium atoms by the Jagiellonian Positron Emission Tomograph (J-PET), using the angular correlation of $\vec{S} \cdot (\vec{k}_1 \times \vec{k}_2)$, where $\vec{S}$ is the positronium spin and $\vec{k}_1$, $\vec{k}_2$ are the momenta of the most energetic positronium decay photons. A non zero expectation value of CPT-odd angular correlation would give rise to an up/down asymmetry of the decay plane with respect to the spin orientation of the ortho-positronium atom. In the previous similar experiments, the precision of determining this kind of correlation has been limited to about 3‰. The precise experimental CPT symmetry tests with J-PET are possible thanks to a dedicated reconstruction technique of the ortho-positronium (o-Ps) into 3γ decays. The reconstruction of the o-Ps decay into three photons was used in order to determine the spin direction of the positronium atoms. Also, the identification of o-Ps decay into 3γ events as well as the reconstruction of their annihilation points was achieved using a large decay chamber with a layer of a highly porous material target silica (R60G) on its inner wall, whose setup allows for determining the o-Ps spin linear polarization without the use of external magnetic field. The measurements were performed with the J-PET by using two radioactive sources with different activities and two different kinds of annihilation chambers. We have measured the angular distribution of gamma quanta emitted in three-photons annihilation as a result of o-Ps decay.

The test of the CPT symmetry with J-PET detector resulted in the mean value of the CPT-sensitive angular correlation operator $O_{CPT} = (-5.5 \pm 3.7) \times 10^{-4}$, which corresponds to the CPT violation coefficient of $C_{CPT} = (-13.6 \pm 9.2) \times 10^{-4}$, therefore no violation has been found at the precision level of 9.2×10^{-4}, which is factor of 3 better than the previous experimental results.

Abstrakt

Testowanie zachowania symetrii CPT jest jednym z najważniejszych zagadnień dla współczesnej fizyki. CPT stanowi jedyną kombinację sprzężenia ładunkowego, parzystości oraz odwrócenia w czasie która wydaje się być fundamentalną symetrią w przyrodzie. Obecnie prowadzonych jest kilka eksperymentów sprawdzających tę symetrię w układach leptonowych, np. w oscylacjach neutrin. Symetria CPT może być testowana również poprzez poszukiwanie elektrycznego momentu dipolowego leptonów, np. elektronu. W tej pracy przedstawiony jest test symetrii CPT w rozpadach atomów pozytonium, stanowiących najlżejszy czysto leptonowy układ związany.

Pozytonium jest dobrym układem do poszukiwania możliwego łamania symetrii dyskretnych w sektorze leptonowym. W tej pracy poszukiwane są efekty łamania CPT w rozpadach pozytonium przy pomocy detektora J-PET, poprzez badanie korelacji kątowej $\vec{S} \cdot (\vec{k}_1 \times \vec{k}_2)$, gdzie $\vec{S}$ oznacza spin pozytonium a $\vec{k}_1$ i $\vec{k}_2$ to pędy dwóch najbardziej energetycznych fotonów powstałych w anihilacji orto-pozytonium. Niezerowa wartość średnia takiej korelacji, asymetrycznej względem transformacji CPT powinna objawiać się powstaniem asymetrii góra/dół pomiędzy płaszczyzną anihilacji oraz kierunkiem spinu atomu orto-pozytonium. W poprzednich eksperymentach dokładność wyznaczenia tej korelacji kątowej była ograniczona do około 3‰. Dokładne testy symetrii CPT przy pomocy eksperymentu J-PET są możliwe dzięki dedykowanej technice rekonstrukcji rozpadów o-Ps na trzy fotony, która została wykorzystana w celu wyznaczenia kierunku spinu atomów pozytonium. Rozpady orto-pozytonium na 3γ zostały zidentyfikowane i zrekonstruowane w pomiarach z użyciem dużej komory anihilacyjnej zawierającej warstwę krzemionki o wysokiej porowatości (R60G) na wewnętrznej ścianie. Taki układ pozwolił na otrzymanie liniowej polazyracji spinowej orto-pozytonium bez użycia zewnętrznego pola magnetycznego. Pomiary zostały wykonane przy pomocy detektora J-PET z wykorzystaniem dwóch źródeł promieniowania $\beta+$ o różnych aktywnościach. W pomiarach użyto również dwóch rodzajów komór anihilacyjnych. Zmierzone zostały rozkłady kątowe kwantów gamma powstałych w rozpadach orto-pozytonium na trzy fotony.

W teście symetrii CPT przy pomocy detektora J-PET wyznaczono wartość łamiącej symetrię CPT korelacji kątowej równą $O_{\mathrm{CPT}} = (-5.5 \pm 3.7) \times 10^{-4}$. Wartość ta odpowiada współczynnikowi łamania CPT równemu $C_{\mathrm{CPT}} = (-13.6 \pm 9.2) \times 10^{-4}$, zatem nie zaobserwowano łamania symetrii na poziomie dokładności 9.2×10^{-4}, trzykrotnie lepszym od wyników poprzednich eksperymentów.

Contents

Chapter 8

Chapter 9

Introduction

This work presents a test of the CPT symmetry performed using the J-PET detector by searching for non-vanishing angular correlations in the decays of ortho-positronium atoms originating from electron-positron interactions into three photons. To date, the CP and T symmetry violation was observed, while there was no observation of CPT violation. However, even in the case of CP and T where the symmetries were noted to be violated, the violation is only observed in systems involving quarks [1]. Therefore, searches for discrete symmetry violations in the leptonic sector are of great interest. So far a CP symmetry violation was not observed for purely leptonic systems (where its breaking symmetry has been observed in the decay of K and B meson) [1,2]. This thesis is focused on the study of a CPT-symmetry violating correlation in the annihilations of polarized ortho-positronium atoms, the lightest purely leptonic systems decaying into photons. Positronium has been recognized as a useful system for tests of the discrete fundamental symmetries CP, and CPT [3]. We choose this system in order to search for an asymmetry in the triple angular correlation $\vec{S} \cdot (\vec{k}_1 \times \vec{k}_2)$, where $\vec{S}$ is the spin of the ortho-positronium atom and k_1 and k_2 are the momenta of the most energetic decay photons, where $|\vec{k}_1| > |\vec{k}_2| > |\vec{k}_3|$. The sensitivity of CPT-odd triple correlation to CPT violation was demonstrated in Ref. [4]. The ortho-positronium atom annihilates mainly into three coplanar gamma quanta, which can be labeled E_1, E_2, and E_3 in order of their decreasing energy. The quantity $\vec{k}_1 \times \vec{k}_2$ defines a vector normal to the 3 photons decay plane.

One of the most fundamental symmetries in physics is CPT invariance. The test of CPT violation acquires its importance as a test of various foundations of physics and basic laws of physics, and the result of such test may either support the essentials of physics further, or they may reveal fundamentally a new physics.

The experiment was performed using the J-PET detector at the Jagiellonian University. The J-PET detector consists of 192 plastic scintillator strips surrounding a 12 cm radius annihilation target chamber.

The experiments were done in the frame of working with the J-PET group. The author took an active part in all experimental measurements, mechanical assembly and experimental setup of the J-PET equipment, tests, and the calibrations of the J-PET detector. The measurements, in which the author of this thesis took part, were performed in January 2017, June-September 2018, and March-April 2019 at Jagiellonian University by means of J-PET detector. The higher levels of the data analysis modules were written in the C++ language by the author using the J-PET framework software. All the analysis of data of the measurements presented in this work was performed by the author, which includes the refined time calibration and obtaining the o-Ps annihilation points and the reconstruction of the first tomographic images. Finally, the analysis of the uncertainties, the extraction of the CPT violating coefficient C_{CPT}, and a comparison of the CPT test's precision results with those which were obtained in previous experimental studies was also performed by the author.

This dissertation is organized into nine chapters. The first chapter serves as an introduction to the subject of discrete symmetries and CPT symmetry violation. Chapter 2 introduces the reader to the main properties of the positron and positronium atom which is a key aspect of this work. Chapter 3 describes the theory and principles necessary to understand the positronium polarization methods. Description of my

research begins in Chapter 4, which gives a technical explanation of the J-PET detector apparatus equipment and software. Chapter 5 contains a detailed explanation of the methods of preparation of the positronium source and annihilation chambers and represents a description of the measurements presented in this work. Chapter 6 discusses the J-PET calibrations and describes all the calibrations which have been done before and after measurements. Chapter 7 includes discussions about the methods of data analysis and image reconstruction. Chapter 8 contains results, conclusions, which included the CPT symmetry violation test by J-PET, the results of studying the angular distribution of photons in o-Ps to three-photon decay, as well as a comparison with the previous experimental results. It also describes the sources of the systematic uncertainties in the measurements of the angular correlation operators for CPT symmetry test. The last chapter serves for the conclusions and the prospects on how to progress with the J-PET to increase the CPT test precision and opens the discussion about the limitations of the study and also includes an overview of opportunities for further researches.

1. The discrete symmetries

The three kinds of discrete symmetries of quantum mechanics, C (charge conjugation), P (parity inversion), and T (time reversal) are all violated in nature, both singly or in pairs. CPT symmetry (in any order) is the only combination of these three symmetries which appears to be conserved as an exact symmetry of nature.

The most interesting fact is that (since the matter is made of quarks and leptons) the violation of CP and T discrete symmetries has, so far, been only discovered for systems including quarks, and it has not yet been observed in any processes involving purely leptonic system.

One can use for example the neutrinos, but it is a completely different kinds of experiments requiring very big detectors and a long time of measurements. There is also the electric dipole moment for leptons, where the electron is most accessible to experimental observation, but it is also indirect search for CPT violation and it is worth also to study the positronium which is the lightest system composed of charged leptons. Such kind of experimental studies are interesting and the best so far performed experiments with positronium atoms excluded a violation of discrete symmetries as CP, T or CPT only at the level of precision of about 3×10^{-3} which was obtained by the Gammasphere detector [5], this result in fact many orders of magnitude less precise than the precisions which have been achieved in the CP symmetry violation studies in the case of quark sector. The latter result still about six orders of magnitude larger than the possible contribution from the radiative corrections which may mimic the CPT symmetry violation at the level of 10^{-9} [6,4].

1.1. Charge conjugation, parity, Time reversal, CP, and CPT symmetries

Quantum electrodynamics (QED) Lagrangian is invariant under charge conjugation symmetry (C), where Charge conjugation is a transformation that switches all the particles in the system with their corresponding antiparticles, which means changes the sign of all charges. Therefore, in the case of pure QED description of Ps decays, the annihilation into an even number of photons is allowed in the case of p-Ps, whereas o-Ps can decay into an odd photons number. According to the Landau-Yang theorem, the o-Ps decay into 2 photons is forbidden, therefore the simplest possible decay violating C-symmetry is the p-Ps into 3 photons. One of the possibilities of looking for a symmetry violation is studying angular correlations, and the angular correlations can be expressed by certain operators [4]. A whole set of these operators presented in Table 1.1. The combination of two discrete symmetries (the parity transformation, and the charge conjugation) and also the three discrete symmetries combination for the decay of o-Ps into 3 photons were investigated and tested by determination of expectation values of the second and third operators presented in Table 1.1. The upper limits on CP [3] and CPT [5] symmetry violation in the annihilation of ortho-positronium:

$C_{CP} = 0.0013 \pm 0.0022$; [3] for the operator $\left(\vec{S} \cdot \vec{k}_1 \right) \left(\vec{S} \cdot \left(\vec{k}_1 \times \vec{k}_2 \right) \right)$

$C_{CPT} = 0.0071 \pm 0.0062$; [5] for the operator $\vec{S} \cdot \left(\vec{k}_1 \times \vec{k}_2 \right)$

Table 1.1. Properties of operators for the o-Ps into 3γ decay for given symmetries. $\vec{k}_1$ and $\vec{k}_2$ denote the momentum of the most energetic decay photons, $\vec{S}$ is the spin of the o-Ps. The symmetry-odd operators available for studies at the J-PET [7] system are highlighted in blue color.

Operator	C	P	T	CP	CPT
$\vec{S}\cdot\vec{k}_1$	+	−	+	−	−
$\vec{S}\cdot(\vec{k}_1\times\vec{k}_2)$	+	+	−	+	−
$(\vec{S}\cdot\vec{k}_1)(\vec{S}\cdot(\vec{k}_1\times\vec{k}_2))$	+	−	−	−	+
$\vec{k}_2\times\vec{\epsilon}_1$	+	−	−	−	+
$\vec{S}\cdot\vec{\epsilon}_1$	+	+	−	+	−
$\vec{S}\cdot(\vec{k}_2\times\vec{\epsilon}_1)$	+	−	+	−	−

The experimental limits on the symmetries violation of CP and CPT in the positronium decays are still several orders of magnitude higher than the effects mimicking the violation. Therefore, there are at least 6 orders of magnitude level for the possible precision test of CPT symmetry violation taking into account a predicted level of final-state interactions.

So far only the weak interactions were found to violate symmetries under the P [8], C [9] and T operators [10]. As shown in Figures 1.1, 1.2 and 1.3 respectively:

The experiment of Wu et al. [8] involved beta particles emitted from cobalt-60 nuclei oriented using a strong magnetic field so their spins aligned in the same direction. The experiment measured the direction in which these beta particles were emitted relative to the spin of the Cobalt-60 nuclei. In the mirror image version of the experiment, the direction of the z-axis was flipped, but the direction of nuclear spin was not because they rotating clockwise in the real is still rotating clockwise in the mirror, so the spin of the nuclei are aligned in real and mirror. When the Cobalt-60 decays and emits beta particles, parity conservation demands that the emitted beta particles should be equally distributed between the two directions along the z-axis, and based on that real and the mirror experiments would give the same results, but beta-particles are emitted preferentially in the direction opposite to the nucleus spin. The mirror world is thus distinguishable from the real world. The parity-transformed world is not identical to the real world, which would be tantamount to parity violation as shown in Figure 1.1. In the case of the mirror experiment, an additional to flipping the direction of the z-axis, if the particles swapped to anti-particles with their charges, then the symmetry would be restored again.
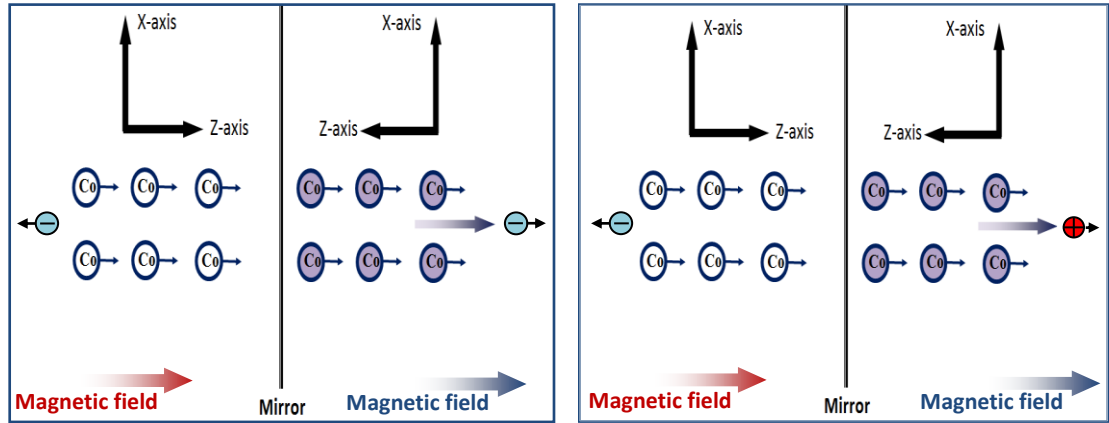
Figure 1.1: Left: The P symmetry violation example in the weak decay interaction (^{60}Co decay). Right: The combined CP symmetry, where the process of the beta+ emission would conserve the symmetry.
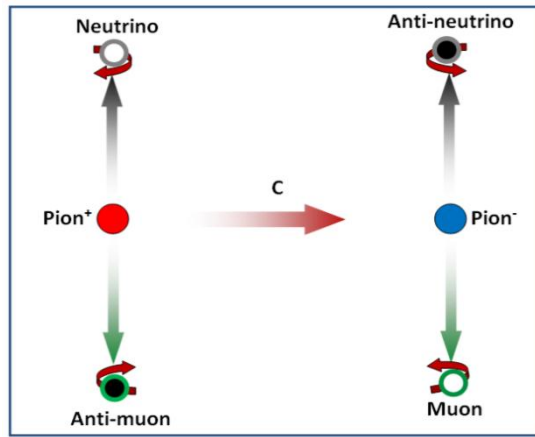
Figure 1.2: The C symmetry violation example, where a positively-charged pion decays into an anti-muon and a neutrino, the neutrino spin is always left-handed and impossible to be right-handed, which violates the parity. While, when a negatively-charged pion decays into a muon and an anti-neutrino, the anti-neutrino spin is always right-handed. The difference between the two processes involving negatively and positively charged pions violates C-symmetry.

The physicists conducted experiments to confirm that certain particles directly violate the time symmetry, for example when a pair of quarks are held together by the strong force, there are some times two different possible arrangments and they can switch back and forth between these two arrangements via the weak force, but switching in one direction takes longer time than switching back, so if it is possible to make a recording of this event, it would look different if would play the recording forwards than if it has been played backwards as shown in Figure 1.3 in certain cases then

fundamental particles can show the difference between going forward and backward in time.
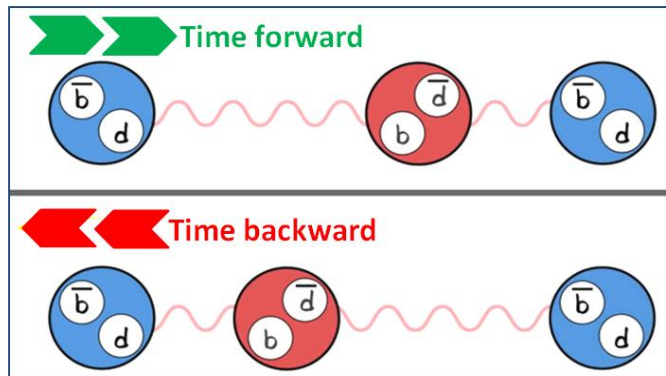
Figure 1.3: The T symmetry violation example in the case of botton and down quarks under the effect of the strong force.

2. Properties of positron and positronium

2.1. The positron

The positron or antielectron is the antiparticle or the antimatter counterpart of the electron. The positron has an electric charge of +1 e, a spin of 1/2 (same as an electron), and has the same mass as an electron. It is a stable particle in the vacuum with a mean lifetime of more than 2 x 10^{22} years [11]. The existence of the positron was predicted in 1928 by physicist Paul Dirac, and positrons were discovered experimentally in 1932 by physicist Carl Anderson.

Positrons may be generated by radioactive decay (through weak interactions), (see Figures 2.1 and 2.2), or by pair production from a sufficiently energetic photon which is interacting with an atom in a material. It is a form of antimatter because, when a positron collides with an electron, the two may completely annihilate resulting in the emission of two or more gamma-ray photons, which due to energy conservation, must have a total energy equal to the rest mass energy (i.e. 1.022 MeV) plus any kinetic energy of the positron-electron pair.

The number of gamma-rays that are emitted is determined by the parity and charge quantum numbers of the annihilating system, which must be conserved. For a system containing n gamma-rays, the charge conjugation eigen value reads:

$$Pc = (-1)^n \tag{2.1}$$

and for the electron-positron system:

$$Pc = (-1)^{L+S}, \tag{2.2}$$

where L is the orbital angular momentum of the electron-positron system and S is its spin [12]. Therefore, an odd or even number of gamma-rays is released through annihilation depending on the spin and angular momentum of the positron-electron pair.
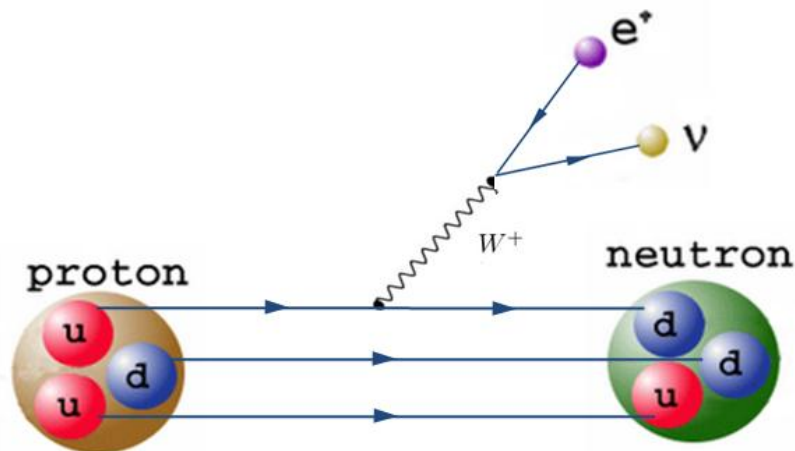
Figure 2.1: Scheme of a beta+ decay.
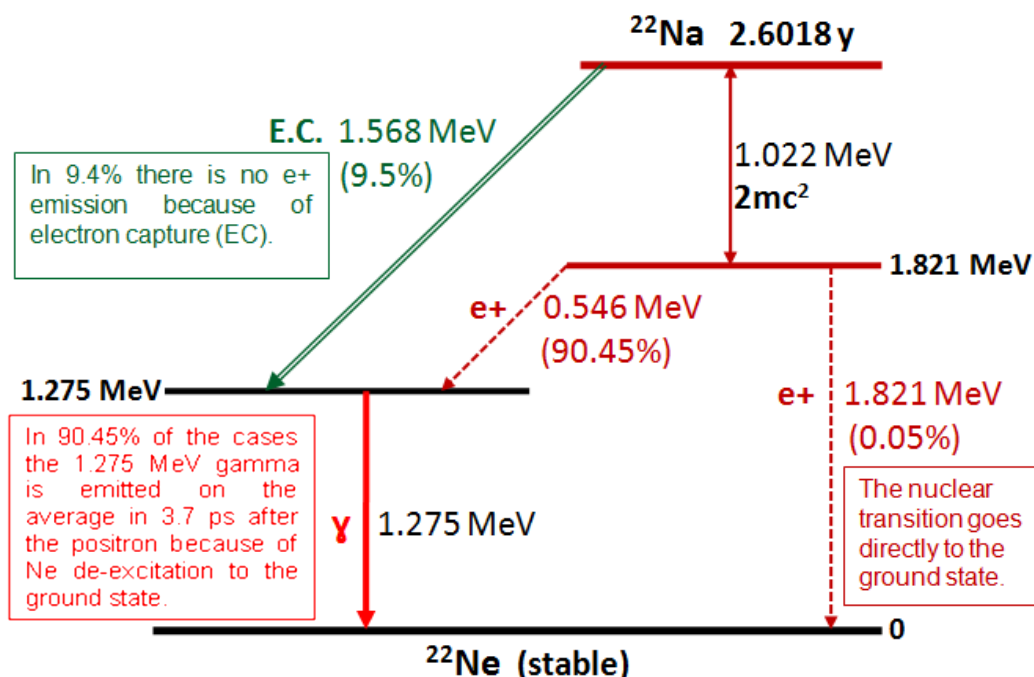
Figure 2.2: Decay scheme of the [22]Na radioisotope, where a positron with an end-point energy of 546 keV is emitted in 90.45% of the decay reactions, which first produces excited neon [22]Ne and then ground-state neon by the emission of a photon (1.275 MeV). 9.5% of the decay events happen by electron capture (EC) and then photon emission, while a very small fraction (0.05%) occurs by the emission of high-energy positrons (1.821 MeV). The accompanying neutrino emission is not shown in this decay scheme.

2.2. The positronium atom

Positronium (Ps) is a system consisting of an electron and its anti-particle, a positron, bound together into an exotic atom. The system is a metastable hydrogen-like bound state of an electron and a positron which can exist in two spin states. Para-positronium, p-Ps, (spin equal to zero) is a singlet ground state with a characteristic self-annihilation lifetime of 125 ps in vacuum [13]. Ortho-positronium (o-Ps) is a triplet ground state (spin equal to 1) with a characteristic self-annihilation lifetime of 142 ns in vacuum. In molecular materials, the lifetime of o-Ps is environment dependent and it delivers information pertaining to the size of the void in which it resides. Ps can pick up a molecular electron with an opposite spin to that of the positron, leading to a reduction of the o-Ps lifetime from 142 ns down to even 1-4 ns (depending on the size of the free volume in which it resides) [13]. The size of the molecular free volume can be derived from the o-Ps lifetime via the semi-empirical Tao-Eldrup model [14]. The Ps-atom was first experimentally detected by Deutsch 1951 [15].

2.2.1. Positronium properties (Fundamental properties of positronium)

This chapter gives an elementary introduction to the most important properties of positronium (see Table 2.1). It is not intended as a comprehensive review which can be found e.g. in [16,17]. Positronium, is an electron-positron bound state, which is the lightest known atom so far. This feature offers unique opportunities for testing our understanding of bound-states in the framework of Quantum Electrodynamics (QED). The spins of the electron and the positron in the positronium can combine to give either a singlet spin ground state $^1S_0$ which is called para-positronium or a triplet ground state $^3S_1$, ortho-positronium. The system is unstable: the two particles annihilate each other and predominantly produce two or three gamma-rays, depending on the relative spin states. The orbit and energy levels of the two particles are similar to that of the hydrogen atom (which is a bound state of a proton and an electron) (see Figure 2.3). However, because the positronium reduced mass is about half of that of a hydrogen atom, the frequencies of the spectral lines are less than half of the corresponding lines of the hydrogen atom.

Table 2.1: The comparison of positronium (Ps) and hydrogen atom.

Hydrogen atom	Properties	Positronium
1.0080	Atomic mass (amu)	0.00110
0.99946	Reduced mass (a.u.)	1/2
0.53 A° (radius)	Size, <r>	1.06 A° (radius)
13.598 eV = 0.5 a.u.	Ionization energy	6.803 eV = 0.25 a.u.
paramagnetic	Magnetism	diamagnetic
$1/\pi$	Contact density	$1/8\,\pi$
1s, 2s, 2p, ..., (n, m, I)	Spatial states	1s, 2s, 2p, ..., (n, m, I)
5.9 μeV	Hyperfine splitting	840 μeV
4.5 a.u.	Dipole polarizability	36 a.u
J = 0 (para) J = 1 (ortho)	Spin states	S = 0 (para) S = 1 (ortho)
Stable	The lifetime	0.125 ns (para) 142ns (ortho)
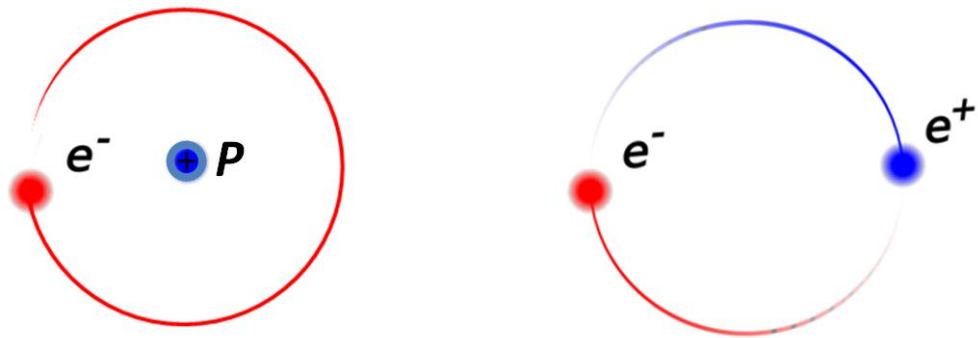
Figure 2.3: Scheme of the hydrogen atom (left) and positronium (Ps) atom (right).

2.2.1.1. Positronium decay rates

Positronium atom consists of an electron and a positron orbiting around each other. p-Ps is formed with an electron and a positron with total spin equal to 0 and in its ground state it has a lifetime in vacuum of 125 ps, decaying predominantly into two 511 keV gamma-rays emitted back-to-back (BTB). The o-Ps is formed with an electron and a positron with total spin equal to one and has a lifetime in the vacuum of 142 ns in its ground state, decaying predominantly into three coplanar gamma-rays with energies from zero to 511 keV. Measuring these annihilation decay rates provides unique tests of quantum electrodynamics (QED) [18].

The Positronium atom annihilates into n gammas, with n restricted to even or odd by equations (2.1) and (2.2), which yield: $(-1)^n=(-1)^{L+S}$, where S is the total spin and L is the angular momentum of the positronium. The characteristics of the two Ps spin states are given in Table 2.2. Due to spin statistics, positronium is formed in a ratio of ortho-positronium (o-Ps) to para-positronium (p-Ps) of 3:1. Thereby, upon the production and annihilation of ground-state of positronium, 3 gamma are more likely produced [19].

Table 2.2: The properties of positronium ground-state: a [20], b [21], c [22], d [23].

Name	State S	Sub state S_z	Mean life-time	Decay mode	Ground state decay rates (μs^{-1})	
					Experiment	Theory
p-Ps	0	0	125 ps	2γ	7990.9+ 1.7[a]	7989.5[b]
o-Ps	1	-1,0,+1	142 ns	3γ	7.0404(10)(8)(140ppm)[c]	7.0420[d]

2.2.1.1.1. Para-positronium

Except for the C-violating mode which are caused by the weak interactions, p-Ps can only annihilate into an even number of photons (see Figure 2.4).
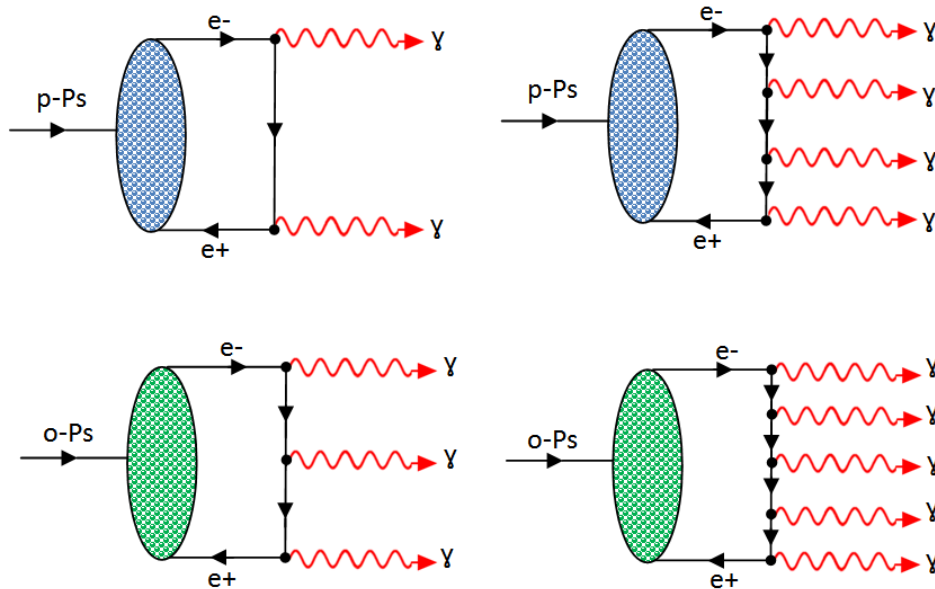
Figure 2.4: The Feynman diagrams of the p-Ps and o-Ps atoms decay modes.

The 2-γ decay rate of the p-Ps ground state, $^1S_0$, was calculated by Czarnecki et al. [24]:

$$\Gamma(p - Ps \to 2\gamma) = \frac{a^5 m_e}{2}\left[1 - \left(5 - \frac{\pi^2}{4}\right)\frac{\alpha}{\pi} + 2\alpha^2 \ln\frac{1}{\alpha} + 1.75(30)\left(\frac{\alpha}{\pi}\right)^2\right.$$

$$\left. - \frac{3\alpha^3}{2\pi} ln^2 \frac{1}{\alpha} + O\left(\alpha^3 ln\frac{1}{\alpha}\right)\right] = 7989.50(2)\mu s^{-1} \tag{2.3}$$

Here, α is the fine-structure constant and m_e is the electron mass. Where the non-logarithmic terms $O(\alpha^2)$ [24] and leading-logarithmic terms $O(\alpha^3 \ln^2 \alpha)$ have been obtained [25].

The theoretical prediction agrees well with the experiment [20],

$$\Gamma_{exp}(p - Ps \to 2\gamma) = 7990(1.7)\mu s^{-1} \tag{2.4}$$

The 4γ decay is highly suppressed relative to 2γ and the branching ratio for these decays amounts to [26]:

$$BR(p - Ps \to 4\gamma) = \frac{\Gamma(p-Ps\to4\gamma)}{\Gamma(p-Ps\to2\gamma)} = 0.277(1)\left(\frac{\alpha}{\pi}\right)^2 \cong 1.49 \times 10^{-6} \tag{2.5}$$

2.2.1.1.2. Ortho-positronium

The more difficult calculation for the lowest order decay rate of the triplet spin state of orthopositronium atom (o-Ps) was first obtained correctly by Ore and Powell [27] in 1949. Their result can be expressed as:

$$\Gamma^0_{3\gamma} = \frac{2}{g}(\pi^2 - 9)\frac{\alpha^6 . m_e}{\pi} \tag{2.6}$$

$$\Gamma^0_{3\gamma} = 7.2111670(1)\ \mu s^{-1} \tag{2.7}$$

The ground state of orthopositronium, $^3S_1$, can decay into an odd number of the photons only (if *C* is conserved) (see Figure 2.4). The three gamma decay rate is given by:

$$\Gamma(o - Ps \to 3\gamma) = \frac{2(\pi^2 - 9)a^6 m_e}{9\pi}\left[1 - 10.28661\frac{\alpha}{\pi} - \frac{a^2}{3}\ln\frac{1}{\alpha} + B_o\left(\frac{\alpha}{\pi}\right)^2\right.$$

$$\left. - \frac{3\alpha^3}{2\pi}ln^2\frac{1}{\alpha} + O(\alpha^3 \ln \alpha)\right] \cong (7.0382 + 0.39 \times 10^{-4} B_o)\mu s^{-1} \tag{2.8}$$

Because of its 3-body phase space and a large number of diagrams, a complete theoretical analysis of o-Ps decays is much more difficult than in the case of p-Ps. The non-logarithmic two-loop effects, parameterized by B_o, have not been evaluated so far, and more theoretical correction is needed.

The 5γ decays branching ratio is of order α^2 [26,28]:

$$BR(o - Ps \rightarrow 5\gamma) = \frac{\Gamma(o-Ps\rightarrow5\gamma)}{\Gamma(o-Ps\rightarrow3\gamma)} = 0.19(1)\left(\frac{\alpha}{\pi}\right)^2 \cong 1.0 \times 10^{-6} \qquad (2.9)$$

2.2.2. Positronium interactions with the medium (environment)

In the presence of matter or in external electric (E) or magnetic (B) fields, the ortho-positronium states may annihilate into two gamma photons. Several mechanisms are responsible for this effect and in this section, they will be briefly discussed. In a material with a random orientation of spins, 3/4 of positronium atoms are formed in the triplet state and the remaining 1/4 is para-positronium (see Figure 2.5). Usually, the interaction which is called free annihilation of an o-Ps atom produces 3ɣ. Based on the quantum electrodynamics, the probability of 3ɣ-annihilation is much smaller than that of 2ɣ-annihilation but the spin conservation rule prevents the occurrence of 2ɣ-annihilation from a spin S = 1 state. Thus the self-annihilation of o-Ps is a relatively slow process and ortho-positronium atoms have enough time to take part in different interactions with the atoms of the surrounding environment. As a result, o-Ps commonly escapes self-annihilation because it is forced by its surroundings to undergo quick 2ɣ-annihilation [29] (see Figure 2.5).
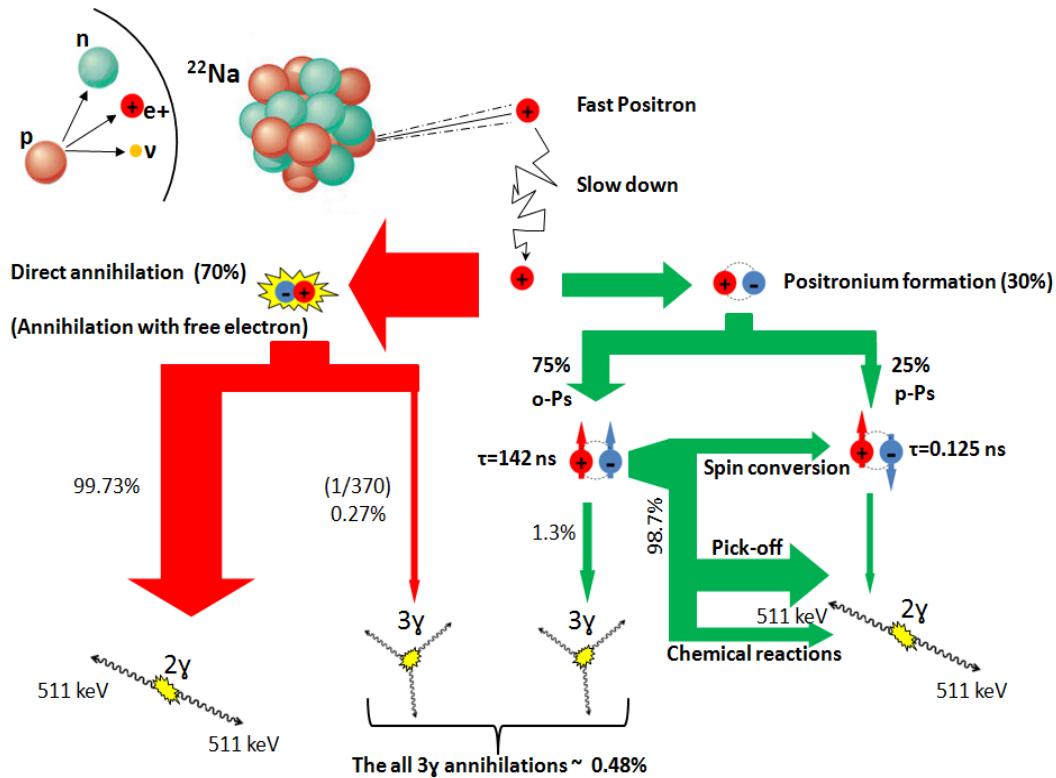
Figure 2.5: The scenarios scheme for all the possible annihilation processes of the positronium in water [13].

2.2.2.1. The pick-off annihilation process

The most general interaction between Positronium and materials is the so-called pick-off annihilation. It occurs in every material, although sometimes together with other o-Ps interactions. This interaction results from the fact that the positron of the triplet positronium atom o-Ps can undergo annihilation with an electron of a colliding molecule rather than with the electron that is part of the positronium atom (see Figure 2.6). Thus the positron-electron pair, that annihilates at the end, is predominantly in a singlet state (S = 0) instead of the o-Ps original (S=1) state. When o-Ps collides with a closed-shell atom or ion, the pick-off process is the dominant process for positron annihilation because of the fact that in the presence of matter the positron wave function may overlap with an electron of the surrounding media. Therefore, there is a high probability that the positron annihilates with an electron which is not its bound partner. The o-Ps annihilation by the pick-off mechanism will predominantly emit two gamma rays in the same way as annihilating p-Ps. Pick-off annihilation will, therefore, decrease the o-Ps lifetime in the material and diminish the maximum fraction of o-Ps that can self annihilate (see Figure 2.6).
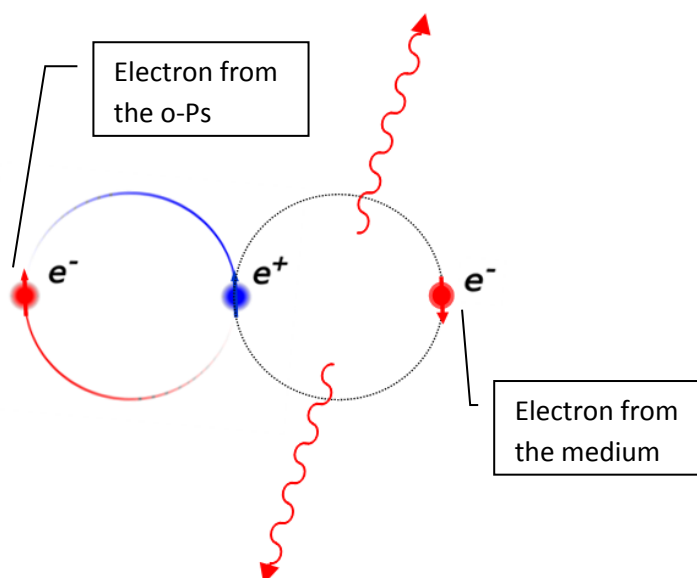
Figure 2.6: The pick-off annihilation process scheme.

As a result of this interaction, the lifetime of ortho-positronium shortens considerably but, owing to the shielding effect of the Ps-electron, it is still longer than it would be in the case of free e^+e^- annihilation (direct annihilation). Pick-off annihilation is especially common in condensed phases. The rate of pick-off annihilation varies with the material type, with the rate being higher for metals and semiconductor materials. Additionally, the pick-off rate changes with the dimension of the pore size and presently the research indicates that the rate decreases with increasing pore diameter [30]. The decay rate through pick-off is much lower than expected from the average electron density of the material in which the Ps forms. This is due to the repulsive electron exchange interaction between the Ps and the surrounding atoms.

2.2.2.2. The spin conversion process (Spin exchange mechanism)

The second important interaction of positronium is the ortho-para spin conversion. It occurs if the substance contains paramagnetic particles with unpaired electrons. When colliding with such a particle, the orientation of one of the parallel spins of ortho-positronium may be reversed simultaneously with the reversion of the spin of the unpaired electron of the colliding molecule. This interaction takes place via electron exchange between the molecule and o-Ps atom (see Figures 2.7 and 2.8). The para-positronium formed by this process annihilates very rapidly, according to its short mean lifetime. Consequently, this effect also leads to drastic decrease in the effective lifetime of positronium. Ortho-para conversion can be demonstrated by the following example reaction [29]: $Ps(\uparrow\uparrow)+NO(\downarrow)\rightarrow NO(\uparrow)+Ps(\uparrow\downarrow)\rightarrow NO(\uparrow)+2\gamma$, where NO is nitrosonium ion and the vertical arrows show the directions of the spin.

The converters are often an atom or molecule that have one or more unpaired electrons (free radicals) and transition metal ions having unpaired electrons. The prominent feature of radicals is that they have extremely high chemical reactivity, however, there is no correlation between the number of unpaired electrons and the strength of the converter. Moreover, it was experimentally verified, that the statistical probability of the ortho-positronium into para-positronium conversion reactions (CR) caused by the paramagnetic compounds with spin $S = 1/2$ is three times larger than that of the CR caused by compounds with $S > 1/2$ [31]. The Ps atom can undergo a spin conversion reaction with paramagnetic material without the necessity of any kind of change in the spin state of the latter [32]. Due to the spin states statistics, after interacting with the odd electron of a solute molecule or ion, the Ps atom (whether singlet or triplet) has normally 3 chances out of 4 to become o-Ps, and 1 out of 4 to be found as p-Ps, because p-Ps has much shorter lifetime compared to that of o-Ps, this processes transform a large part of o-Ps into p-Ps (see Fig. 2.7).
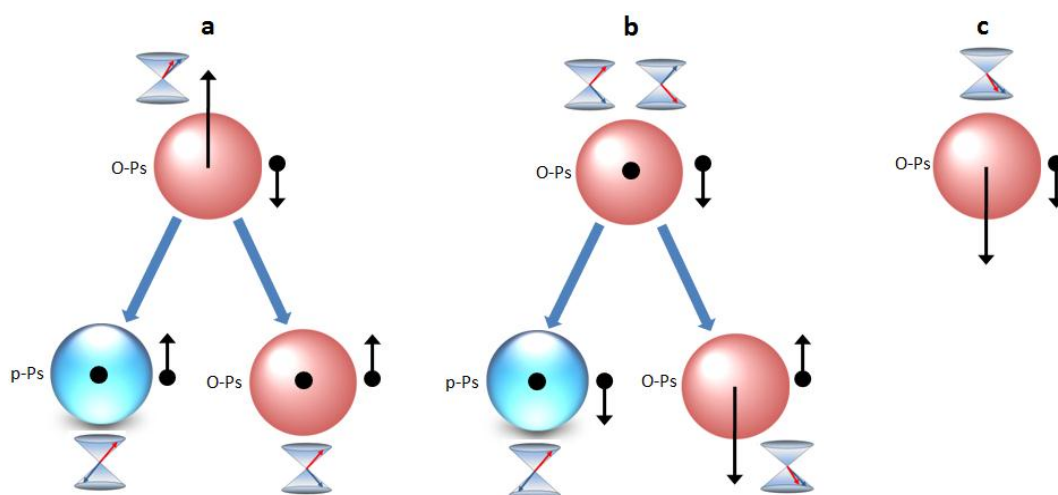
Figure 2.7: Spin-conversion of the o-Ps with an electron of spin down (black small arrow pointing down) : a) the o-Ps (red) with the spin projection $S_z = +1$ can convert either into the p-Ps (blue) or into the o-Ps with $S_z = 0$; b) the o-Ps with $S_z = 0$ can convert either into the p-Ps with $S_z = 0$ or into the o-Ps with $S_z = -1$; c) the o-Ps with $S_z = -1$ cannot convert with an electron with spin pointing down.
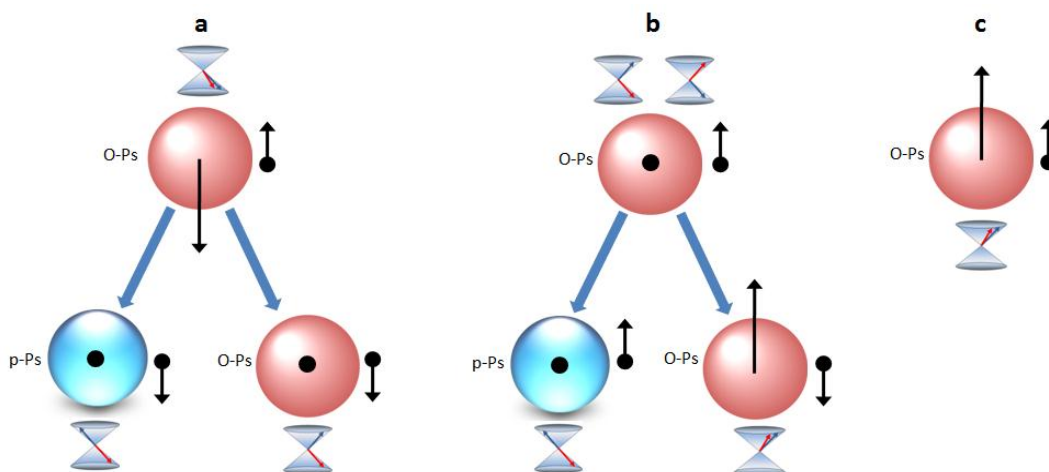
Figure 2.8: Spin-conversion of the o-Ps with an electron of spin up (black small arrow pointing up) : a) the o-Ps (red) with the spin projection $S_z = -1$ can convert either into the p-Ps (blue) or into the o-Ps with $S_z = 0$; b) the o-Ps with $S_z = 0$ can convert either into the p-Ps with $S_z = 0$ or into the o-Ps with $S_z = 1$; c) the o-Ps with $S_z = 1$ cannot convert with an electron of spin pointing up.

2.2.2.3. The Positronium chemical reactions

The positronium reactions are often described simply as "pick-off" or "spin-exchange" interactions which convert o-Ps to p-Ps following the formation of a reaction complex, but many studies verified that the positronium atom can participate in different kinds of the chemical reactions [33].

Despite the aforementioned similarity of positronium to hydrogen atom, there is also a number of important differences. Where the hydrogen atom is a simplest and smallest free radical, as it has an unpaired electron spin, o-Ps is a kind of biracial, as it has a total electron and positron spin =1, while p-Ps exhibits no unpaired spin. Moreover, the distribution of charge in the positronium atom is much more delocalized than that of the hydrogen atom. Also the effective distance between electron and positron in the positronium atom is about twice of that between electron and proton in the hydrogen atom.

It should be noted that certain types of ortho-para positronium conversion reactions, e.g. the interaction with radicals, are also of chemical character. The most important types of positronium chemical interactions can be demonstrated by the following examples [34]:

a. Addition reactions: $Ps + O_2 + M \rightarrow PsO_2 + M$, were addition of positronium to oxygen in the presence of an inert atom or molecule M.

b. Exchange reactions: $Ps + Cl_2 \rightarrow CI + PsCl \rightarrow Cl_2 + 2\gamma$, this chemical interaction include distinction capture and separation of the positronium by halogens like fluorine (F),

chlorine (Cl), bromine (Br), iodine (I), and astatine (At). The bond dissociation energy of positronium and Chlorine molecule (PsCl) is estimated to be about 0.8, 1.6 eV. This chemical reaction has been studied by using the angular correlation technique, where the rate constant is about 4×10^{-9} cm^3/sec. This rate constant value is 30 times greater than the rate constant of the analogous reaction with hydrogen atom [35].

c. Oxidation reactions: $Ps + Fe3^+ \rightarrow Fe2^+ + e^+ + 2\gamma$, where $Fe3^+$, $Fe2^+$ are Ferric ions.

d. Reduction reactions: $Ps + e- \rightarrow Ps- \rightarrow e- + 2\gamma$, Positronium can be further bind to another electron to form the positronium negative ion, $Ps-$ ($e-e+e-$), where it's existence has been confirmed [36].

The common conclusion of such chemical reactions is that Positronium atom senses a medium with more free electrons. This leads to its annihilation similar to the pick-off annihilation. The outcome is a shortened lifetime and an annihilation into two gamma quanta. In the case of benzoquinone, Ps may attack the carbonyls or the ring C=C groups to form such complexes. The previous studies was verified that the positrons react with nitrates [37], it is believed that this reaction is an oxidation process. It is found also that positronium is less readily attacked by the ions like Cl^- and $SO4^{--}$ [30].

In the sulfate and chloride solutions, the positronium atom more effectively replaces the metals which are lowest in the electrochemical series. A systematic study of the chemical properties of the positronium atom was done by McGervey and DeBenedetti [32] who verified that the positronium has an oxidation chemical reaction with nitrates.

2.2.2.4. Positronium quenching in magnetic fields

The ortho-positronium, which decay into 3γ can undergo quenching through various types of interactions with atoms and molecules. The quenching process of o-Ps could happen during o-Ps-atom collisions via pick-off quenching, chemical quenching (see Figure 2.5), spin conversion quenching through an exchange of electron and spin conversion quenching process through a spin-orbit interaction with a heavy atom, another possibility for annihilation is o-Ps→p-Ps conversion due to the spin-orbit interaction between the atom and colliding Ps. This extra quenching mechanism may explain a number of phenomena observed in the annihilation spectrum of Kr and Xe, including the very small Ps fraction of 3% seen for Xe [38].

A similar quenching of o-Ps to p-Ps (and vice versa) is caused by the presence of a magnetic field. The triplet state with $S_z = 0$ can mix with the singlet state resulting in a reduction of the observed decay rate of o-Ps. The triplet states of o-Ps with $S_z = \pm 1$ are not affected by the magnetic field, therefore, the maximum reduction in the o-Ps fraction is 1/3 [39].

The application of a sufficient external magnetic field causes the mixing of para-positronium and ortho-positronium energy states of the Ps atom with quantum number $S_z=0$, resulting in the decrease of the longest-lived o-Ps component in the positronium lifetime spectrum. Rochanakij and Schrader [40] have studied the effect of an external magnetic field on the lifetime of positronium atom in different kinds of liquids and solutions. Applying a steady magnetic fields up to 1.4 Tesla by using the positron annihilation lifetime technique, the lifetime of o-Ps with $S_z=\pm 1$ remains constant as the case before the field was applied, and the lifetime of o-Ps with $S_z=0$ was very sensitive to the strength of the external magnetic field, and it is decreasing as the field strength increases. This effect follows from a well-known principle of atomic physics, the magnetic quenching mechanism, the quadratic Zeeman effect [33], where an important information on the structure of Ps can be obtained through the Zeeman effect.

3.The positronium polarization

Positronium atoms may be created with different spin configurations which determine their fundamental properties, such as energy level structure, lifetime, decay rate and response to an external magnetic field. The nature of the interactions between Ps atoms is also strongly influenced by their energy and relative spin states; oppositely polarized Ps atoms may interact and exchange particles and scatter into different energy states, or join together to form molecular positronium. The positron beams derived from radioactive material are always spin-polarized to some extent and have been used for a lot of applications, for instance, measuring the magnetic properties of ferromagnets, and studying different fundamental interactions. It has been known for many years that a fully spin-polarized positronium atom is the best candidate to form and observe Bose-Einstein condensation in such fermionic system since it has low mass [41]. Many applications with positronium Bose condensate are expected, such as the realization of a 511 keV gamma-ray laser via coherent decays of positronium Bose condensate [42,43] and also a measurement of the effect of gravity on a positron with high precision by using an atomic interferometer [44].

3.1. The linear polarization of the ortho-positronium

The positrons emitted from ^{22}Na radioactive source are longitudinally spin-polarized due to the parity non-conservation in the weak interaction. The positron has polarization vector equal to $\vec{P} = \vec{v}/c$, where $\vec{v}$ denotes the velocity of the positron and c is the speed of light. In the gamma-sphere experiment [5], the linear polarization of the ortho-positronium atom was evaluated statistically by allowing o-Ps to be formed in a single target hemisphere of silicon dioxide aerogel around a point-like positron source located in the center of the sphere, then the linear polarization was estimated along a fixed quantization axis. The unique characteristics, geometry and properties of the J-PET scanner enable the design of a positronium source such that the polarization vector of emitted ortho-positronium atom can be determined [45].

For the J-PET experiment, we are able to estimate the positronia spin direction as shown in Figure 3.1. Using J-PET scanner allow us to study the spin linear polarization of the positrons forming o-Ps atoms, where the linear polarization is estimated on an event-by-event basis [7], instead of the assumption of fixed quantization axis throughout the measurements. The thin layer of porous material is placed on the inner walls of the cylindrical annihilation chamber bombarded with positrons emitted from the beta+ source located in the geometry center of the J-PET scanner. The produced ortho-positronium atoms which annihilate into three photons for which time and position of their interactions is recorded in the plastic scintillator strips of the J-PET detector enable to reconstruct the exact position of annihilation point using the trilateration method. The trilateration-based reconstruction method details were introduced in references [46,47].

A trilateration reconstructing method allows us to determine the direction of positron propagation in a single event with a vector spanned between a point-like source location and the reconstructed annihilation point of the ortho-positronium atom. The trilateration reconstruction method is shown in Figure 3.1. The ortho-positronium

does not displace too far during its lifetime so that its annihilation point is approximately the same as creation point and, hence, the direction of the spin of the positron. The tests performed with Monte Carlo simulations assuming 80 ps time resolution of the J-PET detector have shown that this method is able to reconstruct the o-Ps annihilation point with the spatial resolution of about 2 cm and the annihilation time with the resolution of about 0.1 ns [46], also the o-Ps atoms annihilations into two and three photons can be well separated using such method as described in Section 7.8. Reconstruction of ortho-positronium decays in J-PET detector is based on the trilateration technique similar as in the case of Global Positioning System (GPS). In GPS, trilateration is based on measurements of time and position using the signals from four GPS satellites. In the case of the reconstruction of o-Ps point of annihilation, only three hit-times and hit-positions of registration of 3 photons are available. The shortage of the fourth reference point is compensated by the conservation of the momentum which implies that the annihilation point of o-Ps → 3γ and the momentum vectors of photons are contained in the same plane. The spin polarization is given by a composition of several factors, where the total polarization of the o-Ps is,

$$P_{o-Ps} = \frac{2}{3} \cdot P_{e^+} \cdot P_\alpha \cdot P_{Scat} = \frac{2}{3} \cdot \frac{v_{e^+}}{c} \cdot \frac{1 + \cos\alpha}{2} \cdot P_{Scat} \tag{3.1}$$

The first factor limiting the polarization is that only 2/3 of created o-Ps atoms possess spins parallel orientation to the spins of the originating positrons [45]. The polarization of the positrons themselves depends on the velocity as shown in the 2nd factor, where the average degree of the spin polarization of positron generated using ^{22}Na source is 0.67 [48]. The 3rd factor (P_α) in the above equation limiting the effective polarization of the positrons from e+ source is the uncertainty of the positron flight direction. In general, for the positrons propagating within a cone of the 2α opening angle, the average polarization along the axis of the cone is given by $(1 + \cos(\alpha))/2$ [48], the cone refers to uncertainty of flight direction of the positrons. In the case of the gammasphere detector experiment, this uncertainty was related to the fact that the positrons were allowed to propagate in a hemisphere of porous material in which positrons could form o-Ps, which are described by a cone of an opening angle of (2α=180°), in that case the factor limiting the polarization was equal to 0.5. Unlike all the previous experiments, J-PET detector attempts to reconstruct the position of the o-Ps annihilation points obtaining an angular resolution of about 15° using the trilaterative reconstruction method [46]. Therefore, the linear polarization loss due to the uncertainty of the determination of the direction of positron will amount to about 1/2(1- cos (15°)) ≈2%.

The last factor P_{Scat} in the equation (3.1) comes from the fact that the positrons inside the porous material are relatively de-polarized as a result of their multiple scattering before they totally stopped, this positrons thermalization reduces the average

polarization of the positrons which suppose to form the positronium atoms. This effect has been simulated and measured in ref [49].

In the case of using ^{22}Na source, based on the above simulation, a small portion of the average polarization (about 8% [49]) was lost during the positron thermalization process as they stop in the porous material. Finally, we expect degree of o-Ps polarization in the J-PET experiment to be equal to:

$$P_{o-Ps} = \frac{2}{3} * 0.67 * 0.98 * 0.92 = 40.27\%$$
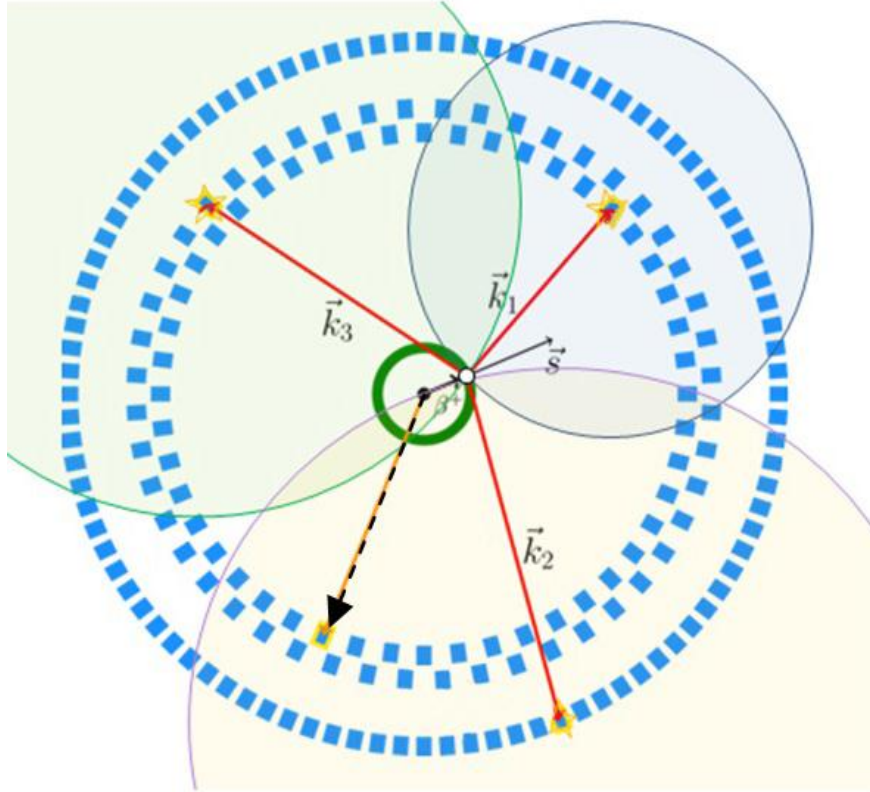
Figure 3.1: Schematic view of the cross section of the J-PET detector, which is made of three layers of plastic scintillator strips (blue rectangles), also, show the scheme of the trilateration-based reconstruction used to determine the ortho-positronium annihilation point. Black dot located in the center indicates ^{22}Na radioactive source emitting positron (e+) and prompt gamma quantum (dashed arrow). Ortho-positronium is produced in the porous cylinder (green band) in which o-Ps formation and decays take place (white dot) and decays into three photons (k1, k2, k3). Red lines denote lines of flight of the three photons used to reconstruct the decay vertex which, in turn, allows us to estimate the positron momentum direction and spin direction $\vec{S}$ of the ortho-positronium [45,7].

J-PET detector has high angular and time resolution and allows for precise measurements the momenta and polarization vectors of annihilation quanta [7,50]. The 3γ originating from the o-Ps annihilation interact with the plastic scintillator strips of J-PET detector mostly via the Compton effect, in this case, the direct measurement of their energy is impossible. However, after the o-Ps to 3γ events are

identified and fully recorded, the energy of each photon may be calculated based on the measured angles between the photons momenta [51].

3.2. The tensor polarization of the ortho-positronium

The tensor polarization is one of the most important characteristics of a Ps atom, which appears in the presence of an external magnetic field. An external magnetic field can be applied in order to align the orientation of the o-Ps spin projection parallel (m=+1), anti-parallel (m=−1) or perpendicular (m=0) to the magnetic field direction. However, the external magnetic field does not only align the spin orientation but also perturbs and mixes the m=0 states. Thus, two new energy states will be possible for the Ps atoms which are called the perturbed singlet and the perturbed triplet m=0 states (see Figure 3.2). The lifetimes of those new states depend on the strength of the external magnetic field. The tensor polarization of o-Ps atom can be defined as $P_2 = (N_{+1} - 2N_0 + N_{-1})/(N_{+1} + N_0 + N_{-1})$, where N_{+1}, N_0, and N_{-1} denote to the number of Ps atoms with a projection of the spin along the quantization axis equal to +1, 0 and -1, respectively. The spin quantization axis will be given by the orientation of the external magnetic field [7]. By the absence of the magnetic field the population of each of the four energy states, one singlet (m=0) and three triplet (m=1, 0,−1) states, is taken to be the same. It means each of the three spin projections can occur with the same probability.

If the external magnetic field is applied, the lifetime of the triplet m=0 state can be drastically reduced with respect to the unperturbed energy state lifetime. In this case, the presence of the magnetic field enable to separate the triplet state m=0 from the triplet m=±1 states, by means of the different lifetimes of the perturbed m=0 and unperturbed m=±1 states. The values of applied magnetic field can be optimized in order to get a maximum separation: it was found that the perturbed triplet states m=0 lifetime for B=0.5 Tesla is about 20 ns [52].

Taking into account that the triplet m=±1 states are unperturbed, they still have a lifetime of 142 ns, with or without an applied external magnetic field. Therefore, one can vary the ratio of N_0 to $(N_{+1}+N_{-1})$ by adjusting a lifetime interval of o-Ps, and consequently, vary the tensor polarization. By Applying an external magnetic field of 0.5 T and a time window from 50 to 130 ns, a tensor polarization of 0.87 was achieved using an aerogel in the experiment described in reference [53].
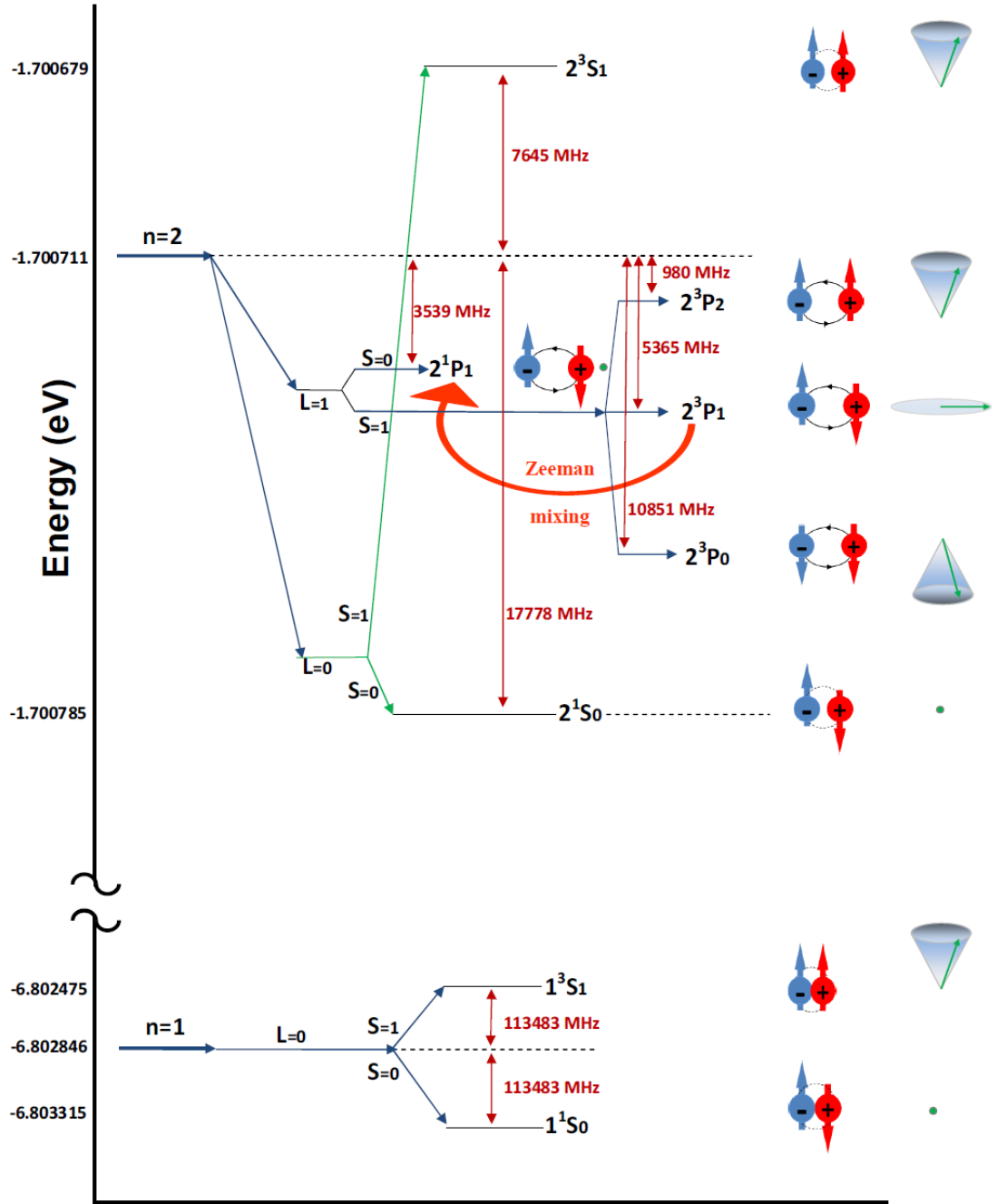
Figure 3.2: Schematic diagram of the positronium energy levels. The diagram is prepared based on information from [**54,55**].

3.3. The degree of the ortho-positronium polarization

The positrons generated through beta decay from ^{22}Na radioactive source are longitudinally polarized because of the parity non-conservation in the weak interaction. This means that the slow positrons emitted from a radioactive source are always spin polarized to some extent [**56**]. The positrons spin-polarized can also be obtained through the spin-orbit interaction method between the un-polarized positrons and heavy target [**57**]. However, this technique is less efficient. Therefore, the crucial

factor is the structure and the design of the positron source. The average polarization can be estimated from the positrons average velocity emitted in the beta+ decays. The average spin polarization of positrons is mostly preserved during formation of ortho-positronium [58].

The o-Ps polarization is by a factor of 2/3 smaller with respect to the polarization of the incident positrons because the spin of electrons in the target is not polarized [6]. This factor can be explained as follows. The both electrons and positrons have a spin 1/2. The two spins values can be added together to give a total spin either $S = 0$ or $S = 1$. Thus, the positronium atom has four ground state levels indexed with S and S_z, where S is the total spin and S_z is the z-projection of the total spin S. The triplet states $|1,1\rangle$, $|1,0\rangle$, $|1,-1\rangle$ and singlet state $|0,0\rangle$ (Figure 3.2) which can be expressed as:

$$\left|S=1,\ S_z=1\right\rangle=\left|\uparrow\right\rangle\left|\uparrow\right\rangle, \qquad \left|S=1,\ S_z=0\right\rangle=\frac{1}{\sqrt{2}}\left(\left|\uparrow\right\rangle\left|\downarrow\right\rangle+\left|\downarrow\right\rangle\left|\uparrow\right\rangle\right),$$

$$\left|S=1,\ S_z=-1\right\rangle=\left|\downarrow\right\rangle\left|\downarrow\right\rangle,\ \left|S=0,\ S_z=0\right\rangle=\frac{1}{\sqrt{2}}\left(\left|\uparrow\right\rangle\left|\downarrow\right\rangle-\left|\downarrow\right\rangle\left|\uparrow\right\rangle\right),\ \text{where the arrows}$$

pointing up and down denote the spin projections of electron and positron.

If the both positron and electron from which the Positronium atom is formed are unpolarized, then the four ground state levels will each be generated with equal likelihood. If the incident positron has some degree of polarization (for example if the incident positron has spins pointing up (+) along the quantization axis), in such situation the formed Positronium will produced more often with $S_z=+1$ than that with $S_z=-1$. Figure 3.3 indicates in a illustrated way that 75% of created positronium atoms will be formed with spin S=1 and only 25% will have a spin S=0. Moreover, 1/3 of ortho-positronia (S=1) will possess $S_z=0$. Taking in to account that in the vacuum, the formation ratio of para-positronia to ortho-positronia (p-Ps/o-Ps) is 1/3, but the process will be in more favor of para-positronium (S=0) production, when it is exposed to the air due to the effects of pick-off and the spin exchange interaction.
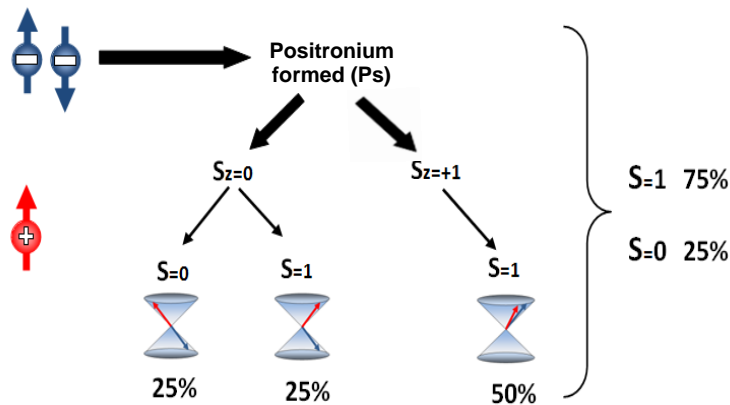

Figure 3.3: Schematic diagram of combined spin states probabilities of positronium formation in an un-polarized porous material by spin-polarized positrons [45].

The longitudinal spin-polarization of positrons along the quantization axis is given by:

$P_{e+} = (N^{e+}_{+1/2} - N^{e+}_{-1/2}) / (N^{e+}_{+1/2} + N^{e+}_{-1/2}) = (v/c) \cdot (1 + \cos 2\alpha/2)/2$, where $N^{e+}_{+1/2}$ and $N^{e+}_{-1/2}$ denote the number of positrons with spin projection pointing up and pointing down their direction of motion, respectively, v represent the speed of positron and α is the opening angle of the cone limiting the direction of emitted positrons [**45**]. The velocity factor can be given by:

$$(v/c) = \sqrt{1 - 1/\{1 + E/(mc^2)\}^2}, \tag{3.2}$$

where E is the kinetic energy of the positrons. In this case one have to select e+ source with higher endpoint energies, in order to obtain positrons with higher spin polarization. One can also filter out the low energy positrons and regulate the solid angle of the emitted positrons.

In order to derive the linear spin polarization of ortho-positronia produced by polarized positrons with the degree of polarization P_{e+} and unpolarized electrons in the target material, we first estimate that (as indicated in Fig. 3.3) the number of o-Ps produced with spin projection +1, 0 and -1 is equal respectively to:

$$N_{+1} = 0.5\, N^{e+}_{+1/2}, \quad N_{-1} = 0.5\, N^{e+}_{-1/2}, \quad N_o = 0.25\, (N^{e+}_{+1/2} + N^{e+}_{-1/2}) \tag{3.3}$$

Thus, the linear polarization of o-Ps, defined as an expectation value of the spin projection onto quantization axis, reads:

$$P^{(\text{linear})}_{o-Ps} = P_{+1} + P_0 + P_{-1} \tag{3.4}$$

where P_{+1}, P_0, and P_{-1} correspond to the m=+1, m=0, and m=-1 states, respectively.

$$P^{(\text{linear})}_{o-Ps} = +1 \cdot (N_{+1}/(N_{+1} + N_0 + N_{-1})) + 0 \cdot (N_0/(N_{+1} + N_0 + N_{-1})) - 1 \cdot (N_{-1}/(N_{+1} + N_0 + N_{-1}))$$

$$P^{(\text{linear})}_{o-Ps} = (+1 \cdot N_{+1} + 0 \cdot N_0 - 1 \cdot N_{-1})/(N_{+1} + N_0 + N_{-1}) \tag{3.5}$$

$$P^{(\text{linear})}_{o-Ps} = (0.5 N^{e+}_{+1/2} - 0.5 N^{e+}_{-1/2}) / (0.5 N^{e+}_{+1/2} + 0.5 N^{e+}_{-1/2} + 0.25(N^{e+}_{+1/2} + N^{e+}_{-1/2}))$$

$$P^{(\text{linear})}_{o-Ps} = 0.5 (N^{e+}_{+1/2} - N^{e+}_{-1/2}) / 0.75 (N^{e+}_{+1/2} + N^{e+}_{-1/2})$$

$$P^{(\text{linear})}_{o-Ps} = 2/3 P_{e+} \tag{3.6}$$

The tensor polarization of the produced o-Ps in the un-polarized material can be defined as:

$$P^{(\text{tensor})}_{o-Ps} = +1 \cdot (N_{+1}/(N_{+1} + N_0 + N_{-1})) + 1 \cdot (N_{-1}/(N_{+1} + N_0 + N_{-1})) - 2 \cdot (N_0/(N_{+1} + N_0 + N_{-1}))$$

$$P_{o-Ps}^{(\text{tensor})} = (N_{+1} + N_{-1} - 2N_0)/(N_{+1} + N_0 + N_{-1}) \tag{3.7}$$

$$P_{o-Ps}^{(\text{Tensor})} = \left(0.5N_{+1/2}^{e+} + 0.5N_{-1/2}^{e+} - 2\left(0.25(N_{+1/2}^{e+} + N_{-1/2}^{e+})\right)\right)\Big/\left(0.5N_{+1/2}^{e+} + 0.5N_{-1/2}^{e+} + 0.25(N_{+1/2}^{e+} + N_{-1/2}^{e+})\right)$$

$$P_{o-Ps}^{(\text{Tensor})} = \left(0.5(N_{+1/2}^{e+} + N_{-1/2}^{e+}) - 0.5(N_{+1/2}^{e+} + N_{-1/2}^{e+})\right)\Big/\left(0.75N_{+1/2}^{e+} + 0.75N_{-1/2}^{e+}\right) = 0$$

So it will be equal to zero independently of the degree of the positron spin polarization [45].

3.4. The angular distribution of the ortho-positronium decay plane

In order to study the angular distribution, let us define Θ as the angle between the positron velocity direction (quantization axis) and the normal to the decay plane. So if we measure for some time the spin projection, we will have a sample which includes N_{+1}^{o-Ps}, N_{-1}^{o-Ps} and N_0^{o-Ps} [59].

The angular distribution in the case of the spin projection $S_z = \pm 1$ reads:

$$\frac{d\sigma}{d\theta}(s_z = \pm 1) \approx \frac{1}{2}(3 - \cos^2\theta),$$

and in the case of the spin projection equal to zero it is equal to:

$$\frac{d\sigma}{d\theta}(s_z = 0) \approx (1 + \cos^2\theta)$$

Now, if we try to find out what would be the angular distribution of the annihilation plane with respect to that quantization axis, so we should add these 3 cross sections:

$$N_{+1}^{o-Ps} \cdot \frac{1}{2}(3 - \cos^2\theta) + N_{-1}^{o-Ps} \cdot \frac{1}{2}(3 - \cos^2\theta) + N_0^{o-Ps} \cdot (1 + \cos^2\theta) \tag{3.8}$$

After substitution of eq. (3.3),

$$= \frac{1}{4}(3 - \cos^2\theta)N_{e+}^{up} + \frac{1}{4}(3 - \cos^2\theta)N_{e+}^{dw} + \frac{1}{4}(1 + \cos^2\theta)(N_{e+}^{up} + N_{e+}^{dw})$$

$$= \frac{3}{4}N_{e+}^{up} - \frac{1}{4}N_{e+}^{up}\cos^2\theta + \frac{3}{4}N_{e+}^{dw} - \frac{1}{4}N_{e+}^{dw}\cos^2\theta + \frac{1}{4}N_{e+}^{up} + \frac{1}{4}N_{e+}^{dw} + \frac{1}{4}N_{e+}^{up}\cos^2\theta + \frac{1}{4}N_{e+}^{dw}\cos^2\theta$$

$$= \frac{3}{4}N_{e+}^{up} + \frac{1}{4}N_{e+}^{up} + \frac{3}{4}N_{e+}^{dw} + \frac{1}{4}N_{e+}^{dw}$$

$$= N_{e+}^{up} + N_{e+}^{dw} = 1(N_{e+}^{up} + N_{e+}^{dw}) \tag{3.9}$$

It means no angular dependence, which shows that without an external magnetic field, the angular distribution of Θ should be isotropic.

4.1. The Jagiellonian Positron Emission Tomograph (J-PET) detector

4.1.1. Basic detector characteristics (General information about J-PET)

Jagiellonian Positron Emission Tomograph (J-PET) is a novel tomography scanner device and the first Positron Emission Tomography scanner build from plastic scintillators as shown in Figures 4.1 & 4.2. The J-PET constitutes a high acceptance multi-purpose detector optimized for the detection of photons from the annihilation of ortho-positronium atoms [7] and can be used in the broad interdisciplinary investigations for fundamental researches including studies of discrete symmetries in the decays of positronium atoms, quantum entanglement of the gamma quanta originating from the decay of ortho-positronium atom [60,61] and research in the field of medicine [62,63]. The organic plastic scintillators, in contrast to inorganic ones, are relatively cheap and easy to shape. This allows for preparation of the cost-effective device enabling a simultaneous metabolic medical imaging of the whole human body. The current commercial PET devices traditionally are based on inorganic crystal scintillators for the detection of the annihilation gamma quanta [64,65]. This PET scanner technology is relatively expensive [66,67] and therefore, there are attempts to find a new, more affordable solutions [68,69]. In the last few years, the Jagiellonian Positron Emission Tomograph (J-PET) collaboration is developing a cost-effective whole-body PET scanner based on organic plastic scintillator strips which will allow reaching a superior time-of-flight (TOF) resolution and a high spatial acceptance at a moderate price.

In the J-PET scanner the light signals, generated by gamma quanta interaction with the plastic scintillator, are read out by a pair of Hamamatsu R9800 photomultipliers connected to the opposite ends of each scintillator strip arranged axially around a cylindrical J-PET scanner [70,71].

Signals from the photomultiplier tubes (PMTs) are sampled in the voltage domain by the dedicated front-end electronics [72]. Based on the difference and the average of these signals it is possible to reconstruct both position and time of interaction of the gamma quanta within scintillator strips. The axial coordinate of the annihilation photon interaction point in the scintillator bar is derived from the difference of the light propagation time measured with the pair of photomultipliers. The organic plastic scintillators were not considered as potential sensors for PET scanner due to their low density (1.03 g/cm^3) and small Z atomic number of elements constituting the material, where the organic scintillators mainly consist of carbon and hydrogen atoms [7]. The small atomic number of organic plastic scintillators leads to a small probability that the gamma quanta transfer all of their energy to the electrons of the organic scintillator via the photo-electric effect [7]. Moreover, the organic scintillators have a small density and thus small efficiency for the detection of gamma quanta. However, disadvantages due to the low detection efficiency and the negligible probability for the photoelectric effect can be partially compensated by large acceptance and improved time resolution achievable with plastic scintillator detectors [73]. The efficiency can also be drastically increased by adding more plastic scintillator layers in the J-PET detector [51] as well as enhanced scintillator readout by using silicon photomultipliers [71] and new electronics readout [74]. The axial length of the current

version of J-PET detector which has 50 cm tunnel length increase on average by a factor of about three in the comparison to the current commercial PET scanners. The larger longitudinal field of view of J-PET detector allows for simultaneous imaging of a larger fraction of the body. The current version of J-PET scanner consists of three layers of EJ-230 plastic scintillator strips readout by Hamamatsu R9800 PMTs which is forming a cylinder of diameter equal to 85 cm and its active inner part length is equal to 50 cm. Plastic scintillators are wrapped with Vikuiti foil and additionally covered with tight black foil light-protection. The signals from each photomultiplier are probed by multi-threshold digital electronics with a timing accuracy of about 30 ps [67].

4.1.2. The advantages of organic scintillators over inorganic crystal

The advantages of organic scintillators include fairly high light output and a relatively quick signal, with a short time of the decay, but perhaps the biggest advantage of plastic scintillators is their ability to be shaped and their lower production costs. It also has the following advantages especially for J-PET detector:

1. The organic plastic has much better light transfer properties than crystals by absorbing internally much less light which is emitted by scintillation from gamma radiation. Light attenuation of crystals is about 20 cm, while this of plastics reach even 380 cm [75,76]. As a result of this process, the photomultipliers will get enough light in order to produce signals when using long polymer scintillator strips. Conversely, the long inorganic crystal scintillators would simply absorb most of the light before it had a chance to reach the PMTs.

2. The possibility to produce the whole body J-PET scanner, where the length of the scanner along z-axis changes with the length of the scintillator without impact on the complex structure of the scanner. Unlike J-PET, conventional scanners need more crystals, photomultipliers, and cables in order to enlarge their field of view (FOV) along z-axis.

3. The J-PET scanner is much cheaper and has simpler structure compared to conventional PET as a whole device because the sets of crystal scintillators along z-axis are simply replaced by just one single plastic scintillator strip, thus overall device complexity is reduced. Also in the case of the large FOV along z-axis, the J-PET has less number of PMTs and less power and signal cables that carry these signals to electronic circuit boards.

4. The design of J-PET opens the possibility of Jagiellonian Positron Emission Tomography-Computed Tomography (J-PET-CT) which would combine a positron emission tomography scanner and an x-ray computed tomography scanner in a single gantry in order to acquire sequential and simultaneous images from both devices in the same session. The plastic scintillators absorb CT radiation much less than inorganic crystals, therefore, J-PET scanner can be coupled with a CT device, operating in the area not covered by PMTs and cables, in order to provide perfectly aligned PET and CT images from a single medical examination.

5. The possibility to produce Jagiellonian Positron Emission Tomography-Magnetic Resonance Imaging (J-PET-MRI) and operate them together after use of semiconductor PMs instead of R9800 PMT or use the same current types of PMTs with a magnetic shielding system.

4.1.3. The principles of the J-PET detector

The operating principles of J-PET scanner are quite similar to the classical PET devices, except that the exact timing information plays a crucial role in the case of J-PET detector. The J-PET scanner is built out of an organic scintillator strips. The active inner part of the detector has a cylindrical shape with the length of 50 cm and a radius of 42.5 cm. Figure 4.1 shows the scheme of registration of 2ɣ events in the J-PET detector modules.
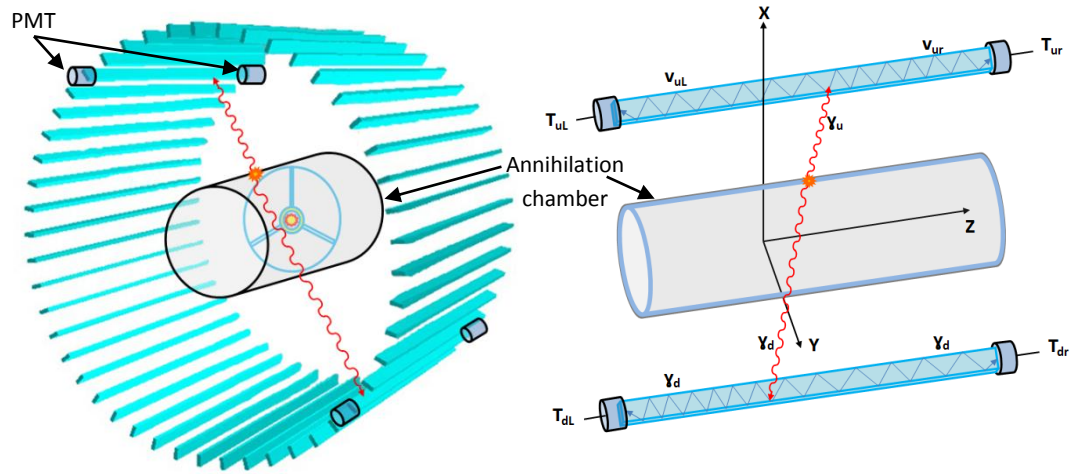
Figure 4.1: Left: Scheme of registration of 2ɣ events in the J-PET detector modules shows the cylindrical annihilation chamber with length of 50 cm and a radius of 12 cm, which contain the three-arm holder with the ^{22}Na source inside the large chamber. Also shows how the plastic scintillator strips are optically connected at two ends to Hamamatsu R9800 PMTs. Right: The arrangements of the scintillator strips is visualized schematically, the light pulses from each strip are converted to electrical signals by two photomultipliers placed at opposite ends.

Table 4.1: Configuration of the current J-PET prototype [77].

Layer	Radius	No. of detectors	Scintillator dimensions	Scintillator cross-section
1st layer	42.5 cm	48	0.7x1.9x50 cm	Rectangle
2nd layer	46.75 cm	48	0.7x1.9x50 cm	Rectangle
3rd layer	57.5 cm	96	0.7x1.9x50 cm	Rectangle

4.2. Description of the J-PET apparatus

4.2.1. The Hamamatsu R9800 photomultiplier tubes

The R9800 photomultiplier has an extremely short transit time spread (0.27 ns) that is uniform across the whole photocathode effective area [**78**]. The active base assembly has been designed to be used with a scintillator strip of the J-PET, and all PMTs are equipped with a new active base. The base comprises a high voltage divider integrated with amplifiers powered by current flowing through the divider.

The R9800 PMT has a simple head-on design that is suitable for mass production but differs in terms of their size and other specifications. It has a 25 mm (1 Inch) diameter and provides a gain of 1.0×10^6 with a rise time of 1.0 ns and transit time spread of 270 ps. The supply voltage required is between 1300 and 1500 volt [**78**].

This design allows limiting the PMT anode current to 15-20 µA at a 4 MHz count rate. The performance of the PMT assemblies has been checked at the J-PET Lab using a two modules prototype and oscilloscope a Serial Data Analyzer (Lecroy SDA6000A). In the J-PET detector, about four hundred PMT and base assemblies were manufactured and tested. The photocathode is bialkali material, contains 8-stages with a spectral response range of 300 nm to 650 nm. Peak sensitivity is in the blue region of 420 nm, which makes these PMTs ideal for scintillation counting. Intended applications include time-of-flight PET in nuclear medicine, time-of-flight counting in high-energy physics experiments, and radiation monitoring in security instruments.

4.2.2. The plastic scintillator strips

The scintillator is a material emitting light after being excited by ionizing radiation and absorbing some of its energy [**79**]. This phenomenon is called scintillation. Scintillators are significant components in radiation detectors, called scintillating counters. The commercial PET scanners are based on different kinds of inorganic crystals with much higher densities than organic plastic scintillators (typically 4-8 g/cm^3) allowing to absorb gamma quanta in a small volume of the crystal via Compton and photoelectric effect [**64,80**]. Cerium doped lutetium oxyorthosilicate scintillator (LSO) and cerium doped lutetium-yttrium oxyorthosilicate (LYSO) scintillator emit about three times more light per unit of deposited energy than the plastic scintillators but their decay time is one order of magnitude longer.

The Plastic scintillators are well suited for applications in time of flight (TOF) detectors due to their short time response and the possibility of production in different sizes and shapes. The achievable time resolution of a PET scanner depends on the decay and rise time of light signals produced in scintillators and on the amount of light reaching the photocathode of the photomultipliers. The decay time of a typical plastic scintillator ranges between 1.4 ns and 2.4 ns and light output amounts to approximately 10,000 photons/MeV of absorbed energy.

The maximum of emission spectra is observed at around 391 nm and this value matches well the quantum efficiency of typical photomultiplier tubes [**78**].

A developed method [75] was used for the tests and quality control of EJ-230 scintillator strips which were used for the construction of the current J-PET version with the R9800 PMT readout. The first full-scale prototype of the J-PET tomograph built from the plastic scintillators [81] with the contribution of the author of this thesis is shown in Figure 4.2.
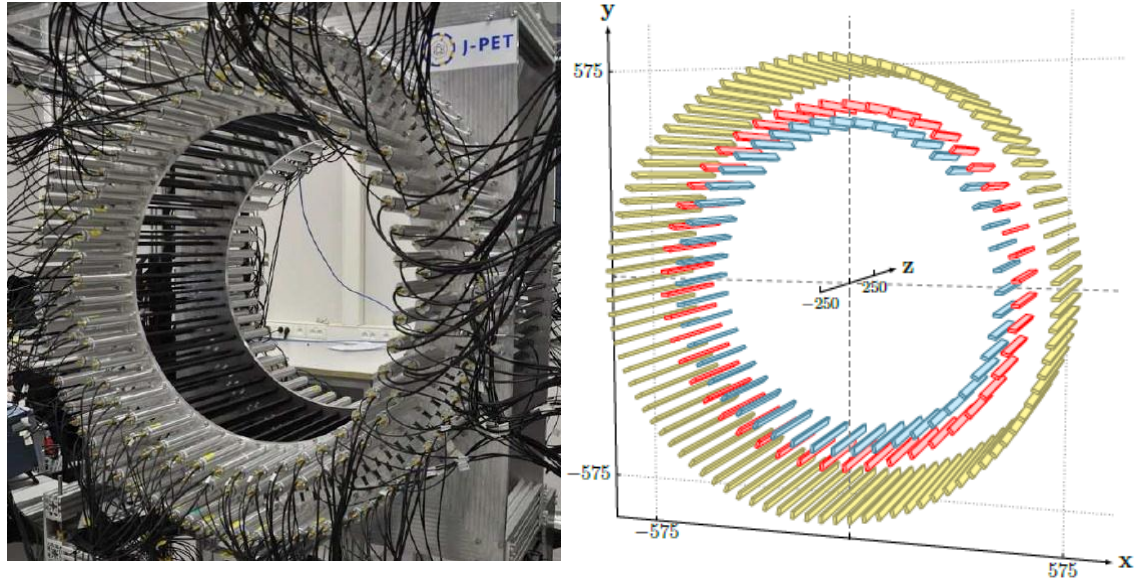

Figure 4.2: Left: Photo of the J-PET scanner. The active inner part of the scanner has a cylindrical shape with the length of 500 mm and a radius of 425 mm. The J-PET detector has three layers of plastic scintillator strips wrapped with the Vikuiti specular foil and covered with a light-tight foil (black strips). The scintillators are connected optically at their two ends to Hamamatsu R9800 vacuum photomultipliers tube and placed inside aluminum protective housing (gray pipes). Right: a schematic view of the built J-PET detector layout.

Table 4.2: The physical properties of EJ-230 [64].

Property	Value
The polymer base	Polyvinyltoluene
Density	1.023 g/cm^3
Refractive index	1.58
Light output	64% anthracene (9700 photons/1 MeV e-)
Wave length of maximum emission	391 nm
Light attenuation length	100 cm
Rise time	0.5 ns
Decay time	1.5 ns

4.2.3. Ambient conditions monitoring system

The measurements of temperature, humidity, and pressure in the J-PET laboratory were done automatically by J-PET ambient conditions monitoring system. The device can also monitor and save pressure values from the vacuum pump. Also measures temperature in 10 points by using DS18B20+ sensors. Each sensor can measure temperature in the range from -50 ^{o}C to +125 ^{o}C with measurement accuracy equal to 0.1 ^{o}C. The measurement of relative humidity is done by using two sensors (model AM2303) placed in two different locations in the J-PET Lab. Each sensor can measure humidity in a range from 0 to 100% with accuracy equal to 0.1%. The measurements of atmospheric pressure are also done in the range from 800 hPa to 1200 hPa with accuracy equal to 0.1 hPa (sensor model BMP180). The system shows current values from all sensors on the monitoring screen every 10 seconds in automatic mode. The device is able to save these values into a text file, usually, an interval of 10 min is used.

4.2.4. The HV power supply

The photomultipliers were connected to CAEN SY4527 high voltage power supply. The applied voltages were set in a way that the gain on all photomultipliers was approximately equal, Figure 4.3 shows the scheme of HV connections.
The power supply section allows different configurations with up to 4 power supply units per mainframe (up to 4200 W), while the board section can house up to 16 boards able to perform different functions.
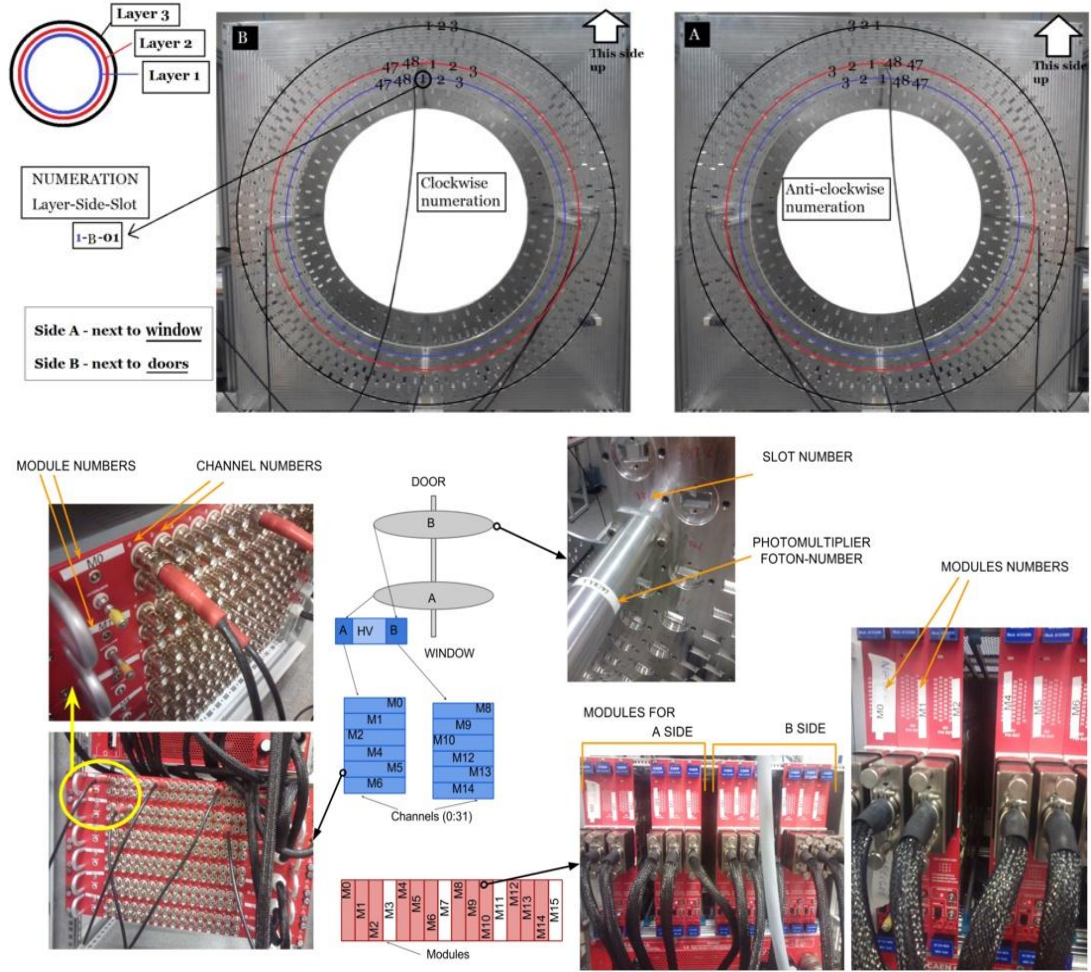
Figure 4.3: The scheme of HV connections.

4.2.5. Data acquisition system (DAQ)

The data acquisition system (DAQ) is the integration of several components which consists of sensors, DAQ measurement hardware, the output/display module, and a computer with programmable software. It also contains the control module that store the digital data of the J-PET detector.

The main part of the DAQ system of the J-PET detector is based on the collection of Trigger Readout Board v3 (TRBv3) modules, based on Field Programmable Gate Array (FPGA) which is commonly used in a high energy physics experiments. The continuous data acquisition process has been achieved by use (trigger-less) measurement mode which is a novel approach in such a kind of detectors [**82**], and that data can be used for further analysis.

4.2.6. Front-End electronics

Signal amplification, shaping, and discrimination are the main functions of the Front-End electronics. The input electric signals coming from the PMT's are amplified and split into four paths, each having an individual voltage threshold level. It is a realization of the multi-level threshold concept as a measure for reducing the time-walk effect and, therefore, achieving better timing resolution [**72**]. The TDC

design used in the J-PET allows for measurement of 48 input channels, hence a single FEE module has 12 inputs from the photomultipliers.

4.3. Software:(J-PET framework, MLEM)

4.3.1. J-PET framework

The J-PET analysis framework software is a flexible and light weight software package based on ROOT [83], which provides all the tools used in order to develop reconstruction and calibration procedures for the J-PET device. The framework incorporates automated handling of J-PET setup parameters' database as well as high-level tools for building data reconstruction procedures. A detailed description of the J-PET analysis framework software used for reconstruction and analysis of the J-PET data can be found in the reference [83,84,85].

4.3.2. Maximum Likelihood Expectation Maximization (MLEM)

In order to reconstruct a tomographic image with J-PET, a MLEM method is used. The expectation-maximization (EM) [86,87] can be described as an iterative method of finding maximum likelihood (ML) estimate [71] from observed data E, e.g. scan. The goal of EM is to find estimates model image ρ for which the observed data is most likely i.e. $P(E/\rho)$ is a maximum. The maximum-likelihood (ML) expectation-maximization (ML-EM) algorithm is being widely used for the procedure of image reconstruction in positron emission tomography.

The J-PET detector does not measure an image directly but measures a sinogram at the boundary of the field-of-view (FOV) that consists of measurements of the sums of the counts along the lines of response (LOR) connecting every two detectors. The purpose of the algorithm of image reconstruction is to process an imperfect count data for a large number of LOR and a huge number of detected photons to create an image. The MLEM reconstruction algorithm approach is used to calculate the decay points distribution. The algorithm adds the decay points for each pixel along a LOR detected by each detector pair. This process is repeated for all possible LORs, which produce an image of the original object.

4.4. Time of flight (TOF) calculation

The time of flight (TOF) technique of gamma quanta in the PET scanner has been used since 1980 [88]. The time of flight (TOF) calculation is the mean key in improving the quality of the reconstructed images, which can be achieved by the determination of the annihilation point on the LOR based on the measurements of the time difference between the arrival of the gamma quanta to the scintillator strips of the detector. The measurement of the arrival time difference between the two photons (t_2-t_1) gave the opportunity for improving the resolution of the tomographic image via determination of the annihilation point relative to the LOR's center which denoted as Δx is shown in Figures 4.4 and 4.5.

A single module of the J-PET scanner consists of a 50 cm length of scintillator strip connected and read out by two photomultipliers. In the first approximation, the distance of gamma photon interaction from the center of the scintillator (Δl) is

determined based on the difference between arrival times of light measured at both ends of the strip. In the case of the e+e- annihilation into two-photons, the position (Δx) along the line of annihilation is determined from time difference which is measured between any two modules. In practice, more advanced methods of hit-time and hit-position determination were developed which take advantage of the variation of the signal shape as a function of the hit position [71]. Practically, due to the finite resolution of the time measurement, it would be possible to determine only a range along the LOR in which the annihilation point is located, which also improves the resolution of the J-PET images. In addition due to the large solid angle covered by the J-PET detector construction, the decrease of the efficiency of the detector will be compensated by the increase of the detector acceptance.

In the case of annihilation into three photons, the positronium annihilation point is reconstructed based on the trilateration method [46].
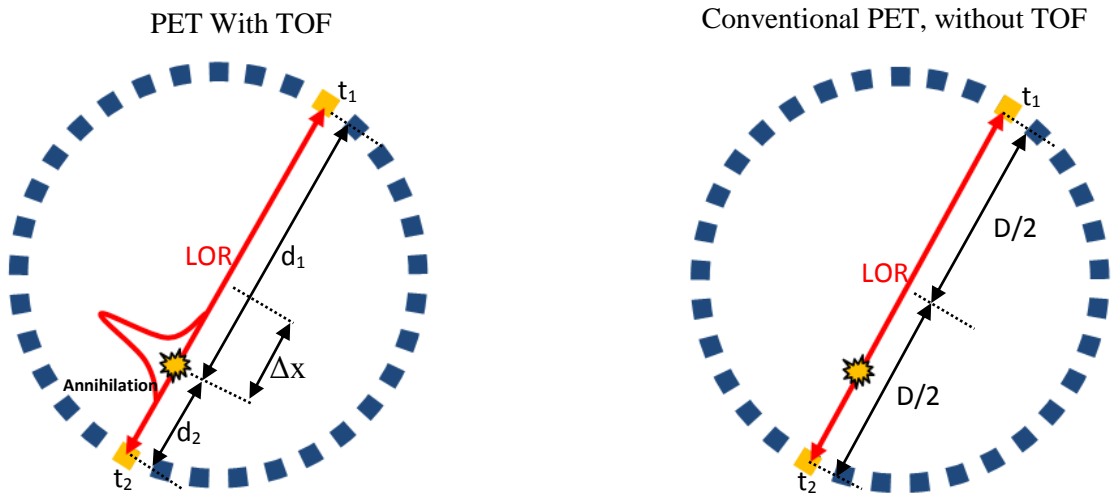

Figure 4.4: Left: Scheme of the PET with TOF, the idea of PET-TOF is $\Delta x = (t2 – t1) \, c/2$. Right: Scheme of the conventional PET, without TOF.

A schematic view of the TOF calculation method using two strips module of the J-PET is shown in Figure 4.5. The determination of hit position versus the central position of the scintillator (Δl) is based on time difference measured on both sides of the scintillator strip (L and R), and the position (Δx) along the line of response (LOR) between them is estimated from the time difference measured between two opposite modules. A_L and A_R are a pair of photomultipliers connected to the left and right edges of the scintillator A, respectively. Similarly, B_L and B_R are the photomultipliers connected to two edges of the scintillator strip B.
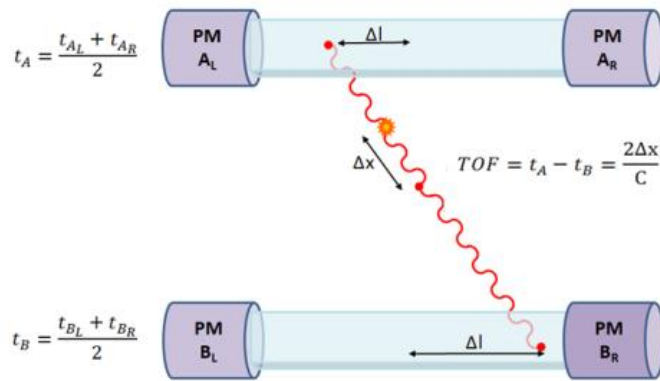
$$t_A = \frac{t_{A_L} + t_{A_R}}{2}$$

$$t_B = \frac{t_{B_L} + t_{B_R}}{2}$$

$$TOF = t_A - t_B = \frac{2\Delta x}{C}$$

Figure 4.5: Scheme of the TOF calculation method, showing two-strips of the J-PET module setup. Place of 511 keV γ quanta interaction with scintillator material (Δl) measured relative to the strip center is determined from the difference between light signals arrival times to both photomultipliers. Place of the two-photon annihilation event (Δx), along with the line of response (LOR), is defined by the time difference between two modules as described in detail in references [66,67,68].

5. Conducted measurements of o-Ps decay in J-PET detector

5.1. The annihilation chambers

5.1.1. The small annihilation chamber

The first long measurement with the J-PET detector was done using a small annihilation chamber which was prepared in the Maria Curie-Sklodowska University (UMCS) in Lublin. This chamber had a 7 cm radius. The whole small annihilation chamber was made of aluminum and located at the center of J-PET scanner. Positronium source activity was equal to about 10 MBq. In this experiment, we mostly detected the annihilation into 2γ rays from both direct annihilation and 3γ rays from the direct e+e- annihilation, because the positronium formation-enhancing medium was not included in this measurement (compare to the setup described in 5.1.2). Therefore, the test of 3γ event reconstruction was based on direct 3γ annihilation of positrons with electrons of the aluminum chamber inner walls, with a yield smaller by a factor of about 370 than the rate of $e^+e^- \rightarrow 2\gamma$.

The details of annihilation chamber preparation are shown below. Also, the chamber mounting is shown in Figure 5.1. One can find schematic of annihilation chamber tube from J-PET detector mounting plate in x-axis and z-axis in Figure 5.2. The small annihilation chamber was connected to the vacuum pump in order to remove the molecules of air and other gases from the vacuum chamber.
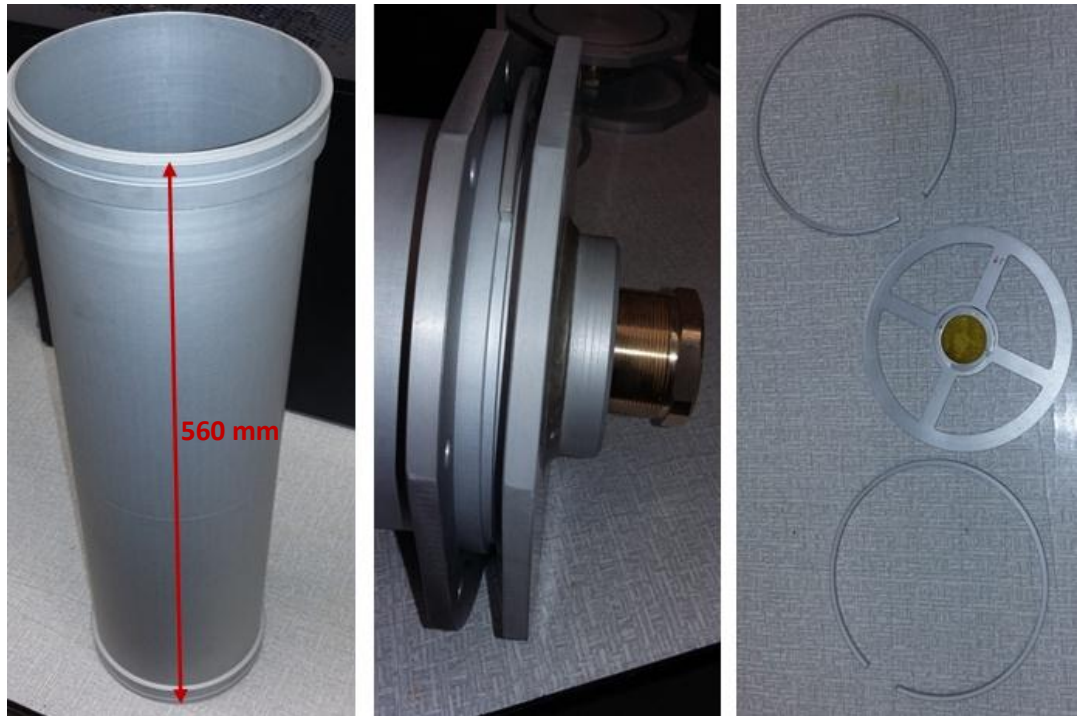

Figure 5.1: The photographs of small annihilation chamber, chamber cover, and the e+ source with the four arms holder. The diameter of the source holder is equal to the inner diameter of the annihilation chamber.
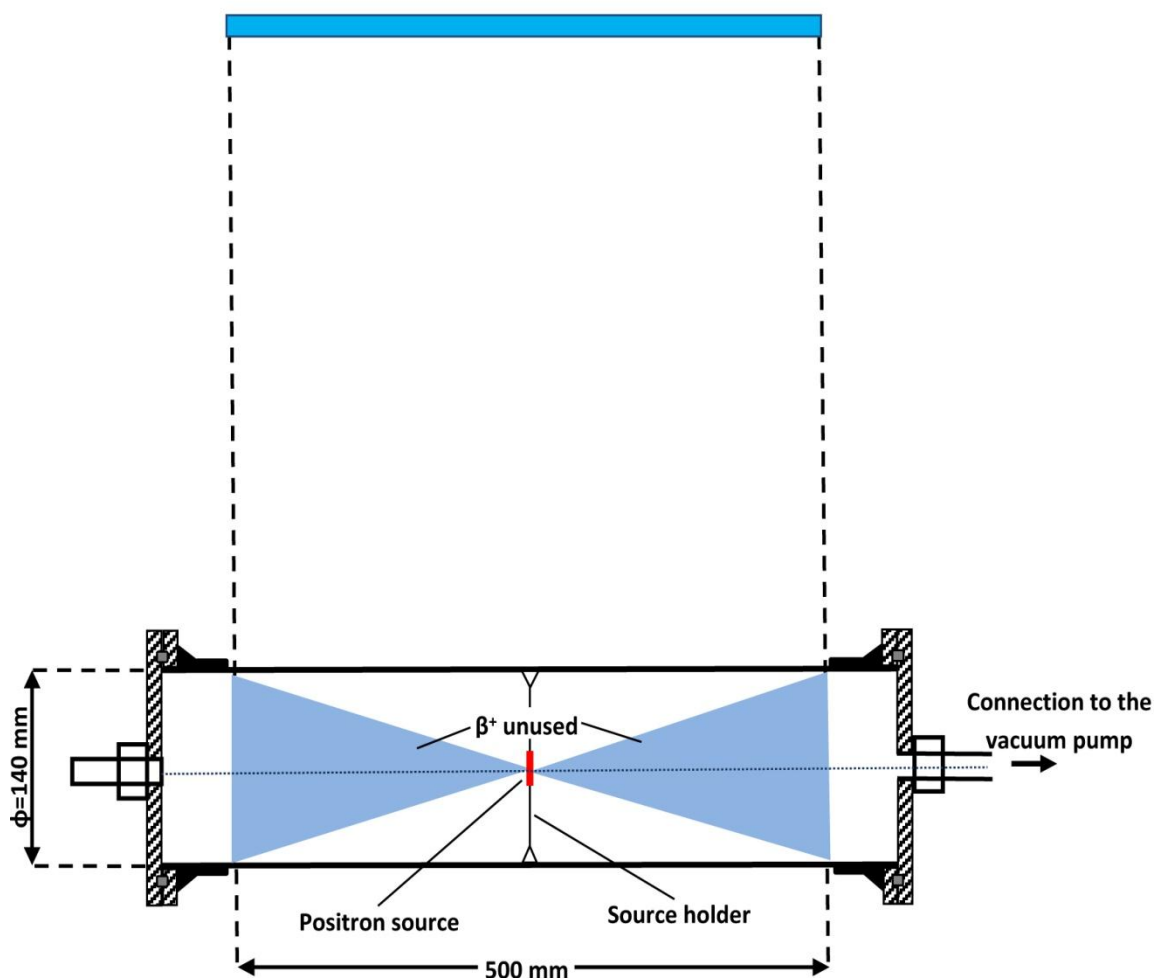
Figure 5.2: Scheme of the small annihilation chamber devised for positron polarization determination in J-PET experiment. Positrons are produced by a β+ source mounted at the center of the cylindrical annihilation chamber which is coaxial with the J-PET detector.

5.1.2. The large annihilation chamber

For the main experiment studied in this work, the large annihilation chamber was used, also prepared at Maria Curie-Sklodowska University in Lublin. The large chamber, made with the cylindrical polymer, has a 12 cm radius with 3 mm thickness and two aluminum covers on the bases of the cylinder. One of them has a hole in order to connect to the vacuum pump. The inner walls of the chamber were coated with porous silica R60G, a medium for positronium production. The setup presented in Figures 5.3-5.6 was constructed and tested in 2018. The experiment was done using the large annihilation chamber for a set of measurements which was dedicated to the identification and reconstruction of the 3ɣ events from o-Ps.
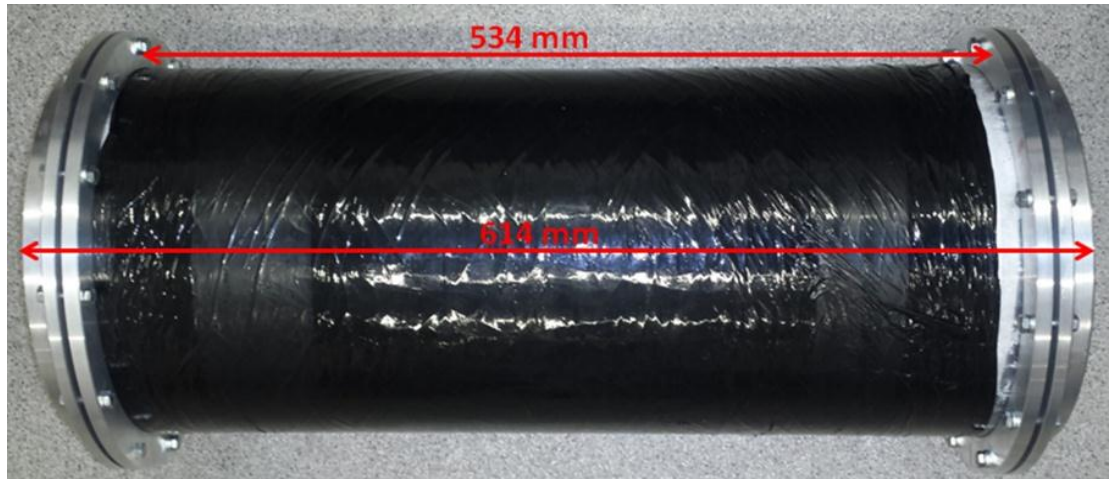
Figure 5.3: The large annihilation chamber devised for positron and positronium polarization determination in J-PET detector experiment.

The activity of the ^{22}Na sources enclosed in Kapton foil envelope which was made in UMCS has been measured before starting the experiment and calculated in reference to UR450 sodium-22 source of known activity and the activity was equal to 10 MBq. The positron source was then placed inside the vacuum chamber using a holder with three arms as shown in Figure 5.4, which shows the holder inside the chamber and the inner wall of the large chamber coated with the porous silica R60G. Figure 5.5 (left) also shows the positron source fixed on the holder. The measurements were performed at room temperature while maintaining the pressure in the chamber at the level of about 10^{-3} Pa. The preparation and the test of the large annihilation chamber are shown in Figure 5.6, where few requirements were asserted: source is in a central position, the chamber is symmetric and its walls have low gamma-ray absorption as shown in Figure 5.7.
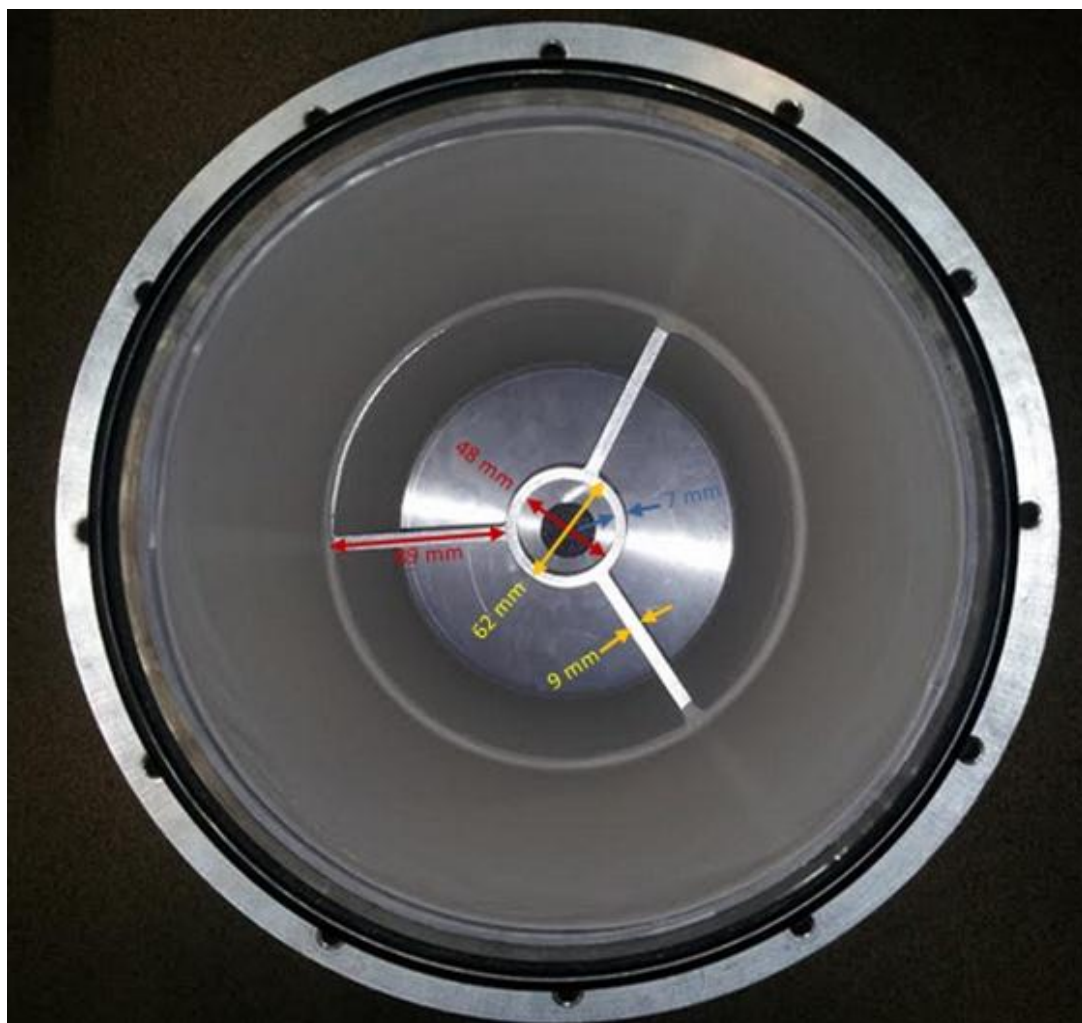
Figure 5.4: The inner wall of the large chamber showing the porous silica R60G and the three-arm source holder. The diameter of the source holder is equal to the inner diameter of the large annihilation chamber.
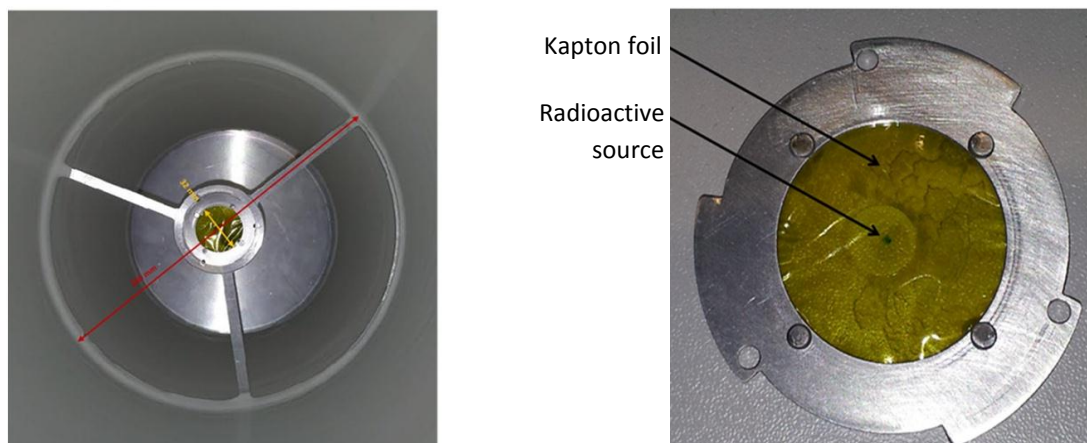
Figure 5.5: The three-arm holder with the [22]Na source inside the large chamber (left), the [22]Na source (right) which is used with large annihilation chamber. Positrons are produced by a [22]Na radioactive source mounted at the center of a cylindrical annihilation chamber which is coaxial with the J-PET detector. Positronium atoms are formed by the interaction of positrons in a porous layer covering the chamber inner walls. Determination of an o-Ps→3γ annihilation position in the cylinder provides an estimate of positron momentum direction.
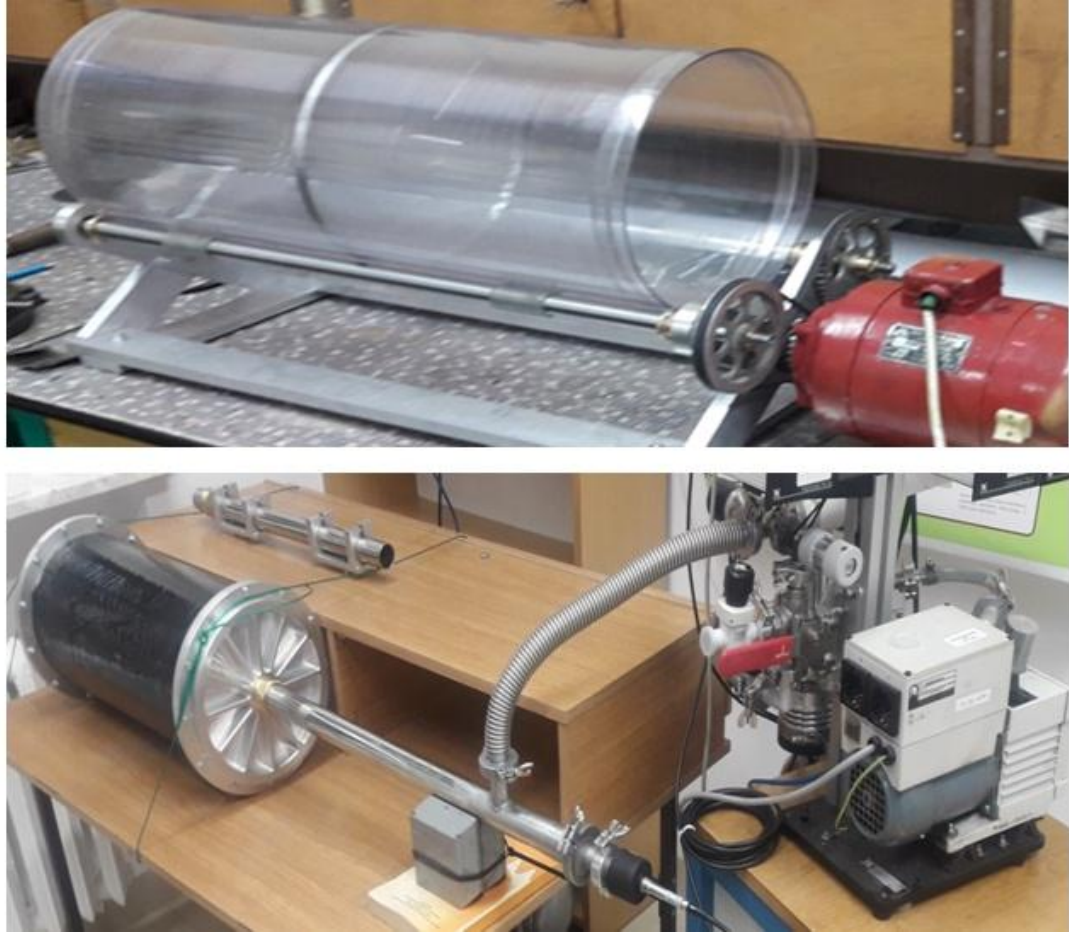
Figure 5.6: The preparation procedure of the large annihilation chamber, coating with the R60G silica porous material on the inner walls of the large annihilation chamber [**89**].
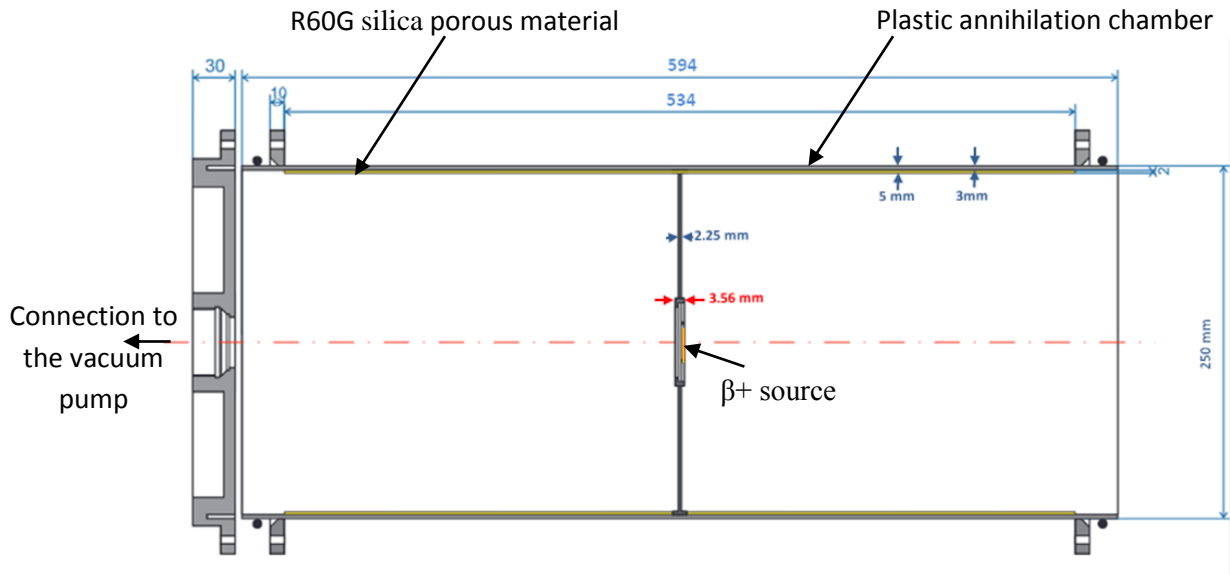

Figure 5.7: Scheme of the large annihilation chamber devised for J-PET experiments. Positrons are produced from an e+ source mounted at the center of a cylindrical annihilation chamber (see Figures 5.5 and 5.6). The chamber is coaxial with the J-PET detector [**89**].

5.2. The porous material target (Characteristics of porous silica R60G, SiO2 powders).

Porous silicon is a form of the chemical element silicon that has introduced a porous in its microstructure (see Figure 5.8) rendering a large surface to volume ratio in the order of 500 m^2/cm^3. The porous materials with open pores at the surface are important and necessary to produce a high yield of positronium atoms as well as positronium moderators through collisions with the inner walls of the pores before emerging in the free space outside the porous target. The previous experimental results indicate that aerogel and porous silica are good candidates for an efficient formation of thermal Ps atoms [90].
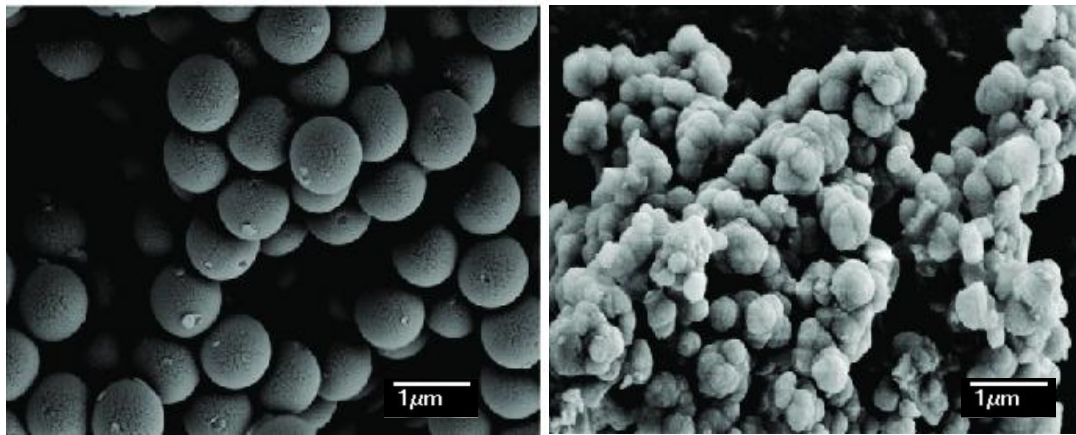
Figure 5.8: Scanning electron microscope (SEM) images of the non-porous silica particles (left), and porous silica particles (right) [91].
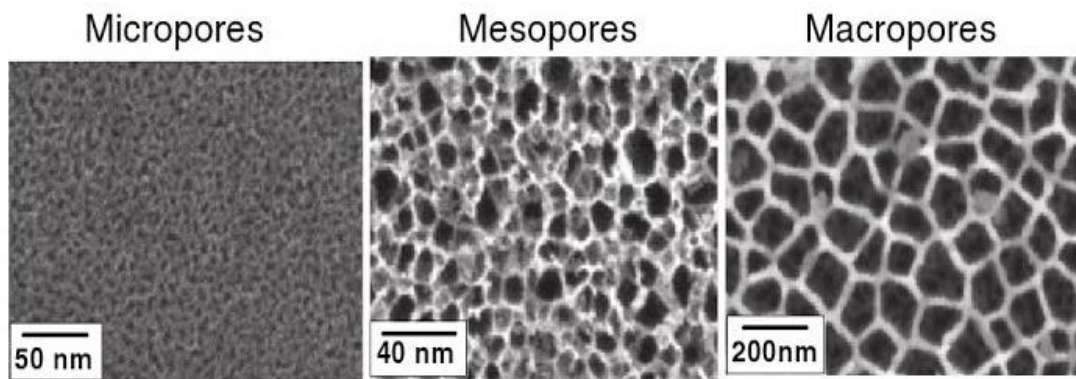
Figure 5.9: The typical morphology examples of micro porous, meso porous, and macro porous materials [92].

The porous silica R60G is a form of silicon with unique properties, distinct from those of crystalline or amorphous silicon. The porous silicone materials can be classified into three main categories based on the pore size: microspores silicon with pore diameters smaller than 10 nm, mesopores silicon with pores diameter in the range of 10-50 nm, and macropores silicon with pores larger than 50 nm as shown in Figure 5.9 [92].

5.3. The positronium production setup

5.3.1. Positron sources based on β+ decay

Most positron source experiments usually used the β+ emitters in order to prepare a polarized slow positron source. There is a large variety of β+ emitting nuclides which have different lifetimes, as shown in the Table 5.1 which includes the most important relevant data like end-point energy (E_{max}), helicity (v/c), average energy (E_{av}), energy (E_γ) and the intensity (I_γ) of the most dominant gamma transition. The yield of positron (I_{e+}) is usually below 100% due to competing electron capture (EC).

Table 5.1: The main properties of radioactive beta+ emitting nuclides mainly used in positron experiments. The Table is adapted from [**93**].

Nuclide	Half life	I_{e+}	E_{max} (keV)	E_{av} (keV)	v/c	E_γ (keV)	I_γ
^{11}C	20.4 min	0.998	960.0	385.6	0.822		
^{13}N	9.97 min	0.998	1198.3	491.8	0.860		
^{15}O	2.04 min	0.999	1731.7	735.3	0.912		
^{18}**F**	110 min	0.967	633.2	249.8	0.741		
^{22}**Na**	2.60 y	0.898	545.4	215.5	0.711	1275	0.999
		0.001	1819.7	835.0	0.925		
^{26}Al	$7.4 \cdot 10^5$ y	0.818	1173.2	543.5	0.875	1809	0.997
^{27}Si	4.16 s	0.997	3788.8	1719.8	0.973	2211	0.002
^{44}Ti/^{44}Sc	49.0 y	0.943	1475.3	632.6	0.895	1157	0.999
^{48}V	16.0 d	0.499	694.6	290.3	0.770	984	1.000
		0.004	2006.6	878.6	0.930	(1312)	(0.975)
^{57}Ni	35.6 h	0.353	865.0	368.7	0.814	1378	0.817
		0.070	738.0	313.7	0.785	(1920, 127)	(0.123, 0.167)
^{58}**Co**	70.8 d	0.150	475.2	201.3	0.697	811	0.994
^{64}**Cu**	12.7 h	0.179	652.5	278.1	0.762	1346	0.005
^{68}Ge/^{68}Ga	271 d	0.880	1899.0	836.0	0.925	1077	0.030
		0.011	821.7	352.6	0.806		
^{72}**Se**/^{72}**As**	8.40 d	0.642	2500.0	1117.0	0.949	834	0.795
		0.163	3334.0	1528.5	0.968		
^{89}Zr	3.27 d	0.228	902.0	395.8	0.826	909	0.999

5.3.2. The preparation of the positron source

The design of the annihilation chambers was motivated by the requirement to estimate the e+ momentum direction event by event as described in Section 3.1. The positrons emitted in the decay of a ^{22}Na radioactive source are longitudinally spin-polarized (right-handed) along the direction of motion as a result of parity non-conservation in the weak interaction. The degree of polarization is proportional to the emitted particle's speed. In the case of ^{22}Na, an average polarization calculated from an average velocity of positrons from the positron source is around 67 %. In the two measurements studied in this work, two low-energy positron sources have been built based on β+ sources. However several setups have been tested at (UMCS) in Lublin in order to produce a positron source appropriate for linear polarization estimation. In

the J-PET experiments, we used ^{22}Na radioactive source with activity equal to 1 MBq and 10 MBq dated on November 2017. The radioactive source was placed in the middle between two layers of Kapton foil. The source was located in the geometrical central of the cylindrical annihilation chamber.

5.3.3. Producing highly polarized slow positrons

The polarization of the positron at the moment of the positronium formation depends on the type of the beta+ source, absorber material, moderator and on changes in the directions of spins caused by passing through all of those materials. The backscattering can be reduced by depositing the ^{22}Na on a low-z material (e.g. Be). Some of the positrons are absorbed in the source material, and the source holder, and any additional absorbers located between source and annihilation chamber. The Kapton foil act as absorber which also increase the positrons polarization by preferentially absorbing those positrons that are emitted at low energy and large angles relative to the axis of the tomograph, where the axis of the tomograph is perpendicular to the surface of the radioactive source. While absorbers increase the degree of polarization for the above reasons, they also reduce the positron intensity.

5.3.4. The preparation of the positron source for large annihilation chamber

The ^{22}Na isotope was used as a source of positrons for the large annihilation chamber experiment. The source was prepared by sealing a few drops of ^{22}Na solution (NaCl solution) placed in the middle, between two Kapton layers with a thickness equal to 8 μm each as one can see in Figure 5.5 (left). The layers of the Kapton foil were glued using Eccobond 144A glue, compressed by a cylindrical piston and holed using two thin aluminum rings connected together by four aluminum rivets, as one can see in Figure 5.5 (right). The ^{22}Na has a half-life of 2.6 years and its other properties are shown in Table 5.1. The Q value for the nuclear transition of ^{22}Na to ^{21}Ne is equal to 2.843 MeV. This is the maximum energy available for the particles involved in one of the three possible decay modes of ^{22}Na. The positron decay occurs in about 90.6% of the decay cases and has an end-point energy of 545.4 keV. The positron emission is always followed by the prompt emission of a 1.27 MeV photon (3.7 ps mean delay) which comes from the de-excitation of ^{22}Ne to the ground state. There is also about 9.944% of the decays by an electron capture process (EC) that takes place when an orbital electron is captured by the nucleus. It means that the main decay mode of ^{22}Na is through the emission of positron (90.6%) which is followed by gamma emission with energy 1.275 MeV. The β+ transition directly to the ground state of ^{22}Ne is also observed with a small probability (0.056%). This transition is through the emission of a positron with the maximal possible value of endpoint energy (1.821 MeV). The emitted positrons that pass through the vacuum chamber, enter the porous material (porous silica R60G) target where they have the possibility to bind to an electron and form positronium atoms. The R60G silica is a porous material with a density of 85 mg/cm3 [90], and it has an average grain size of about 50 - 100 nm [94], see Figure 5.8. During the experiment data taking, a three days period of measurements were done without vacuum in order to check the effect of the air quenching, which arises from spin exchange of Ps with the O_2 present in the air.

5.3.5. Positron source preparation for small annihilation chamber

The design of the positron source capsule was done as shown in Figure 5.10. The basic concept is similar to that positron source which was designed to be used with large annihilation chamber (section 5.3.5). A few drops of liquid ^{22}Na radioactive material were dropped to the middle of Kapton foil disc, after drying the liquid for several hours using a special light bulb, it is covered with a second layer of Kapton foil (8 μm thickness). The air leak is prevented by rigid contact of the edges of the source. The Eccobond 144A glue was used between the foil layers, outside the internal piston by pressing the foils with glue with another external piston and heat it for hardening the glue. Finally, we obtained small circle without air or glue (just foil and radioactive isotope) in the central part, and an external ring with glue. Thus, the source can be used in a vacuum condition. The two layers of Kapton foil had glued together, surrounded with aluminum rings inside the source holder (Figure 5.10 right). The source holder and the source frame should be made of low-z materials to reduce the backscattering probability of positrons. Therefore, both are made of aluminum.
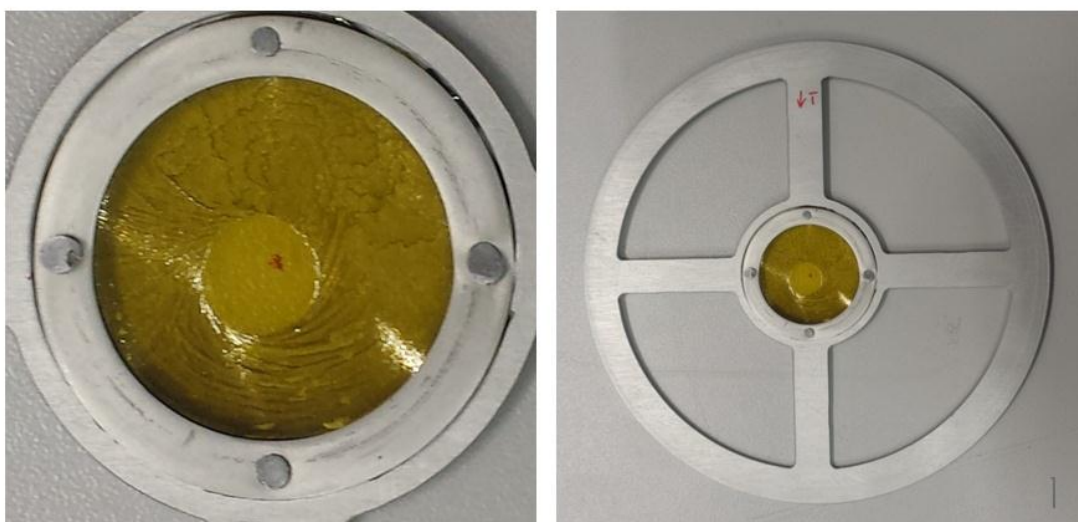

Figure 5.10: Left: Photo of the positron source used inside the small chamber. Right: The source and the four arms holder which is used with the small chamber, where the diameter of the holder is 138 mm which is equal to the inner diameter of the annihilation chamber [**89**].

The positrons pass through the vacuum and eventually stop at the surface of the Al material, during the bombardment of the inner wall of the small annihilation chamber with positrons as shown in Figure 5.2.

6. Calibration procedures of the J-PET detector

6.1. Calibration of effective light velocity in scintillator strips

6.1.1. The collimator

The design of lead collimator has taken the advantage of the symmetries of the J-PET detector, and thus the collimator assembly consists of two lead cylinders which are connected with screws placed in such a way that the beam of gamma quanta from the source will irradiate the central positions of all the detection modules strips at the same time. It also has an arms assembly, collimator support assembly and motor for collimator movement. In Figure 6.1 one can find a photograph of disks and arm assembly, and also collimator assembly inside the J-PET detector.

In order to hold this relatively heavy collimator, dedicated mechanical support arms are needed. Moreover, it should provide a precise determination of the position of the gamma emission plane along the z-axis. It turns out that the main difficulty which we have to deal with is the weight of the cylinders. Since the lead density is quite high, and arms supporting the collimator are exposed to big bending moments which may destroy the symmetry of the whole system and prevent precise measurements. Thus, to find dimensions of the lead cylinders giving best collimated beam with possibly lowest weight we have made calculations neglecting gamma quanta scattering. These calculations give also first approximations of expected beam profiles for the new collimator. The ^{22}Na source was placed inside of lead collimator with a 1.5 mm slit. Sodium source had an activity of around 18.5 MBq. Each lead cylinder of the collimator has dimensions of 3 cm (thickness) x 10 cm (radius) as shown in Figure 6.2. A mechanical step motor was used to move the collimator to the exact position along the whole length of scintillators with an accuracy better than 0.1 mm.
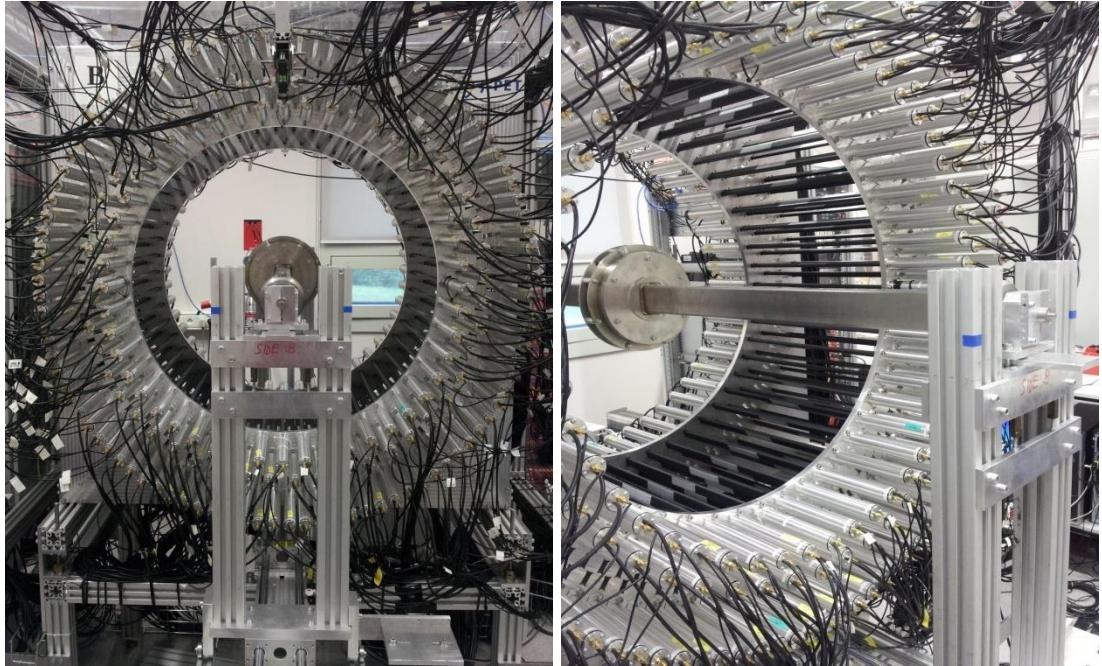

Figure 6.1: Photo of the J-PET detector with the collimator at the center.

6.1.2. Effective light velocity calibration measurements

The assembled collimator was placed at several positions along z-axis inside the J-PET detector. Each measurement took 30 minutes, the collimator was moved from -200 mm (close to A-side of the detector) through the center to the +200 mm position (close to B side). Then additional measurement at the central position was performed for 5 hours. Photomultiplier voltage and threshold settings were the same as during the long measurement with annihilation chamber.
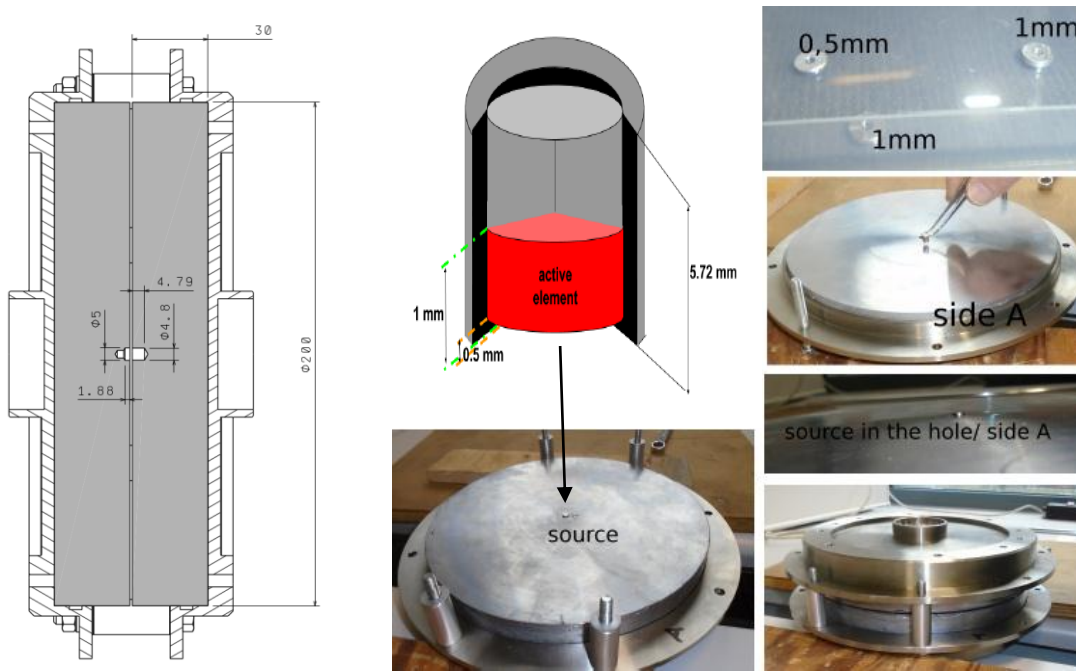

Figure 6.2: Left: Scheme of collimator disks. Each cylindrical disk of the collimator has 3 cm thickness. Middle:top scheme of source capsule with dimensions of the ^{22}Na source and placed inside collimator for big barrel. Distance from flat surface to an active element is equal to 0.5 mm. Middle bottom and Right: Proper placing of the source inside collimator disc. In side B there is a spring which pushes the source and prevents it from moving and shaking. Source is placed in the hole inside side A. Under the source in hole on side A there is placed one pad with 1 mm height, so the source protrude above collimator's disk surface. The size of slit of mounted collimator is equal to 1.5 mm [95].

The scan with the collimator for the four set of thresholds has been performed including the central position and for each position along z-axis.

6.1.3. The velocity calibration

The calibration measurements for the velocity of light signals in the scintillator have been done using the collimator. Using a scan at several positions along the whole length of the scintillator strip, with a predefined steps along z-axis (Figure 6.3).
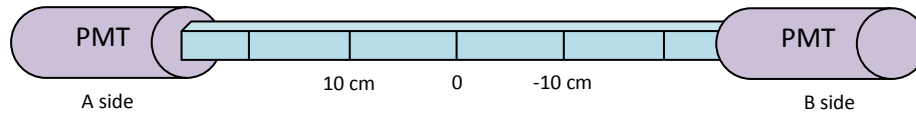
Figure 6.3: Different position of collimator according to scintillator inside J-PET detector. Center of the J-PET detector was marked as 0 position.

There was a series of measurements with collimator irradiating different z positions.

Assuming that the effective length = L, as shown in Figure 6.4.

$$Z - \text{position} = \text{Velocity} * (\text{Time B side} - \text{Time A side})/2 \tag{6.1}$$

For different assumed effective length the same calibration procedure was applied, to check how calibration constants changes with the change of effective length.
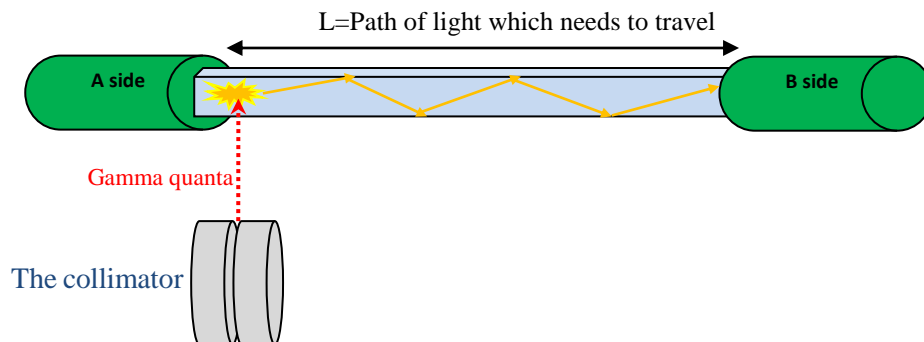

Figure 6.4: Scheme of the path of light which needs to travel through the scintillator strip of the J-PET detector.

6.2. Time calibration

The time calibration method of the J-PET detector based on the experimental measurements performed with a ^{22}Na radioactive source and a reference detector.

6.2.1. The reference detector measurements

The reference detector is a single PMT pointing in the direction of the measured scintillator strip (see Figure 6.5). It was mounted on a metallic arm. The angular position of this detector in the XY plane of J-PET was automatically set by a motor. A single measurement was performed with the reference detector pointing at the center of each scintillator strip and lasted 5 minutes. The radioactive source was pointing from a small distance to the J-PET strips, thus minimizing the error on gamma position with respect to the strip center.

6.2.2. Time calibration with reference detector

The measurements have been performed in counter-clockwise and anti-clockwise directions of moving the reference detector arm between irradiation of subsequent scintillator strips. Time of measurement for each strip was equal to 5 minutes. The reference detector settings were the same for both measurement orientations. The ^{22}Na source (UR451) has been inserted at the plastic cover on the top of the reference detector and connected with the reference detector arm in the J-PET detector. HV on reference detector was set to 1350 volts.
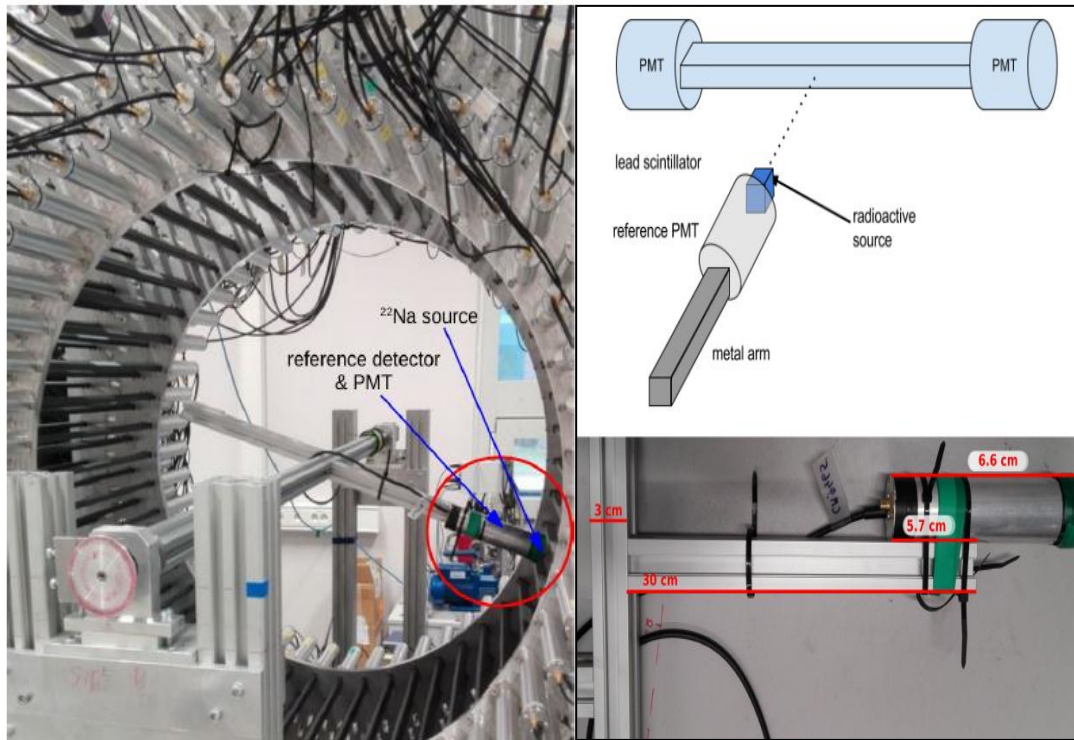

Figure 6.5: Left: Reference detector inside the J-PET detector seen from B side with a marked reference detector and ^{22}Na radioactive source. Top-Right: the reference detector and the plastic scintillator strip module alignment. Bottom-Right: The reference detector, PM tube and the detector arm holder.

The calibration measurements were performed with the reference detector such that radioactive source is pointing at the center of each strip as shown in Figure 6.6. The collected data of the reference detector measurements allow performing time calibration for each scintillator strip (synchronization between the photomultiplier signals from A and B side) as well as synchronization between neighboring strips and layers.
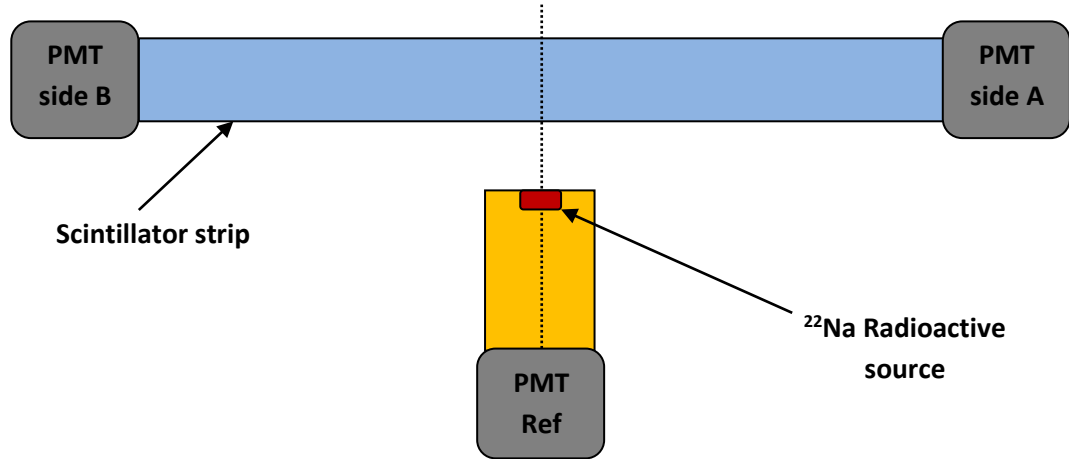

Figure 6.6: Scheme of the performed measurement for a single scintillator strip in J-PET. Scintillator strip, reference detector and photomultipliers are marked with blue, yellow and gray rectangles, respectively.

6.2.2.1. Determination of the time calibration offsets

This section presents the recipe of the time calibration of the J-PET taking into account the A-B sides synchronization and synchronization between strips and layers.

6.2.2.2. The A-B sides time synchronization

The A-B sides time synchronization of each strip in the J-PET has been done by assuming/fixing the following convention:

$$t_A = t_A^{true} - offset_A \text{ and } t_B = t_B^{true} - offset_B, \tag{6.3}$$
where:
t_A, t_B - times measured on side A and B, respectively,
t_A^{true}, t_B^{true} - the true times on side A and B, respectively,
$offset_A$, $offset_B$ - time offsets for side A and B, respectively.

The time difference between the left (B) and right (A) side of the strip is:
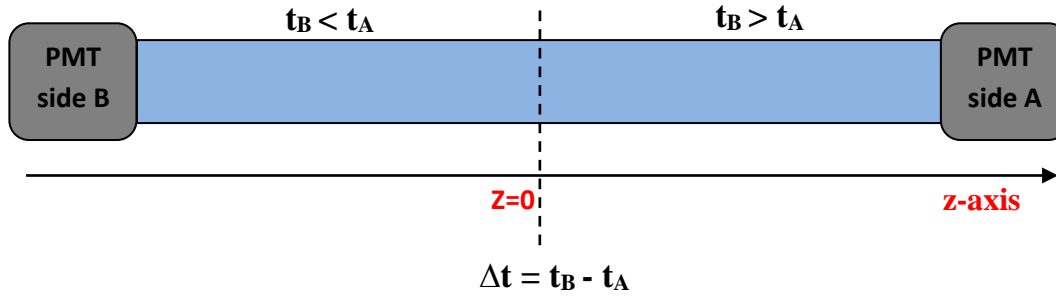$$\Delta t_{AB} = t_B - t_A \text{ as shown in Figure 6.7.} \tag{6.4}$$

Figure 6.7: Scheme of J-PET single strip with marked z-axis and the time difference between both sides.

3. Taking into account (6.3) and (6.4) we obtain following relation:

$\Delta t_{AB} = t_B - t_A = t_B{}^{true} - offset_B - (t_A{}^{true} - offset_A)$ (6.5)

In case of the measurement with the reference setup irradiating the center of the strip, $t_B{}^{true} - t_A{}^{true} = 0$ which allows for obtaining the first calibration constant:

$C_1 = \Delta t_{AB} = offset_A - offset_B$ (6.6)

6.2.2.3. The synchronization between strips

In order to perform simultaneous synchronization of the left-right sides and also between all strips in a layer, we should take into an account the time difference between each strip and the reference detector by using the following method:

$\Delta t_{hit} = t_{ABav} - t_{ref}$ (6.7)

where:

$t_{ABav} = (t_A + t_B)/2$ is the average time for strip,

t_{ref} is the time measured by a reference detector.

Which represents the times of recording photons from the same e+e- annihilation (the same event), where one photon goes to the scintillator strip and the other one to the reference detector.

Taking into account the equations (6.5) and (6.7) we obtain the following relation:

$\Delta t_{hit} = (t_B{}^{true} - offset_B + (t_A{}^{true} - offset_A))/2 - t_{ref}$

$(t_B{}^{true} + t_A{}^{true})/2 - t_{ref}$ = constant, since calibration is with respect to the reference detector. Further on we assume that constant = 0

Thus:

$\Delta t_{hit} = ((t_B{}^{true} + t_A{}^{true})/2 - t_{ref}) - (offset_A + offset_B)/2 = -(offset_A + offset_B)/2 = C_2$ (6.8)

By solving equations (6.5) and (6.8), we obtain following time offsets:

$offset_A = C_1/2 - C_2, offset_B = -C_1/2 - C_2$ (6.9)

6.2.2.4. The synchronization between layers

The synchronization between the three layers in the detector was carried out with respect to the first internal layer by applying the following method:

$$\Delta t_{hit}^{Li} = t_{AB_{av}}^{Li} - t_{ref}, \tag{6.10}$$

where:
$t_{AB_{av}}^{Li}$ average time for strip in i'th layer (i=1,2,3),

t_{ref} time measured by the reference detector.

Equation (6.10) refer to the case of recording times for photons emitted from the same e+e- annihilation, where one photon in the scintillator strip and the other one in the reference detector.
After correcting for the time offset, we obtain:
$$t_{AB_{av}}^{L2} = t_{AB_{av}}^{L1} + \Delta t_{L2-L1} \tag{6.11}$$
$$t_{AB_{av}}^{L3} = t_{AB_{av}}^{L1} + \Delta t_{L3-L1} \tag{6.12}$$
where:
$\Delta t_{L2-L1} = \Delta R_{L2-L1} / c =$ time difference of the photon propagating from layer 1 to layer 2,
$\Delta t_{L3-L1} = \Delta R_{L3-L1} / c =$ time difference of the photon propagating from layer 1 to layer 3,
ΔR_{L2-L1} is the distance between layer 1 and 2, ΔR_{L3-L1} is the distance between layer 1 and layer 3, c is the speed of light.

Taking into account equations (6.10), (6.11), and (6.12) we obtain:
$$C_{2=} t_{AB_{av}}^{L1} - t_{ref}, \tag{6.13}$$

We can define analogous constants for layer 2 (C_2^{L2}) and for layer 3 (C_2^{L3}), which should be obtained as in the following way:
For layer 2: $C_2^{L2} = C_2 + \Delta t_{L2-L1}$

For layer 3: $C_2^{L3} = C_2 + \Delta t_{L3-L1}$

6.2.3. Time calibration using 2 gamma back to back and de-excitation photon

The time calibration with the reference detector was very time consuming and required additional measurements, and thus the procedure explained further was used to apply additional time calibration and recalibrate the data. The new time calibration of large annihilation chamber data have been performed by using the following procedure [96]:

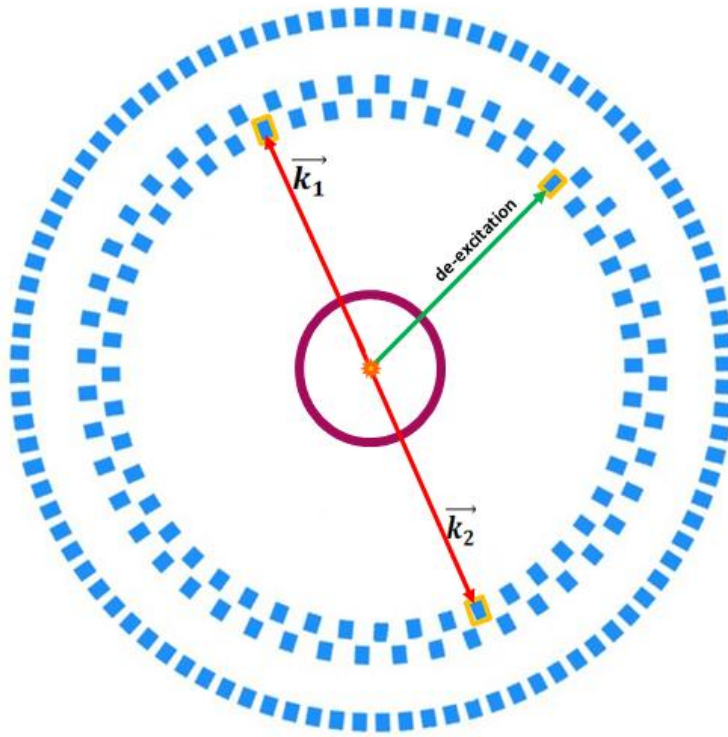1.Select events with 3-hits in a coincidence time window of 4 ns (see Figure 6.8).

Figure 6.8: The illustration view of the J-PET detector showing the e+e- annihilation into two back to back photons and one de-excitation (prompt) photon in the event happening at the center of the radioactive source.

2. Identifying annihilation and prompt photon candidates by checking if the hits have a time over threshold (TOT) in one of the following ranges (as indicated in Fig. 6.9):

- 24 ns $<$ TOT $<$ 36 ns – annihilation photon candidates hits,
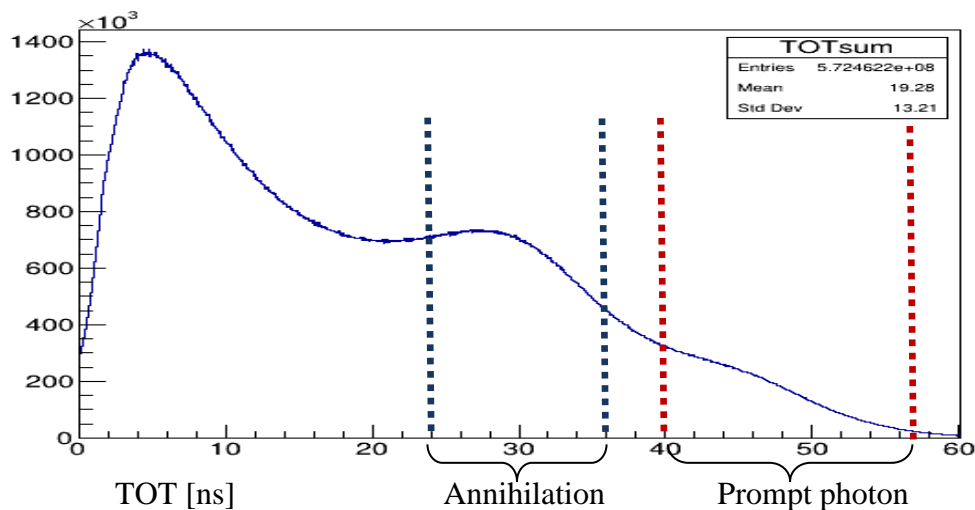- 40 ns $<$ TOT $<$ 57 ns - de-excitation photon candidates hits.

Figure 6.9: The time over threshold (TOT) values distributions calculated for interactions in all modules of J-PET detector. The region of TOT used to select annihilation photon candidates is marked with blue dashed lines, while the TOT region of de-excitation photons candidates is located between the red dashed lines.

Only events containing exactly 2 annihilation photons and 1 de-excitation photon candidates are used for calibration, other events are rejected.

4. For every such 3-hit event, we reconstruct the annihilation point from the lines of response (LORs), connecting the two hits identified as annihilation photons.

5. Accept and reconstruct the events with the annihilation points within the 2 cm radius around the chamber center in the XY plane and in the range of 5 cm along z-axis, as indicated in Figure 6.10.
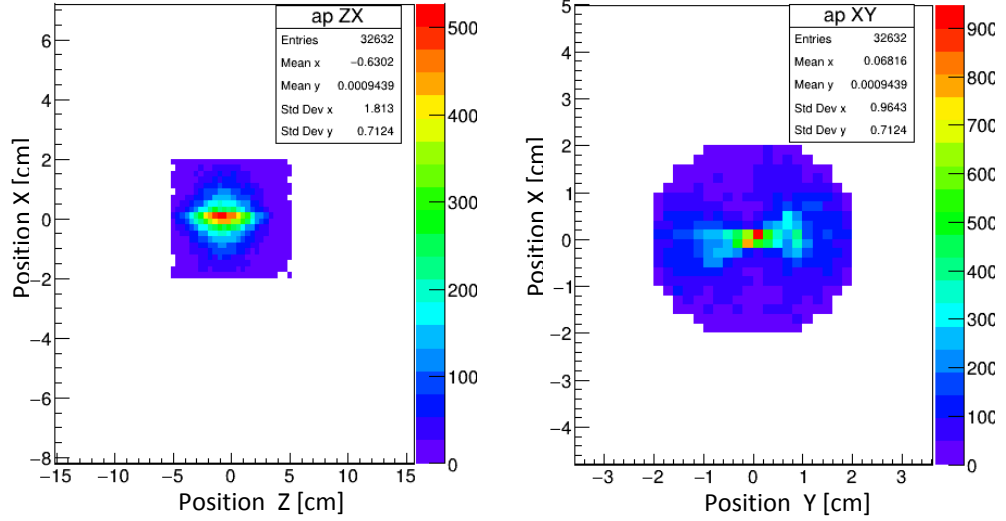

Figure 6.10: The annihilation points at the center (source region) within 2 cm transverse radius and $\pm$ 5 cm along z-axis, obtained using e+e- $\rightarrow 2\gamma$ and Ps $\rightarrow 2\gamma$ annihilations.

6. Correct the hit recording times for the time of flight (TOF) from the annihilation point to the hit for all the 3 hits of the event. In order to do that we take the distance from the annihilation point to the hit (d), and obtain the gamma emission time as:

$T_{emission} = T_{hit} - d/c$,

Where d is the distance between the annihilation point and the hit position and we have to do it for every hit i.e 2-hit from back to back (BTB) and also for the prompt, assuming that all of them came from the same annihilation point.

7. Accept events where the azimuthal angles between two annihilation hits measured with respect to the center of the detector are in the range: $174^o <$ angle $< 186^o$.

Such selected events are used to construct two kinds of time difference spectra separately for every detection module of the J-PET detector:

- Time difference between emission of one of the annihilation photons recorded in the given detection module and emission of the corresponding de-excitation photon, recorded in any of the J-PET detection modules (Figure 6.11).

- Time difference between emission of an annihilation photon recorded in any J-PET detection module and emission of the corresponding de-excitation photon recorded in the given detection module (Figure 6.12).

For each of the J-PET detection modules, the mean values of the time difference distributions defined above were extracted and used to construct time calibration corrections for each module.
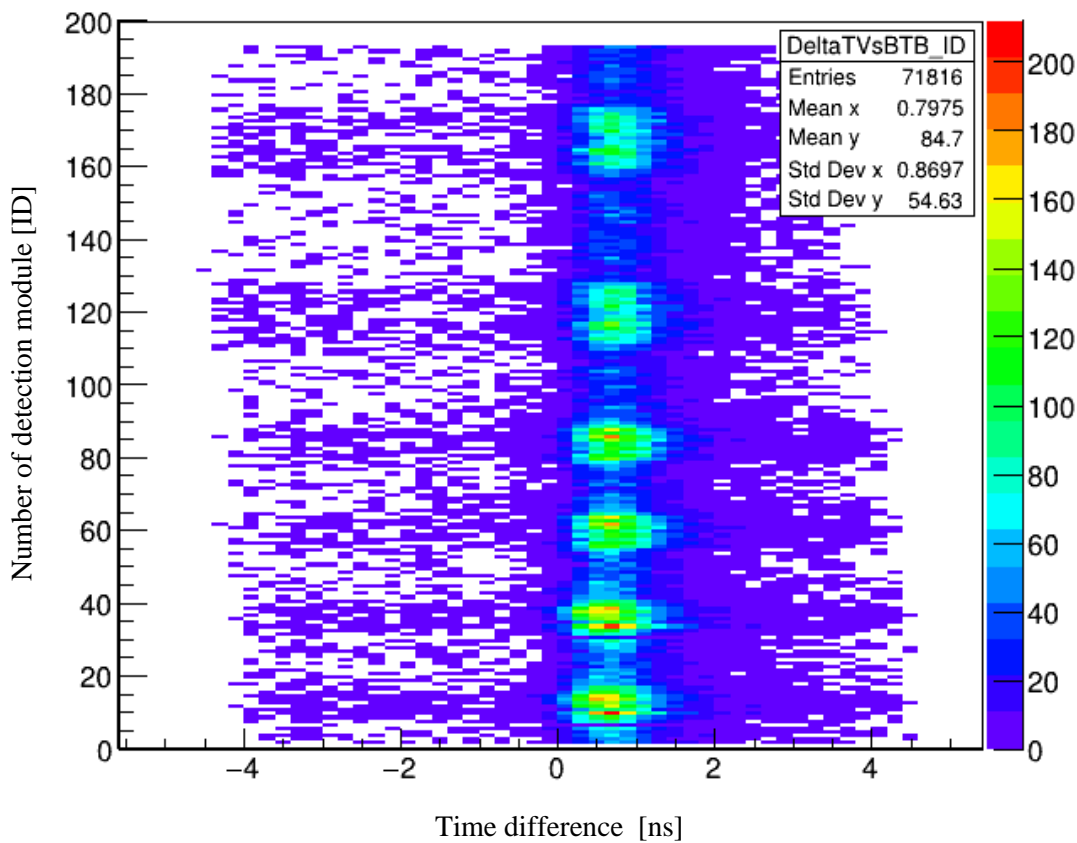

Figure 6.11: The time difference between emission of one of the annihilation photons recorded in the given detection module (identified by its ID on the vertical axis) and emission of the corresponding de-excitation photon (prompt hit) recorded in any of the J-PET detection modules.
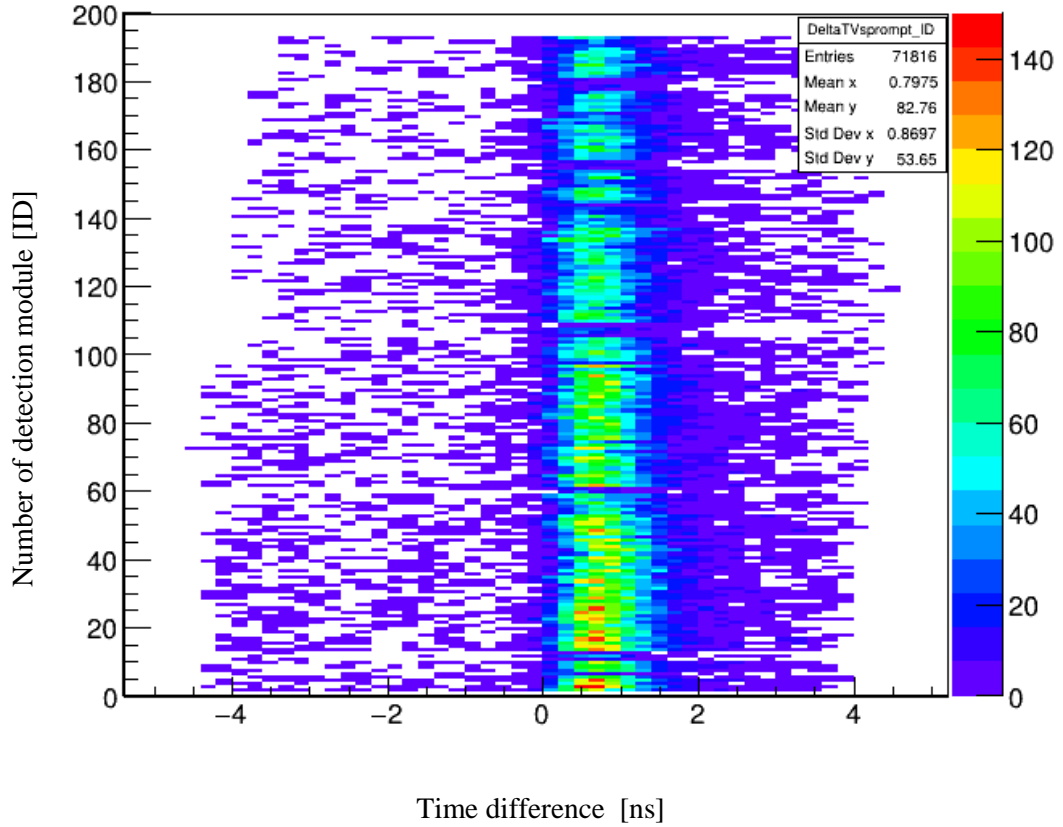
Figure 6.12: The time difference between emission of an annihilation photon recorded in any J-PET detection module and the emission of the corresponding de-excitation photon recorded in the given detection module (identified by its ID on the vertical axis).

Calculate and plot the histogram for each scintillator ID for both above cases, and determine the mean value for each scintillator ID, then correction for scintillator:

Correction for scintillator's $ID_{time} = (mean_{BTB\_Annihilation} - mean_{prompt})/2$

From the two histograms in Figures (6.11) and (6.12), we extracted the mean for each scintillator ID, where we have assumption that the recorded time of de-excitation and annihilation include the offset for a given scintillator strip. As shown in Figures (6.13-6.18).
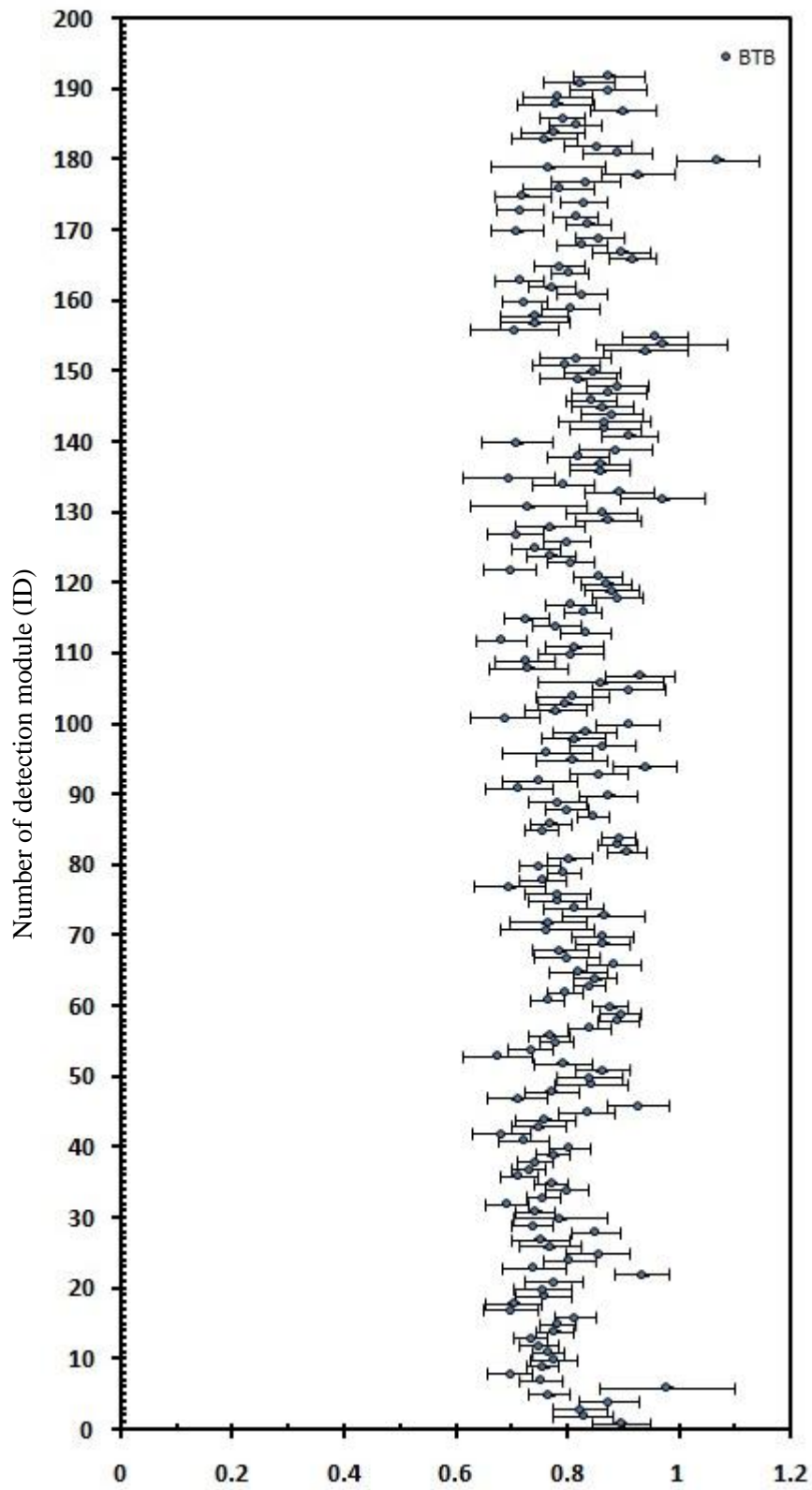
Mean values of the distribution from Fig. 6.11 [ns]

Figure 6.13: The histogram of the mean time for each scintillator ID for the case of BTB versus scintillator ID.
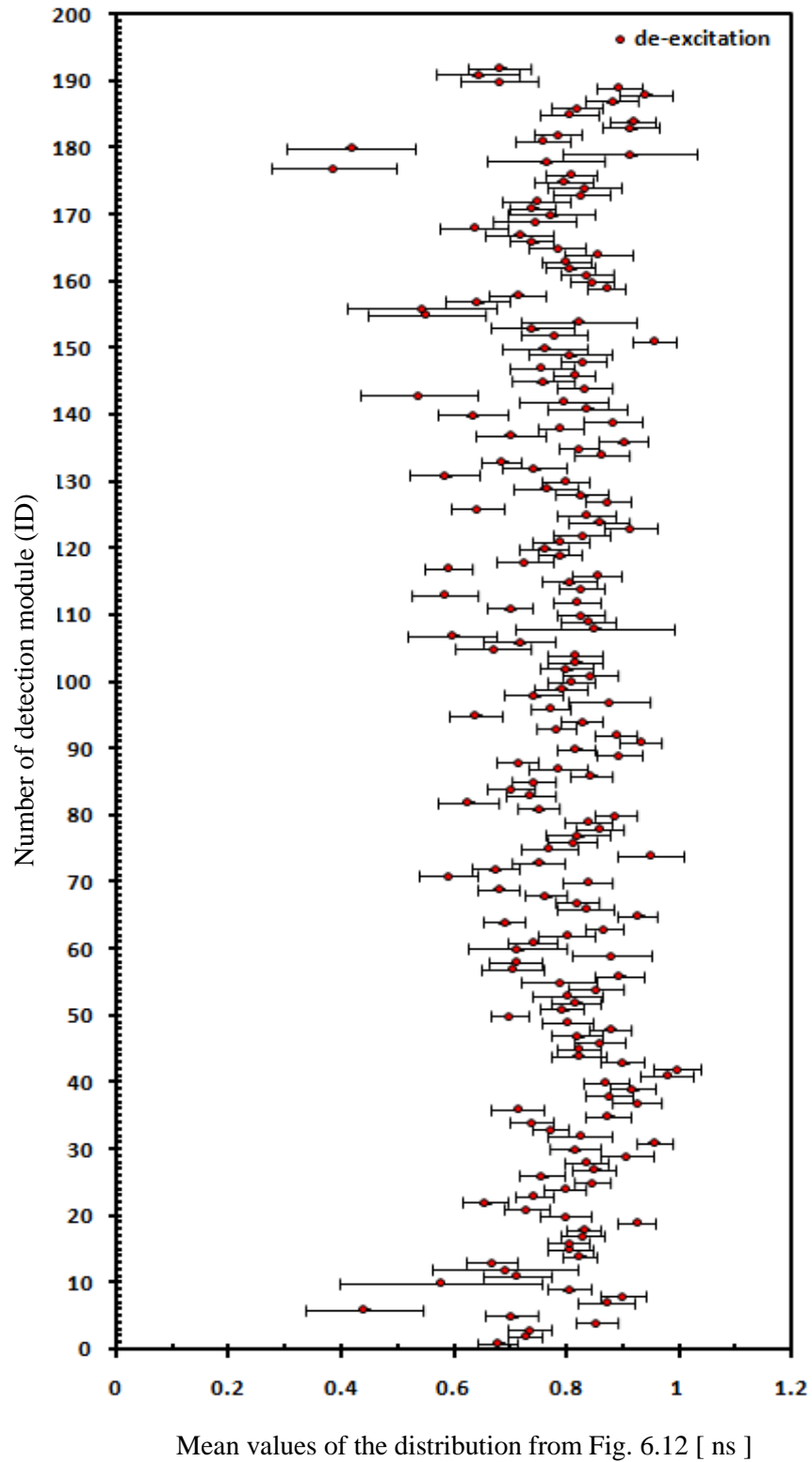
Figure 6.14: The histogram of the mean time for each scintillator ID for the case of de-excitation versus scintillator ID.
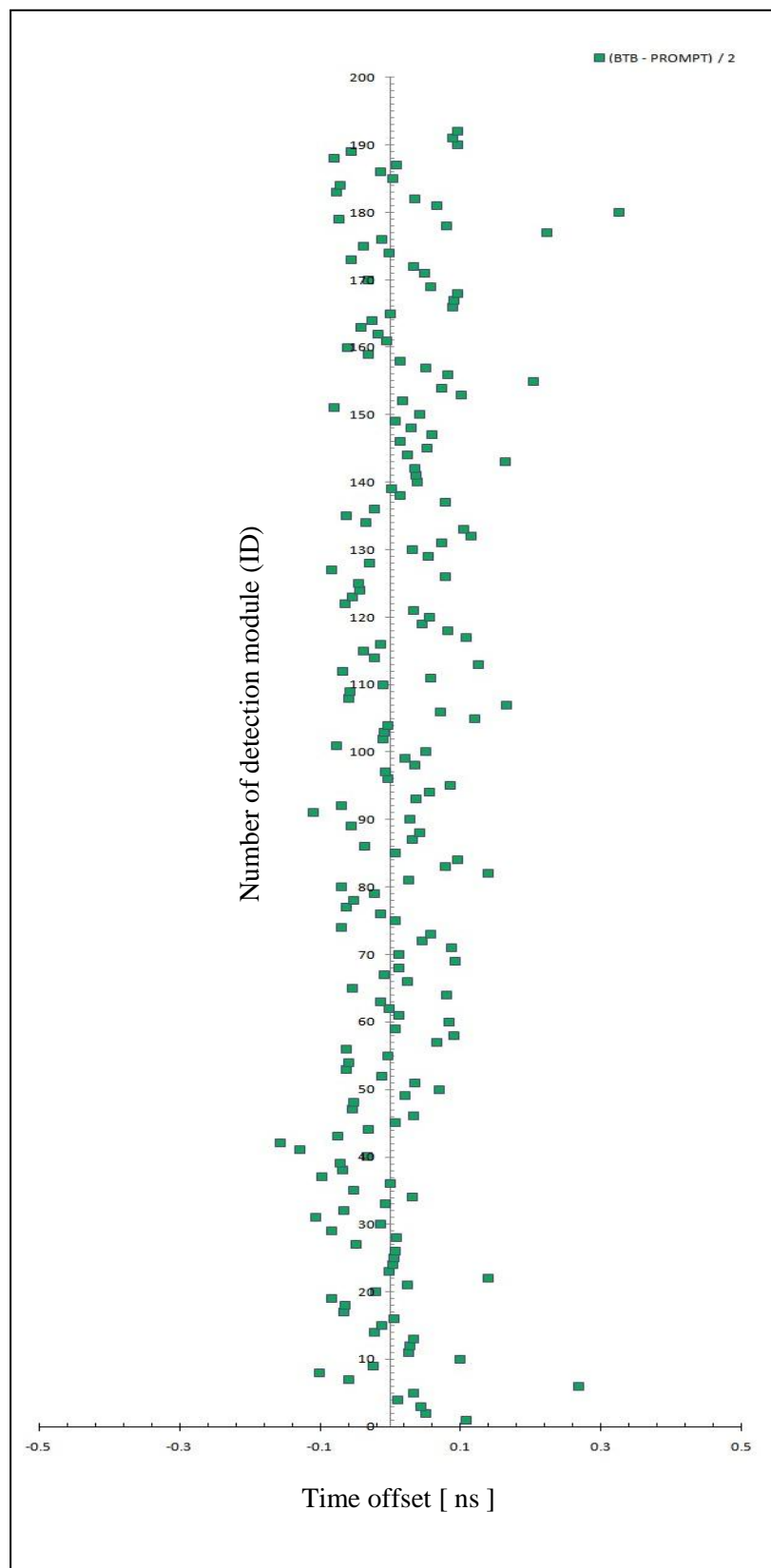
Figure 6.15: The histogram of the time offset versus scintillator ID.

Time offset = 1/2 (Mean BTB − Mean Prompt)
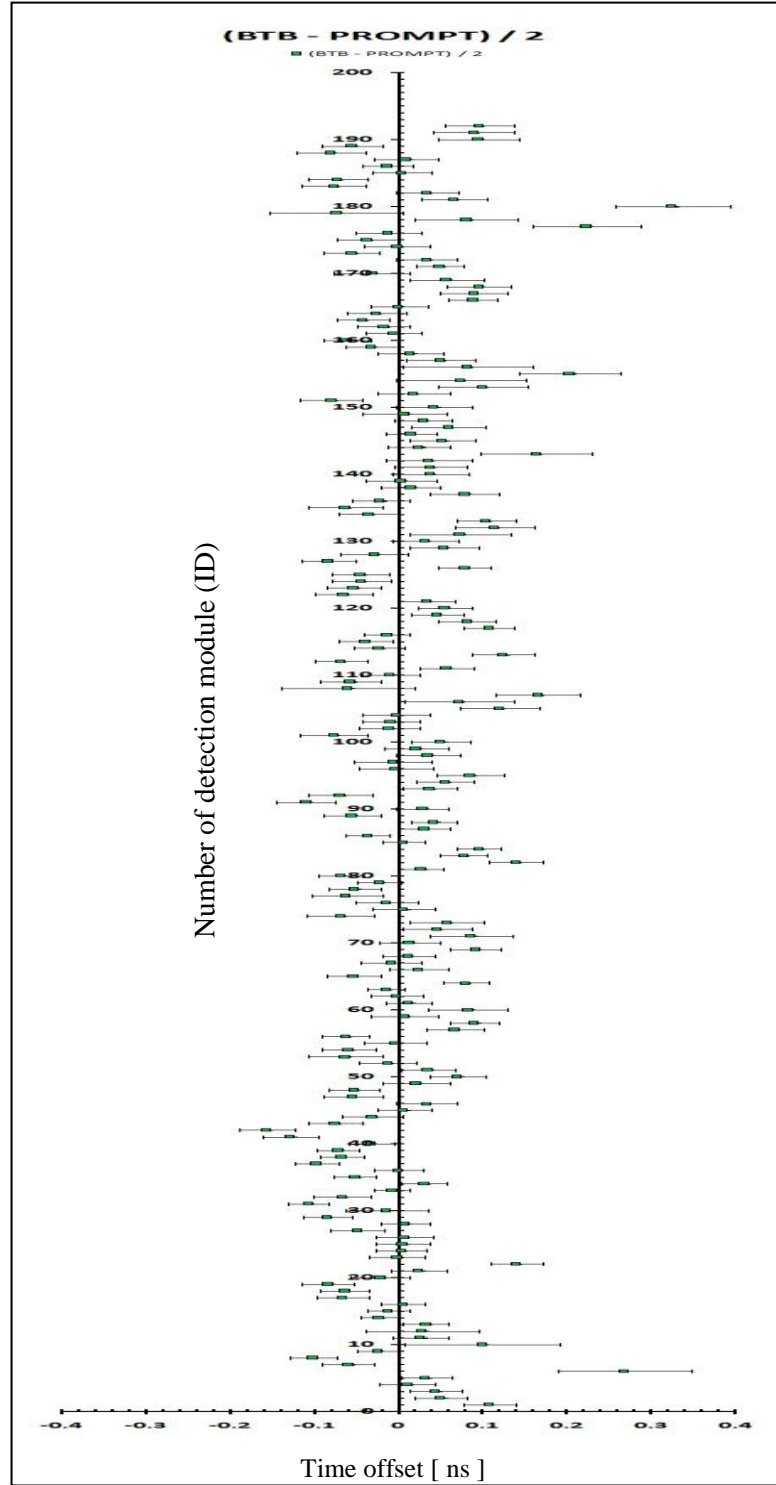
Figure 6.16: The time offset with error versus the number of detection module (ID)

$$\sigma(\Delta t) = \frac{1}{2}\sqrt{\sigma^2(annihillation) + \sigma^2(prompt)}$$

1st iteration
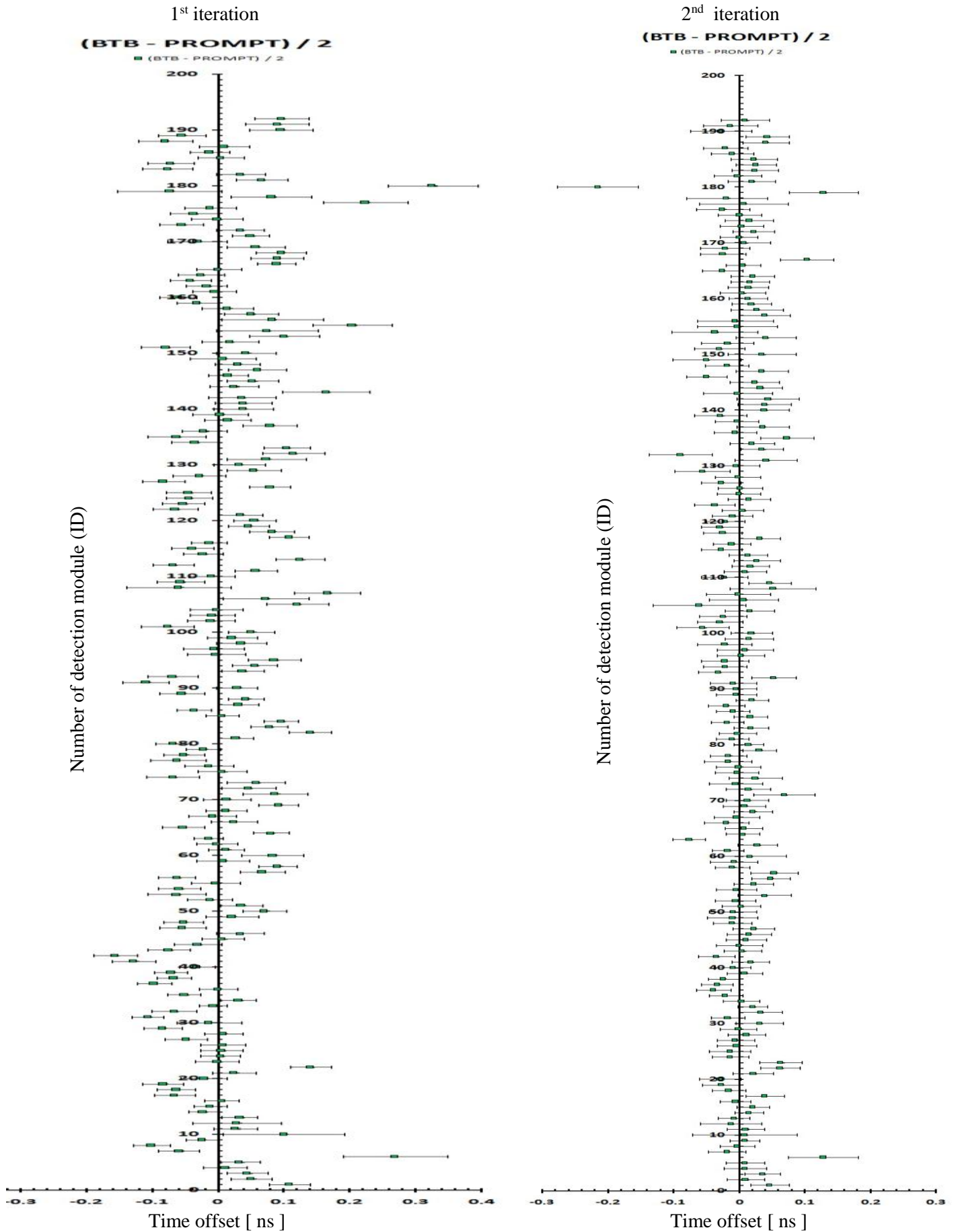
2nd iteration

Figure 6.17: The time offset with error versus the number of detection module (ID), obtained in subsequent iterations of the procedure presented in Fig. 6.16.
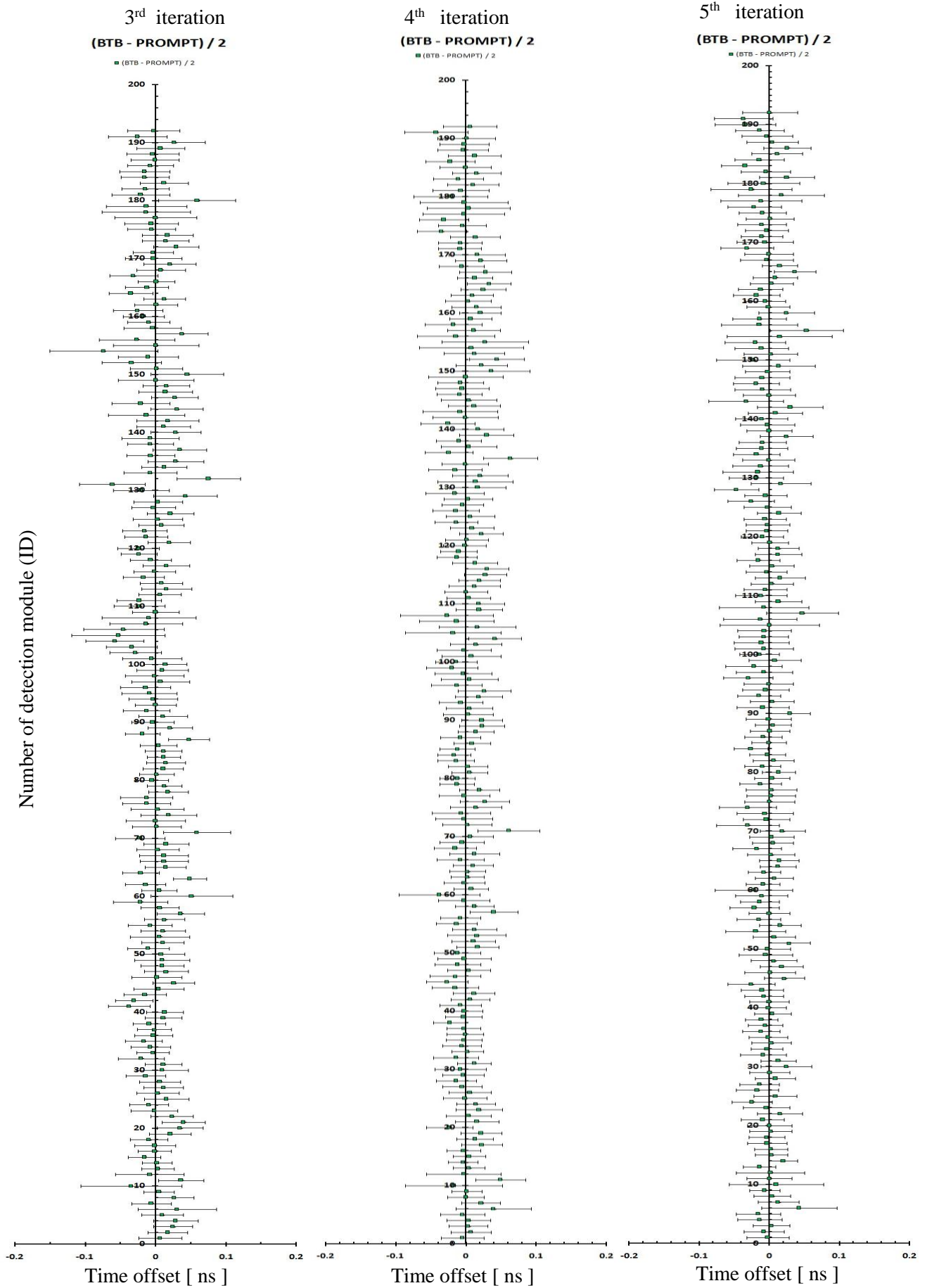
Figure 6.18: The time offset with error versus the number of detection module (ID), obtained in subsequent iterations of the procedure presented in Fig. 6.16.

7. The data analysis

7.1. The J-PET data reconstruction and preselection

The large annihilation chamber measurements were performed for 57 days, resulting in a total of 260 TB of collected raw data. The reduction of such a high data stream resulting from the trigger-less mode of data acquisition of the J-PET detector [97], requires stringent discrimination of background (coming mostly from 2ɣ annihilations) already at the early stages of data processing to allow for effective analysis. The data analysis was performed using the J-PET Framework Analysis software [83]. At the first level of data analysis, single times recorded at certain voltage thresholds values which were applied to the electric signals of the PMT were assembled into representations of the original PMT signals. For each PMT output signal, the Time Over Threshold (TOT) value as explained in Section 7.6.1 was recorded using the information on all the four thresholds. Later, each pair of signals which come from the same hit were identified and counted from two sides of the same scintillator. The pair of signals corresponding to the same hit should be originated from the same scintillator strip and their arrival times (the time at the leading edge on the lowest voltage threshold) should have an interval less than 5 ns, determined by the maximum effective time of light propagation along the whole length of a scintillator strip.

The last stage of the data reconstruction includes collecting the event candidates as a set of hits that were recorded within a time window of 20 ns. Such a time window value is broad concerning the possible time differences in a real event, in order to reduce the size of data without limiting the further fine selection criteria of the event candidates by the strict value of the required timing interval. In the current data analysis, only candidates with at least 2 or 3 hits in the event within 20 ns were accepted for further analysis, and after such preselection, the data returned for further analysis is reduced to about 0.2% of the original volume of the raw data.

7.2. The application of the calibrations

During the execution of the data reconstruction procedures, all the calibrations which were mentioned in chapter 6, including the Time-Over-Threshold calibration, calibration of time synchronization, the effective speed of light calibration, and TDC non-linearity corrections, were applied.

7.3. The data pre-selection criteria

7.3.1. The criteria based on the times over threshold

Time Over Threshold is used in the J-PET detector to determine the energy response of scintillators strips. The time over a threshold value is widely used to describe signals from different kinds of detectors in the field of particle physics [98]. The TOT technique is well suited to build multi-channel readout systems for pixilated detectors [99]. The main limitation of the TOT method is that the relation between the input charge to be measured and the width of the encoded pulse signal is non-linear. Figure 7.1 shows a scheme of a probing signal at four thresholds with 4 points on the leading edge and at the trailing edge of the signal, which allows for reconstructing the original signal shape.
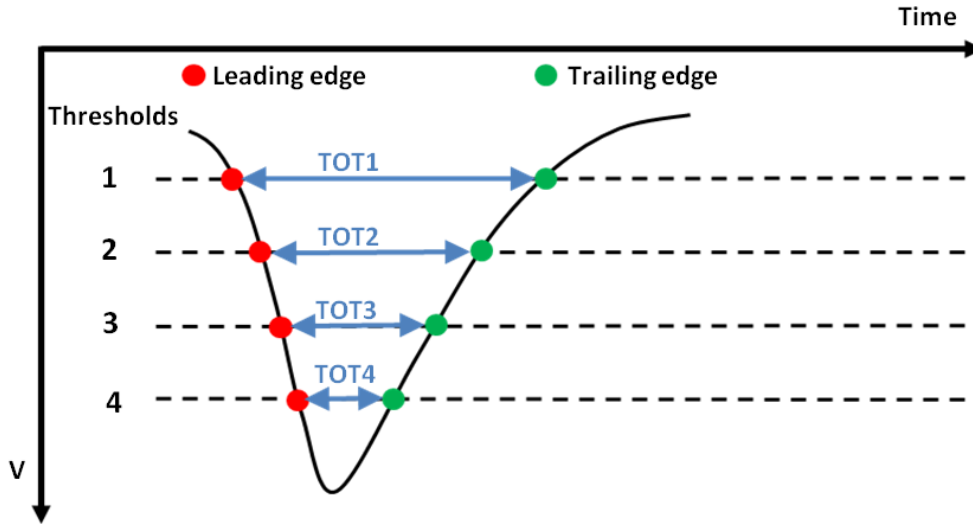
Figure 7.1: The recorded signal is sampled at four voltage threshold levels (dashed black lines). Each signal crossing a given threshold is registered at both leading and trailing edge (red and green dots respectively). The value of deposited energy can be estimated using the sum of registered times over threshold (TOT) for all four thresholds crossed by the signal, which allows for reconstructing the original signal's amplitude and shape.

After the pre-selection of the event candidates, we can estimate the deposited energy of gamma quanta interacting in the scintillator strips. The total sum of times over threshold of the two signals constituting a hit is calculated as a measure of the deposited energy of gamma quanta. A histogram of the sum of TOT values is shown in Figure 7.2. However, such estimation method of the deposited energy values is very sensitive to the detector properties such as the photomultipliers gain. Therefore, a TOT calibration was done for the small chamber experiment in order to remove this effect.

Figure 7.2: The histogram of the sum of TOT values from four thresholds of each strip in the J-PET detector in two different experiments with a different set of thresholds and a different ratio of 3ɣ to 2ɣ events. Left: The experiment with small annihilation chamber. Right: The experiment with a large annihilation chamber.

7.4. The procedure of J-PET data reconstruction

The reconstruction procedure of J-PET data is a multi-stage process based on dedicated framework analysis software [**83**]. The Data Analysis Framework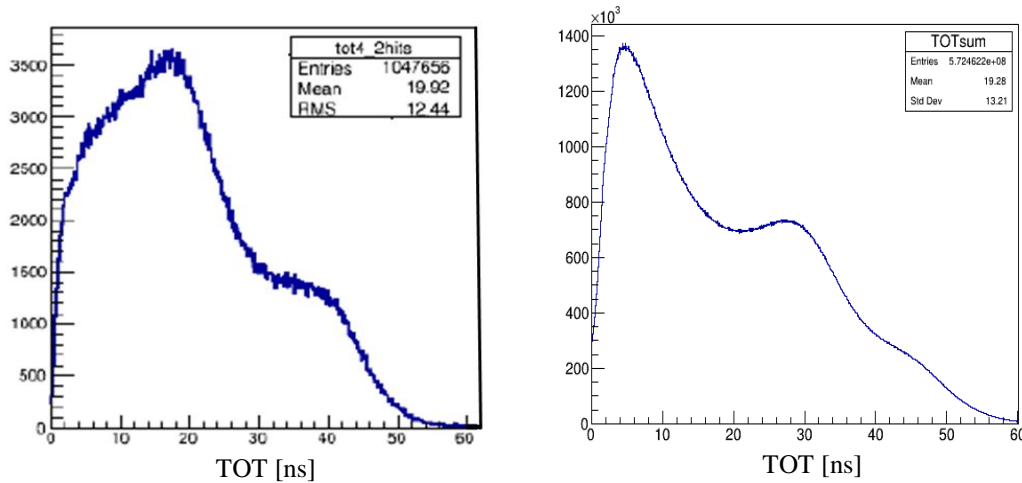 for J-PET experiment is a flexible environment software for both on-line and off-line data reconstruction procedures, which includes: fundamental physics analyses, medical imaging, detector calibration. The J-PET data analysis consists of several modules. Each of them corresponds to a particular computing task e.g. time calibration procedure or data reconstruction algorithm. The J-PET framework user can choose between available modules of reconstruction algorithms or create special analysis modules and easily include them in the chain of data processing. A scheme of the data processing sequence is shown in Figure 7.3.
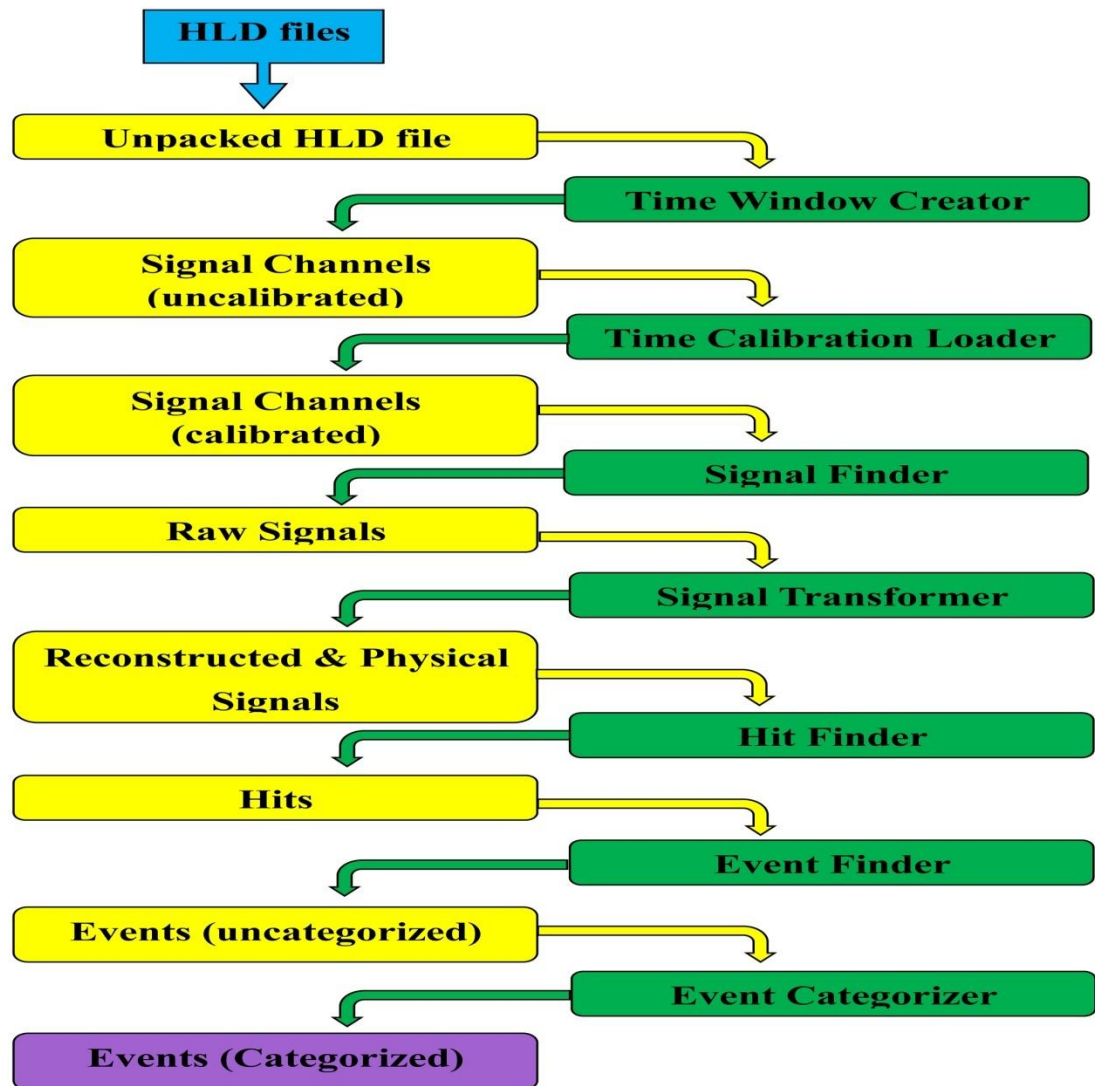
Figure 7.3: Diagram of data processing by the J-PET Framework Analysis software. The input data (TDC times) were recorded and delivered by the data acquisition system (DAQ) as HLD (raw data) files shown in the blue rectangle. The green rectangles represent the computational tasks responsible for some reconstruction algorithm or time calibration etc., yellow rectangles represent the reconstructed physical quantities e.g. signals, hits (photon interaction points) at the scintillator strip and events, which leads to the output in the purple rectangle.

7.5. The image reconstruction of the cylindrical annihilation chambers

The e+e- annihilation points reconstruction (2γ imaging) was performed for several reasons: a benchmark to the 3γ annihilation points, understanding the detector acceptance, and also for checking the positioning of the chamber with respect to the detector.

7.5.1. The 2-gamma annihilation points reconstruction

The first set of measurements using J-PET detector implementing the scheme discussed in Section 5.3 were performed with a small annihilation chamber (aluminum vacuum chamber) with a radius of about 7 cm depicted in Figure 7.4 left and 10 MBq sodium source was used as a positron source. The positron source was placed in the form of ^{22}Na enclosed by two layers of Kapton foil inside the cylindrical aluminum chamber. In these test measurements, the positrons were mostly annihilating in the aluminum wall by emitting two back to back photons, but there was also a small possibility for 3γ events from direct three-photon e+e- annihilation. The other criterion imposed on the two-hits events to identify annihilations into two back to back photons was based on the angular topology of the 2γ event.

The relative azimuthal angle between the locations of detection modules has been observed which recorded photons is in the range Θ=180º $\pm$ 19º (the highly populated region around 180º) in the case of the small cylindrical annihilation chamber with 7 cm radius as shown in Figure 7.4.

This requirement imposed on the difference of azimuthal angles of recorded photon interactions was determined using the following geometrical reasoning. The decay point has to be located on the walls of the chamber and the angles are calculated with respect to the center of J-PET detector (as indicated in Figures 7.4) using a following formula:

$\theta_{min} = 2 * \cos^{-1}\left(\frac{r}{R}\right)$, where, r is the radius of the annihilation chamber, and R is the radius of the 1st layer of the J-PET detector, where it is enough to consider the effect of the smallest radius layer of the detector (1st layer), in order to get the maximum width of the θ-band around 180º.

$\theta_{min} = 2 * \cos^{-1}\left(\frac{7}{42.5}\right) = 161^{o}$

$\theta_{max} = 360^{o} - 161^{o} = 199^{o}$

The events from two gamma photons annihilations, which contain two photons with opposite momenta, are expected to be congregated in a vertical band. Figure 7.4 shows that indeed there is an excess of events in the expected range of 180º$\pm$19º.
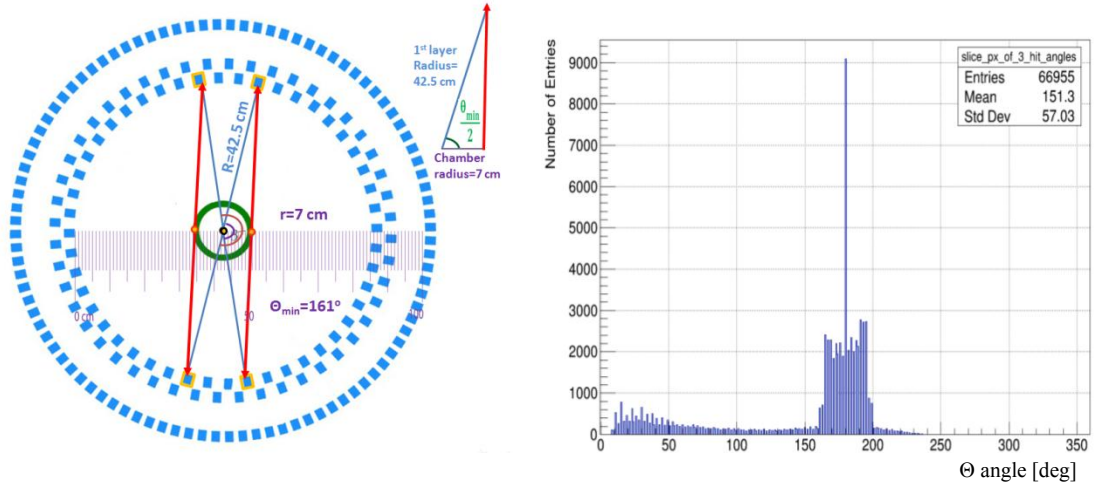
Figure 7.4: Left: The illustration view of the J-PET detector showing the maximum and minimum values of the range of angles between two gamma back to back decay at the wall of the small cylindrical annihilation chamber with 7 cm radius, measured with respect to the center of the detector. Right: The distribution of the Θ angles between 2-hit in the case of a small annihilation chamber experiment showing the events from two gamma photons annihilations, which contain two photons with opposite momenta, are congregated in a vertical band symmetrically around 180º.

In the case of the large annihilation chamber with 12 cm radius, the possible min/max values of the azimuthal angles between the two hits are equal to:

$$\theta_{min} = 2 * \cos^{-1}\left(\frac{12}{42.5}\right) = 147^o$$

$$\theta_{max} = 360^o - 147^o = 213^o$$

In this case, the relative range of angles between the two photon's momenta has the range Θ=180º $\pm$ 33º, as shown in Figure 7.5 left.
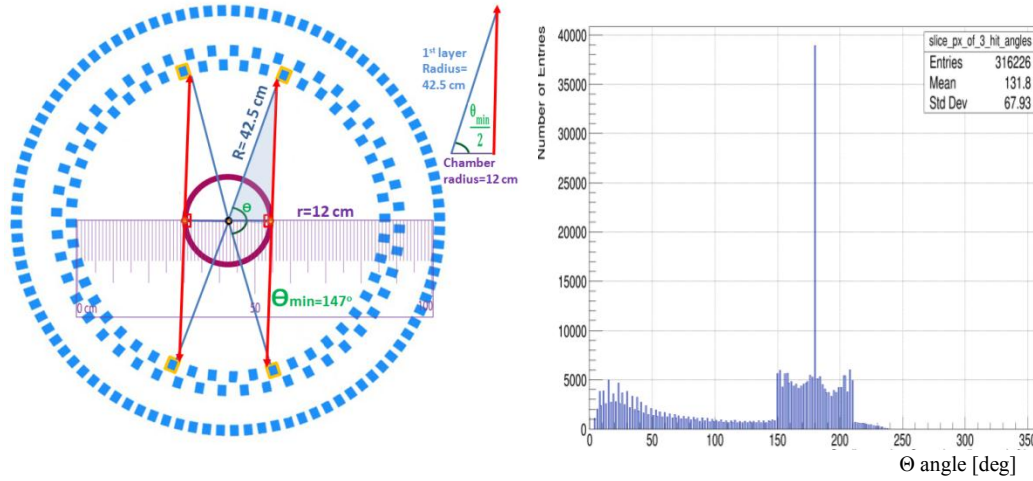
Figure 7.5: Left: The illustration view of the J-PET detector showing the maximum and minimum values of angles between two gamma back to back decay at the wall of the large cylindrical annihilation chamber with a 12 cm radius, measured with respect to the center of the detector. Right: The distribution of the Θ angles between 2 hits concerning the geometrical center of the detector for the case of large chamber experiment. The events from two gamma photons annihilations, which contain two photons with opposite momenta, are congregated in a vertical band symmetrically around 180°.

The single event can be described as a set of two hits happened within a narrow time window of about 4 ns. In the case of the event which has only two hits recorded within the same time window, the probability that one of the two observed hits corresponds to a high-energy de-excitation photon (1.275 MeV when the ^{22}Na radioactive isotope is used in the measurements) is comparable to the chance of observing a photon from the 2γ annihilation. Conversely, for the pre-selection criteria which required more hits in coincidence, the influence of de-excitation photons on the spectrum of TOT is decreased.

For each event, registered time values were corrected with time calibration constants. The field of view of the imaging by J-PET detector in x and y plane was limited to circle with a diameter equal to 50 cm. Consequently, only those events which have a distance between the line-of-response (LOR) connecting hits and the geometrical center of the J-PET detector smaller than 25 cm were accepted for the annihilation points reconstruction [100].

The data pre-selection procedure was also done by using the criterion based on the reconstructed energy loss of the photon. The energy loss was estimated based on the sum of time-over-threshold (TOT) values measured at four thresholds values which have been discussed in details in Section 7.3.1.

The TOT spectrum contains the structures from Compton spectra for photons from annihilation candidates and high energetic de-excitation photons candidates.
The lower limit of TOT value corresponds to the low values of deposited gamma energy. Applying this criterion reduces the contribution of hits that originate from secondary photon scatterings in the strips of the J-PET detector, while the upper limit

of the TOT values decreases the contribution from the photons with energy of 1.27 MeV which come from the ^{22}Ne* de-excitation.

Moreover, the z-coordinate of the place of interaction of quantum within the scintillator strip was limited to $\pm$23 cm within the active range of the scintillators. The events with hits that have larger values of z-coordinate were rejected. This limitation was motivated by the possibility of gamma quanta scattering on mounting plates near the edges of the strips where the scintillators are connected to the PMTs as well as by worsening of the resolution for hits close to strip ends.

The annihilation points distributions for the large plastic annihilation chamber with a 12 cm radius and a small Al annihilation chamber with a 7 cm radius are shown in Figure 7.6 after applied cuts which allowed for background rejection. The hit time and hit position of each gamma quantum interaction with the J-PET scintillator strips were used for image reconstruction of the large and small annihilation chambers walls performed by a dedicated MLEM algorithm as shown in Figure 7.7.
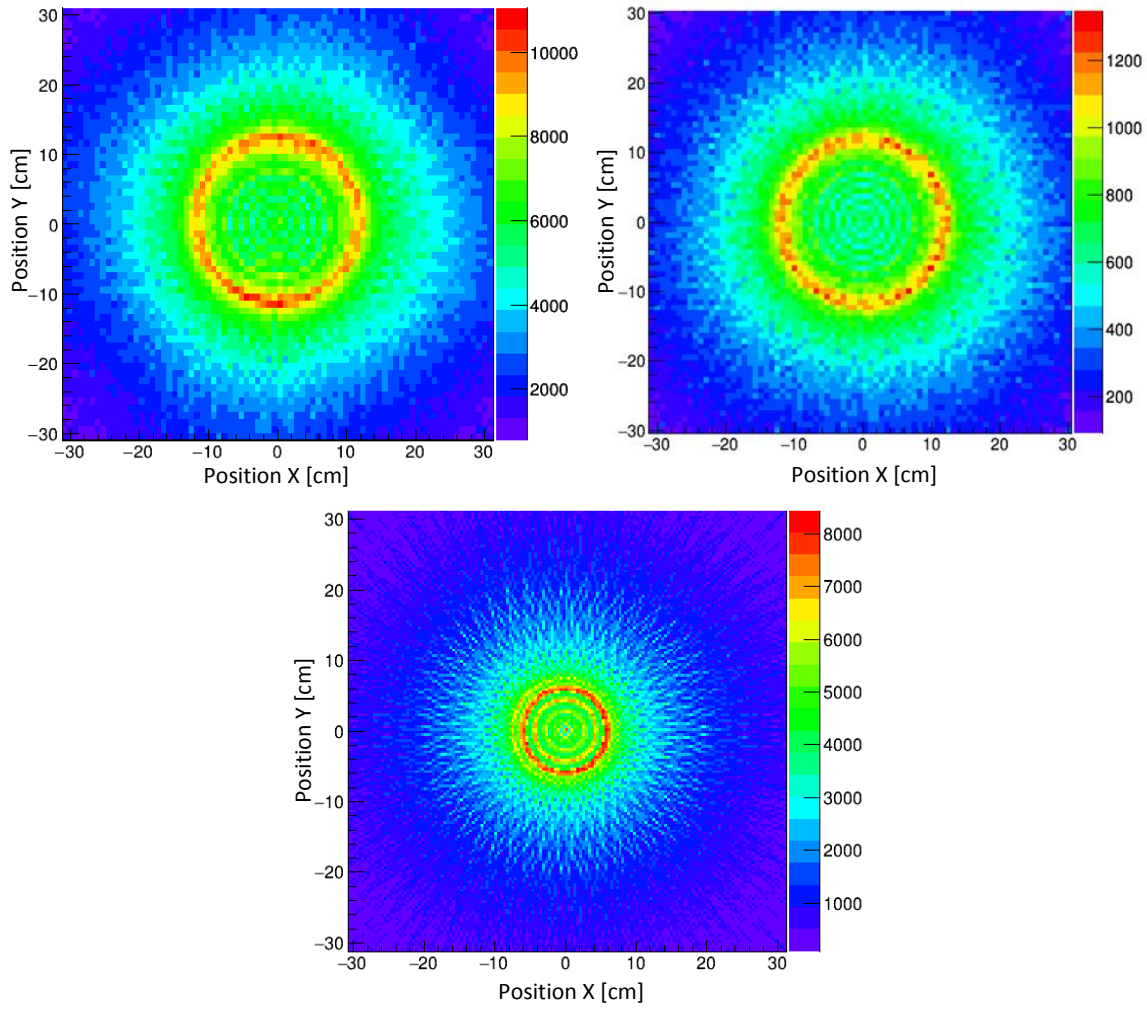
Figure 7.6: The distribution of annihilation points of the large annihilation chamber using 10 MBq source (top-left), large annihilation chamber using 1 MBq source (top-right), the small cylinder annihilation chamber (bottom), obtained using e+e- $\rightarrow$ 2ɣ annihilations used as a benchmark for the 3-gamma annihilation reconstruction, where z=$\pm$5 cm has been excluded to reduce the effect of annihilations taking place in the β^+ source setup.
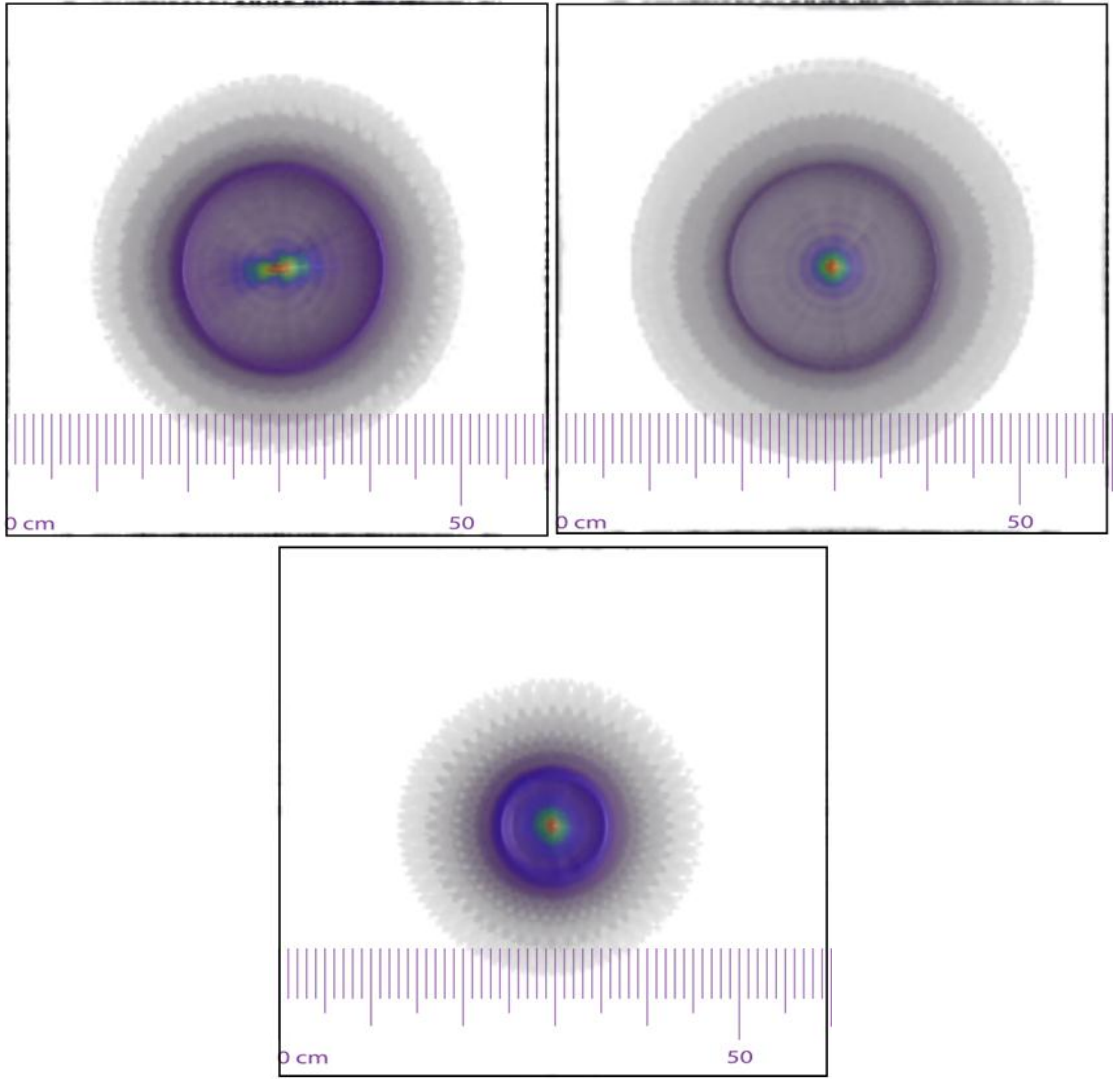
Figure 7.7: Tomographic images in the transverse view (xy) of the cylindrical annihilation chambers obtained using e+e-→2ɣ annihilations and MLEM images reconstruction. Top: images of the large chamber in measurements with 10 MBq source (left) and 1 MBq source (right). Bottom: the image of the small chamber in the measurement with 10 MBq source.

The 2ɣ images were used to check the positioning of the annihilation chamber and the source setup, reveling imperfect alignment in case of the measurement with a 10 MBq source.

The transverse image for the large annihilation chamber measurement with 10 MBq ^{22}Na source, and longitudinal image in the yz-plane (top view) is shown in Figure 7.8 and side image xz-plane is shown in Figure 7.9. The observed distribution shows that that the source holder is tilted (rotated) by a few degrees around x-axis and also shifted about -6 mm along z-axis. It means the source was not exactly aligned at the geometrical center of the detector as expected from the considerations presented in the Section (5.3). The discovered offset along z-axis was taken into account in the analysis presented in the next sections.

Figure 7.8: 2ɣ longitudinal images of the central region of the large annihilation chamber in the measurement with 10 MBq source. Left: The YZ view reveals an effect of the source setup being tilted with respect to the transverse (xy) plane. Right: The XZ view shows that the source position along the z-axis was not at the geometrical center of the detector.

Figure 7.9: 2ɣ longitudinal images of the central region of the large annihilation chamber in the measurement with 1 MBq source. Left: The YZ view of the annihilation points distribution which shows that the s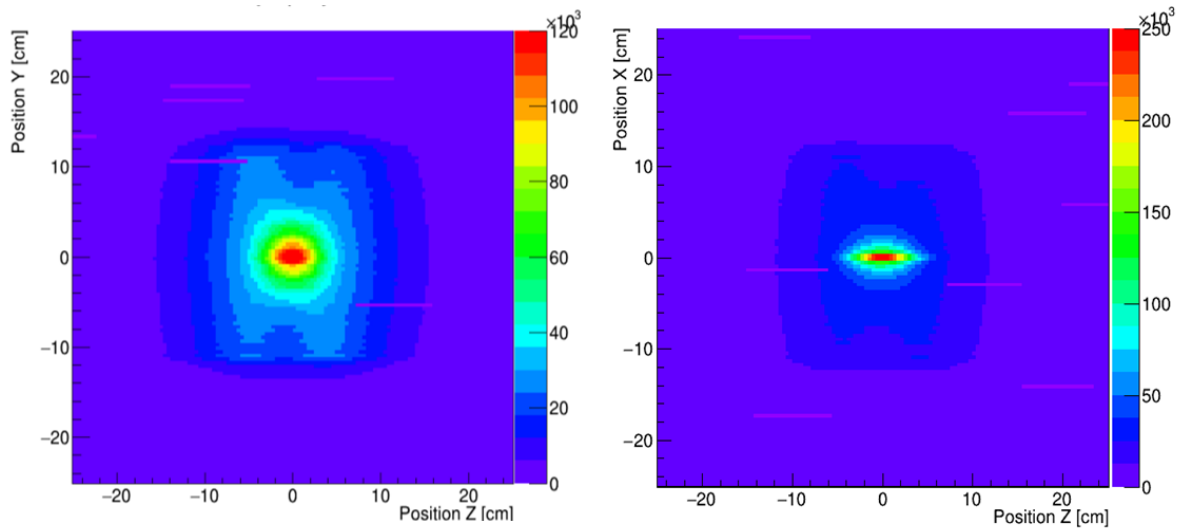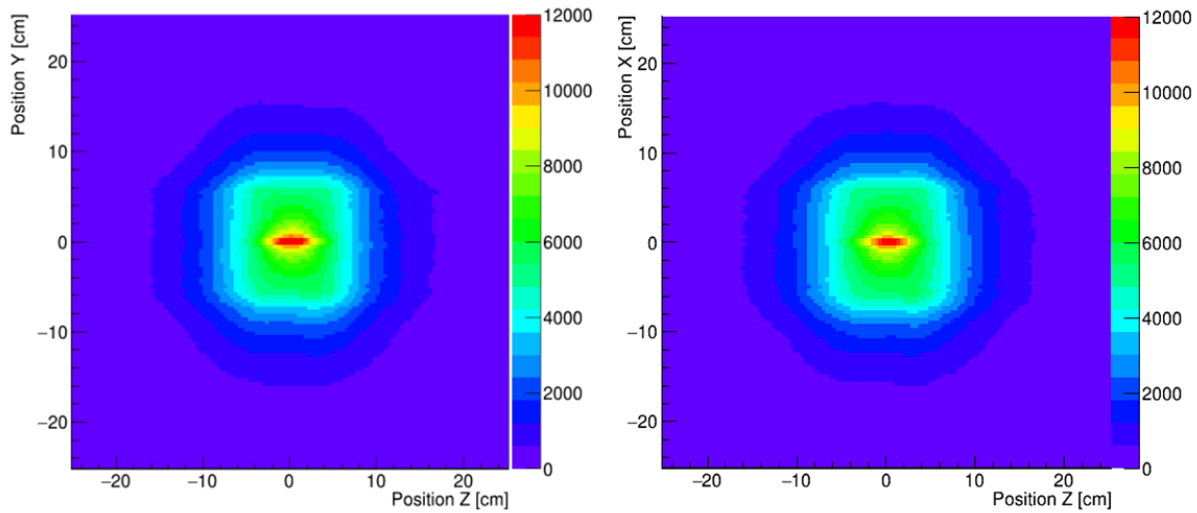ource is located at the geometrical center of the detector. Right: The XZ view shows that the source position along the z-axis is aligned at the geometrical center of the detector.
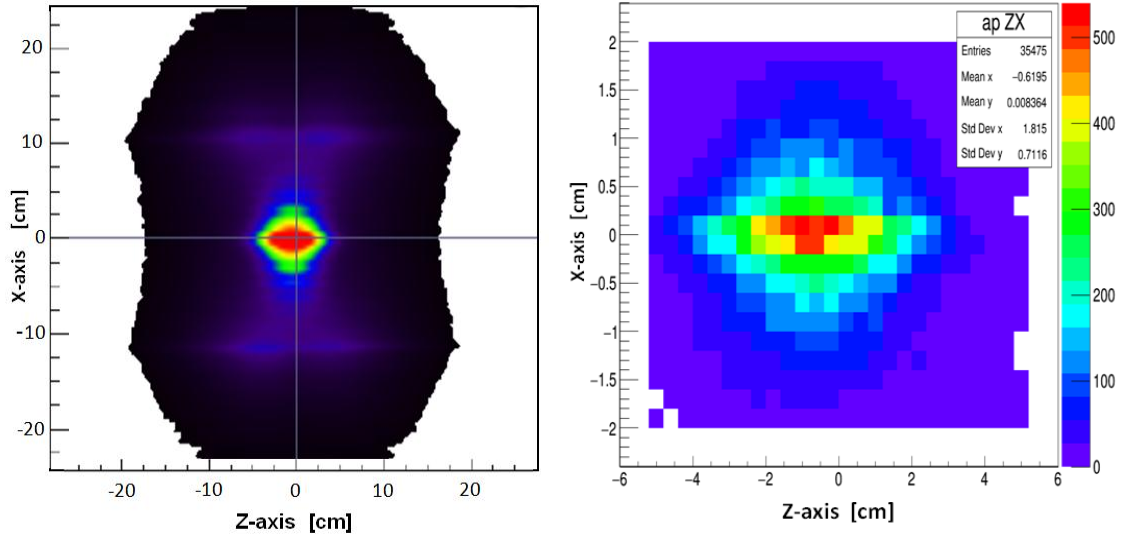
Figure 7.10: Left: Tomographic image of the source region in the measurement with 10 MBq source, obtained using MLEM image reconstruction. An offset of the source is visible along the Z-axis. Right: Zoom of the source region of the XZ view from Figure 7.8 (right). The shift of the source along Z-axis amounts to about -6 mm.

7.6. The identification and reconstruction of 3-gamma annihilation points

In the experiment performed with a large cylindrical chamber, the o-Ps decay location was expected to lie within a porous material target which covers the internal surface of the large annihilation chamber. None of the previous experiments [5,6,4,3] attempted to reconstruct the exact position of the o-Ps decay point. In J-PET, however, due to the relatively high angular resolution and high timing resolution of the detector, the reconstruction of the o-Ps decay into 3γ process is possible using a new trilateration-based reconstruction method described in Section 3.6. The suggested reconstruction method can be also successfully used in the tests of the CP and CPT symmetries with the J-PET detector, allowing for background reduction as well as the determination of o-Ps spin on an event-by-event basis.

7.6.1. The time over threshold (TOT) criterion

The first criterion is based on calibrated time over threshold (TOT) values. We select the hits whose TOT values range is 16 ns < TOT < 36 ns, which correspond to annihilation photons candidates. Similarly, the location of the measured TOT value in the rightmost part of the TOT spectra presented in Figure 7.11 may be used to identify the candidates for interactions of high-energy prompt gamma quanta from the positron source. In order to select candidate events for 3γ annihilations, three-photon interactions with TOT in the above range recorded within a time window of 2.5 ns were required for further analysis.
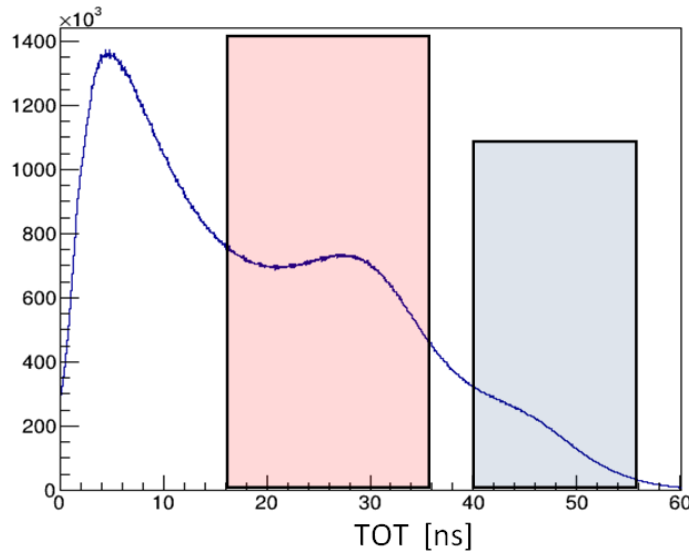
Figure 7.11: Distribution of TOT values for photon interaction recorded in all modules of the J-PET detector in the measurements with the large annihilation chamber. For each interaction, TOT is calculated as a sum of times over threshold at four energy thresholds applied to each of the two photomultiplier electric signals. Two characteristic regions of the distribution used in the analysis are highlighted. The region of TOT used to select annihilation photon candidates is marked with pink color, while the TOT region of de-excitation photons candidates is marked with a blue color.

The second TOT region from Figure 7.11 may be used to select prompt photon candidates, providing start signals for the determination of o-Ps decay time. The actual decay of o-Ps to 3-hit events, comparing to e+e-→3γ direct annihilation observed in case of small aluminum chamber measurements, will involve a lifetime characteristic, the interval of time between an associated de-excitation photon (prompt gamma) and the recording of the annihilation photons. This property can be used for more sophisticated identification of the o-Ps decay. However, requirement of a de-excitation photon registered in coincidence with a 3γ annihilation would significantly reduce the number of accepted events, therefore, in the following analysis prompt photon and, consequently, lifetime information is not used for event selection.

7.6.2. Reconstruction of the annihilation point

In this point, the three annihilation photon candidates are used to reconstruct the 3γ annihilation point using the methods described in Section 3.6. The angular resolution of the annihilation points reconstruction constitutes one of the important factors for control of the linear polarization in the measurements and can be enhanced by the kinematic fit requiring the radial cylindrical coordinate of the annihilation points to be fixed at the radius of the annihilation chamber. The additional time calibration of the

J-PET detector has been achieved and improved in order to enhance the time resolution which has a crucial impact on the performance of trilateration reconstruction for the three-gamma events.

7.6.3. Calculation of the energies of the three photons

Using the J-PET detector, it has not been possible to measure directly the photon energy (Where no direct measurement method of the photon energy is available). However, we are able to reconstruct the momentum of each photon from the o-Ps→3ɣ decay based on the measurements of the photon hit-positions and the o-Ps annihilation point which allows for the determination of the relative angles between the three decay photons with respect to the annihilation point.

The reconstruction of these angles and the use of energy and momentum conservations permit to reconstruct the momenta of all decay photons. In order to analyze the J-PET data, we save the data events where we identified all three photons decay events, then we reconstructed the annihilation points and their normal to the decay planes. Then we tested the asymmetry in the decay planes with respect to the Ps spin direction.

Let us define:

$$\hat{k}_1 = \frac{\vec{r}_{H1} - \vec{r}_{An}}{|\vec{r}_{H1} - \vec{r}_{An}|}, \hat{k}_2 = \frac{\vec{r}_{H2} - \vec{r}_{An}}{|\vec{r}_{H2} - \vec{r}_{An}|}, \hat{k}_3 = \frac{\vec{r}_{H3} - \vec{r}_{An}}{|\vec{r}_{H3} - \vec{r}_{An}|} \tag{7.1}$$

Where:

$\vec{r}_{H1}$, $\vec{r}_{H2}$, $\vec{r}_{H3}$ are the 1st hit position, 2nd hit position and the 3rd hit position respectively.

$\vec{r}_{An}$ the vector of the annihilation point position.

$$d_i = |\vec{r}_{Hi} - \vec{r}_{An}| \text{ for i } = 1,2,3 \tag{7.2}$$

where d_1, d_2, and d_3 are the distance for each hit from the annihilation point as shown in Figure 7.12.

Figure 7.12: Schematic view of the cross section of the J-PET detector showing the case of o-Ps annihilating into 3γ recorded by the scintillators. Red dot located in the center indicates [22]Na radioactive source emitting positron (e+) and de-excitation gamma quantum (orange arrow). The o-Ps is produced in the porous layer on the inner wall of the annihilation chamber (purple band) in which o-Ps formation and decays take place (yellow dot) and decays into three photons which are subsequently recorded in scintillators (marked with blue rectangles).

The angles between the three hits positions with respect to the location of the annihilation point (see Figure 7.13) can be calculated as follows:

$$\theta_{ij} = \text{acos}(\hat{k}_i . \hat{k}_j), \text{for i} \neq \text{j} = 1,2,3 \tag{7.3}$$

Based on the angles between the three hits positions with respect to the annihilation point we can get the values of energy per each decay photon using the following formulas [51]:

$$\left. \begin{aligned} E1 &= -2m_e \left(\cos\theta_{31} + \cos\theta_{12} * \cos\theta_{23}\right)/\left((1 + \cos\theta_{12}) * (1 + \cos\theta_{12}) - \cos\theta_{23} * \cos\theta_{21}\right) \\ E2 &= -2m_e \left(\cos\theta_{23} + \cos\theta_{12} * \cos\theta_{31}\right)/\left((1 + \cos\theta_{12}) * (1 + \cos\theta_{12}) - \cos\theta_{23} * \cos\theta_{31}\right) \\ E3 &= -2m_e \left(1 + \cos\theta_{12}\right)/\left((1 + \cos\theta_{12}) - \cos\theta_{23} * \cos\theta_{31}\right) \end{aligned} \right\} \tag{7.4}$$
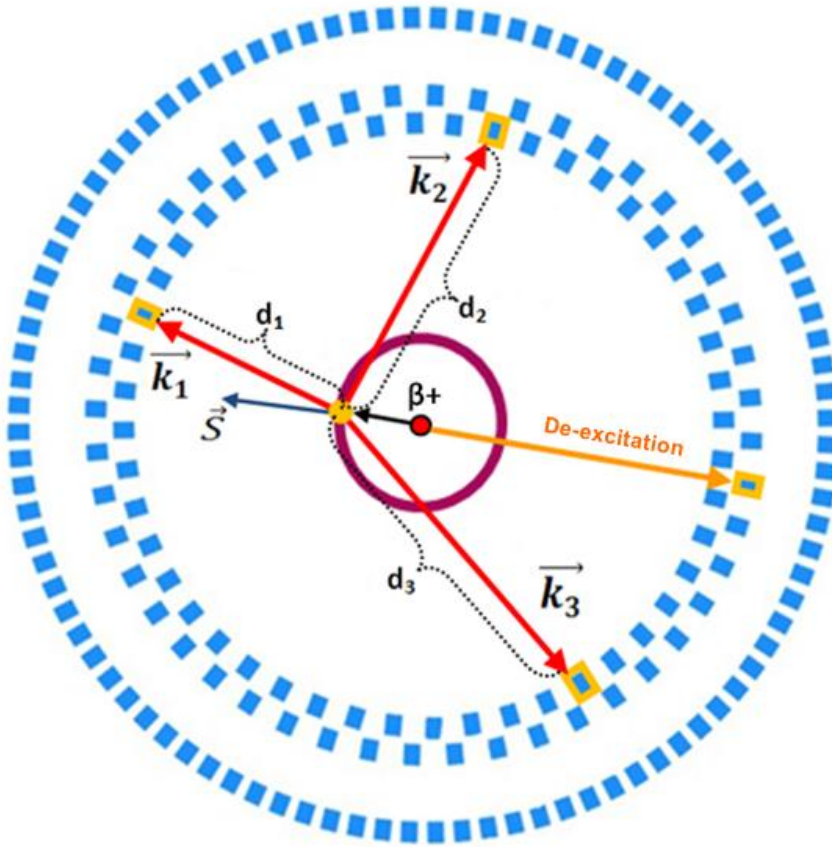
where m_e is the electron mass.
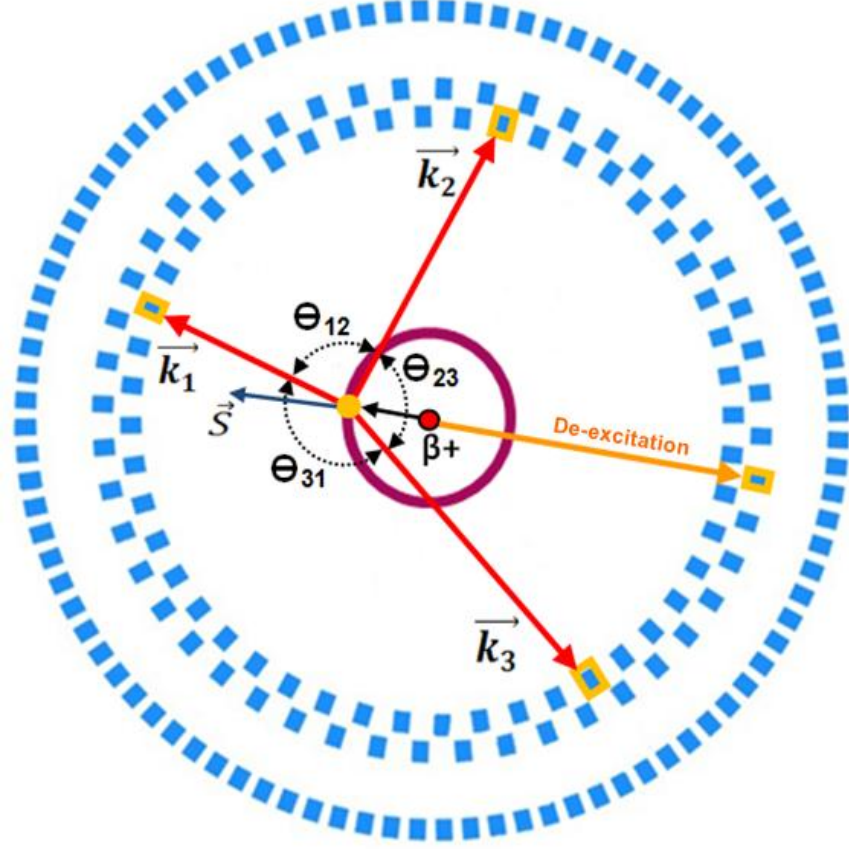
Figure 7.13: Schematic view of the J-PET detector showing the case of o-Ps annihilating into 3γ recorded by the scintillators. Paths travelled by the photons are marked with solid red arrows and yellow arrow indicates the de-excitation photon, $\theta_{12}, \theta_{23},$ and θ_{31} are the angles between vectors indicating hits positions with respect to the annihilation point, ordered so that $\theta_{31} > \theta_{23} > \theta_{12}$.

After the reconstruction of 3 photons energies, events with unphysical kinematical configurations are identified and discarded at this stage.

7.6.4. Determination of the shortest distance between the o-Ps decay plane and the cylindrical target

The Ps spin direction can be estimated by using the trilateration method from the points of 3γ annihilations (see Figure 3.1). And from the same 3γ hits, we can determine the decay plane for each o-Ps annihilation. The shortest distances between the o-Ps decay planes and the center of the J-PET can be calculated by means of determining the projection of the section between the reconstructed o-Ps decay point and the center of the chamber onto the normal of the decay plane (see Figures 7.14 and 7.15). Some decay planes examples are shown in Figure 7.16.
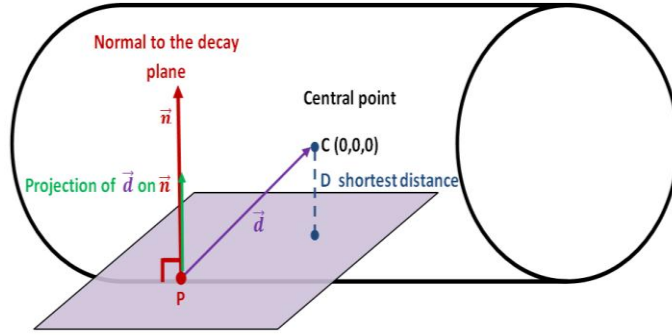
Figure 7.14: Schematic view showing the determination of the shortest distance (D) between the center of J-PET and the o-Ps →3ɣ decay plane, where $\vec{n}$ is normal to the decay plane, D is the projection of $\vec{d}$ on $\vec{n}$.

$$D = \frac{\vec{d} \cdot \vec{n}}{\|\vec{n}\|} = \vec{d} \cdot \hat{n}$$
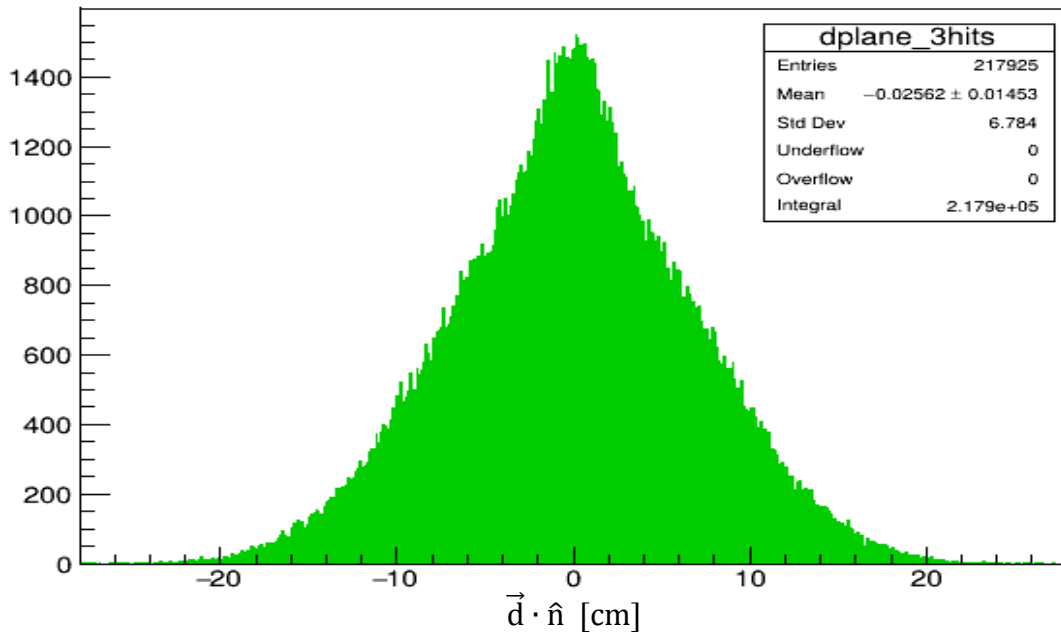
Figure 7.15: Distribution of the shortest distance (D) between the o-Ps decay plane and the geometrical center of the J-PET detector which is required to be less than 27.7 cm. Extreme values allow for the rejection of artificial decay planes obtained for accidental 3-hit coincidences.

In this data analysis, we decided to use shortest distances between the o-Ps annihilation planes and the center of the J-PET detector (presented in Figure 7.15) in the event's selection to reject the background which comes from the artificial annihilation points reconstructed in case of for example the accidental coincidences where the annihilation points are located outside the wall of the decay chamber or those which are located at the edges of the chamber. Figure 7.16 depicts two cases of events which can be distinguished by this value. As the maximum distance of the geometrically allowed annihilations happening at the farthest point of the chamber surface from the center is 27.7 cm, events with D > 27.7 cm are rejected.
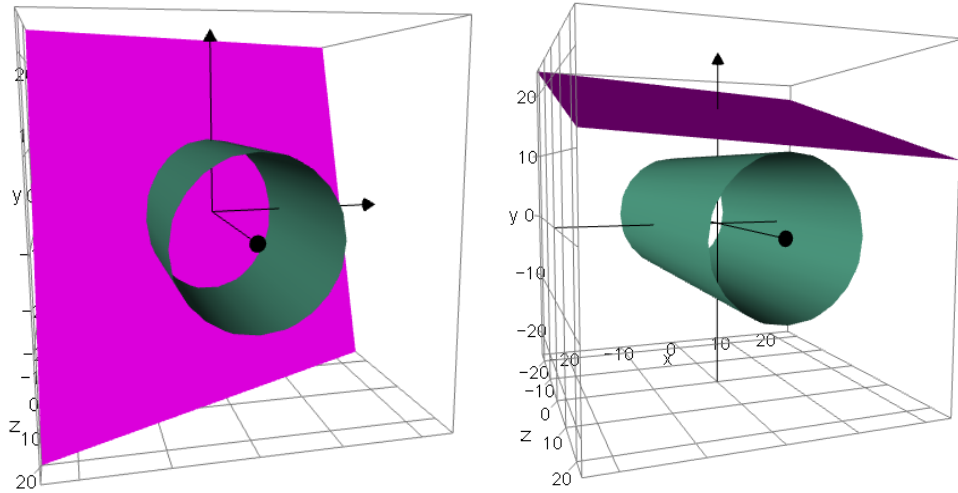
Figure 7.16: Visualization of two different exemplary orientations of the recorded decay plane (violet) with respect to the cylindrical decay chamber (green). Left: In the case of a genuine o-Ps→3γ decay occurring in the positronium production medium located in the cylinder wall, the point of closest approach of the plane to the geometrical center of the detector cannot be larger than the distance of the furthest allowed annihilation point on the chamber surface. Right: In the case of a decay plane resulting from an accidental 3γ coincidence, the decay plane may be distant from the center [**101**].

This criterion does not depend on the resolution of the o-Ps→3γ reconstruction. While in principle the distance between the reconstructed o-Ps→3γ annihilation point and the detector center could be used to identify artificial 3γ coincidences, such criterion would be affected by the resolution of the annihilation point reconstruction. Therefore, the criterion described above was chosen to avoid signal events rejected due to finite annihilation point resolution.

### 7.6.5. The shortest distance between the LORs and the reconstructed annihilation points

The major sources of the background for o-Ps $\rightarrow$ 3ɣ events at this stage are the 2ɣ annihilations which may happen in the aluminum holder of the source at the central part of the cylindrical annihilation chamber inside the J-PET detector and one scattering photon or random three photons in coincidence.

In order to identify events containing a back-to-back 2ɣ annihilation, we have considered all the possible choices of possible pairs of hits out of three in an event candidate, then three hypothetical lines of response (LORs) (see Section 4.4) have been reconstructed (LOR for each pair of every 2-hits out of 3-hits). After that, for every three such possibilities, one hypothetical 2ɣ annihilation point has been reconstructed per each LOR. A detailed description can be found in Figure 7.17 and Figure 7.18. Eventually, we had 3 possible distances between the hypothetical 2ɣ annihilation points and the reconstructed 3ɣ annihilation point for each of the reconstructed o-Ps decay points, out of each, we selected the minimal, maximum and the sum of the three distances referred to as total distance.

The applied criterion includes the shortest distance (d_{min}), longest distance (d_{max}) and total distance (d_{total}) between the 2ɣ annihilation point located on the LOR and the 3ɣ annihilation point obtained from trilateration based on all three hits. This criterion remove most of the possible artificial 3-hit events.
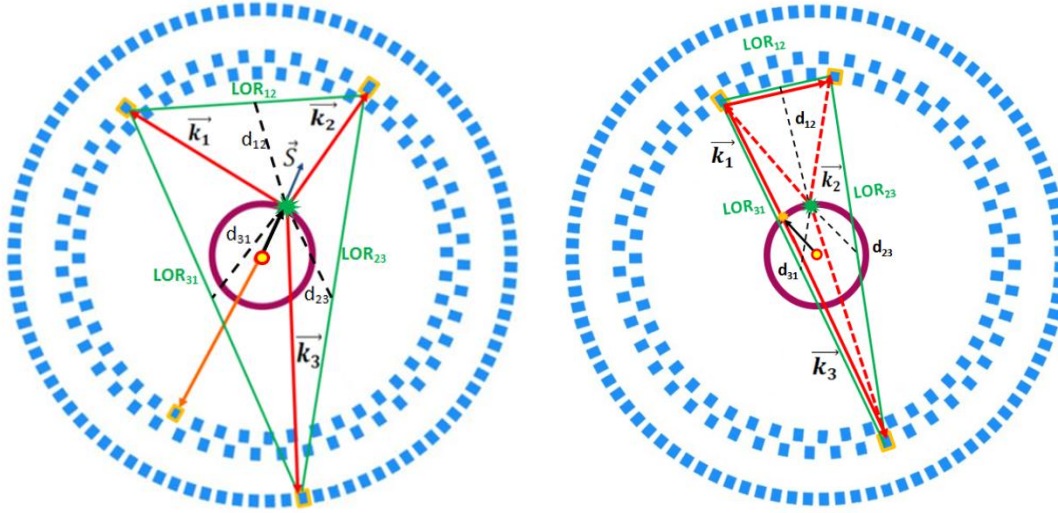
Figure 7.17: Schematic view of the J-PET detector showing the distances (d_{min}) marked with dashed black lines between the hypothetical 2 gamma annihilation point on each LOR (green lines) and the 3ɣ annihilation point (green star) on the wall of the large annihilation chamber. Left: Genuine o-Ps annihilation into 3 photons (marked with solid red lines). Right: e+e- annihilation into 2ɣ back-to-back and one secondary photon scattering (solid red lines). Dashed red lines indicate artificially identified 3ɣ annihilation photons.

The true 3-hit events from the annihilation chamber can be distinguished from artificial 3-hit events shown in Figure 7.19, which are mostly combinations of 2ɣ events with an accidental or scattered photon, or the coincidence of three random photons via the relation between the shortest distance versus the total distance which shows a distinctive structure corresponding to the target region and the radioactive source region. The explanation, how particular kinds of events can be identified by specific values of d_{min} and d_{total}, is as follows:

In case the event contains a pair of back-to-back photons, one of the considered LOR-s would be true, resulting in one of the distances being very small and close to zero like d_{31} in the case presented in the right panel of Figure 7.17, which means the 2ɣ hypothetical annihilation point (indicated as a yellow star) which corresponds to the LOR$_{31}$ could be true. In this case, one of the hypotheses will be true about the LOR location, so this distance has to be small. On the other hand, in the case of scattering, the 2ɣ annihilation point reconstructed on the LOR which represents the hypothetical annihilation point location would usually be as far from the chamber as the location of one of the layers of the J-PET detector. Therefore, one of the distances should be rather large as you can see in the case of d_{12} in Figure 7.17.

The 2nd criterion based on the total of the three distances d_{total}, which would be sensitive to large distance from scattering as shown in Figure 7.18. Also we considered the cut on the maximum distance d_{max} (where d_{max} <77.3 cm), this cut was used as an additional criterion, in order to remove any events which include unphysical values of the distances with respect to the geometrical size of the J-PET.
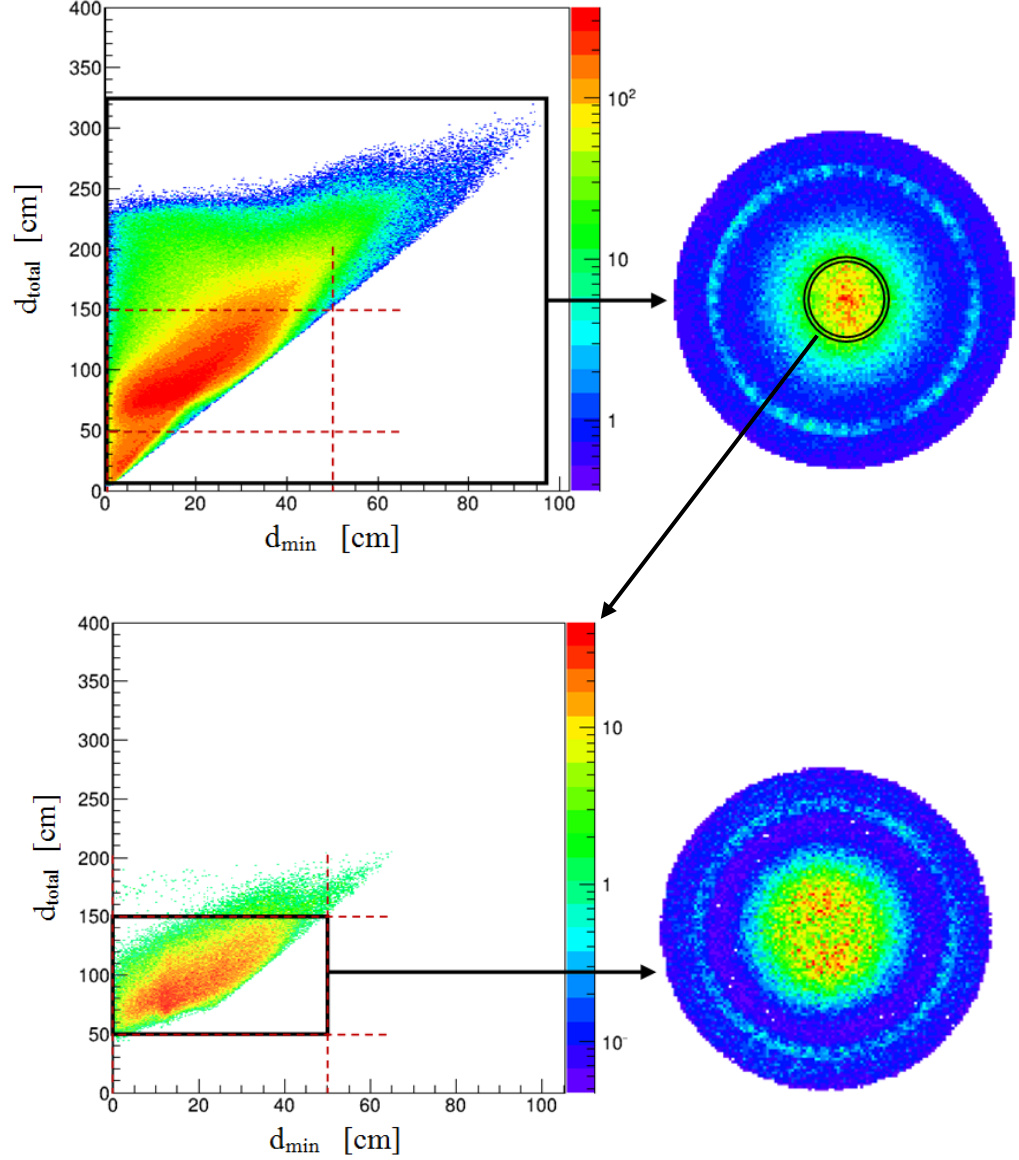
Figure 7.18: The shortest distances (d_{min}) vs. the total distances (d_{total}) between the o-Ps→3ɣ annihilation point and 2ɣ annihilation points on all possible hypothetical LORs. Top-Left: The distribution of d_{min} vs. d_{total} for all the events at this stage of the data analysis. Top-Right: The XY distribution of the decay points with the same conditions for the same set of events. The value of the cuts at d_{min} and d_{total} was selected by looking at the subset of this events selected from the ring marked in the top-right figure, where the largest contribution of 3ɣ events is expected. For these events only we obtained the distribution shown in the bottom-right figure and after applying the cuts shows in the bottom-left Figure, where the small black rectangle indicates the selected ranges which were applied in the event selection which is between (0-50) cm for d_{min} and (50-150) cm for the d_{total}.
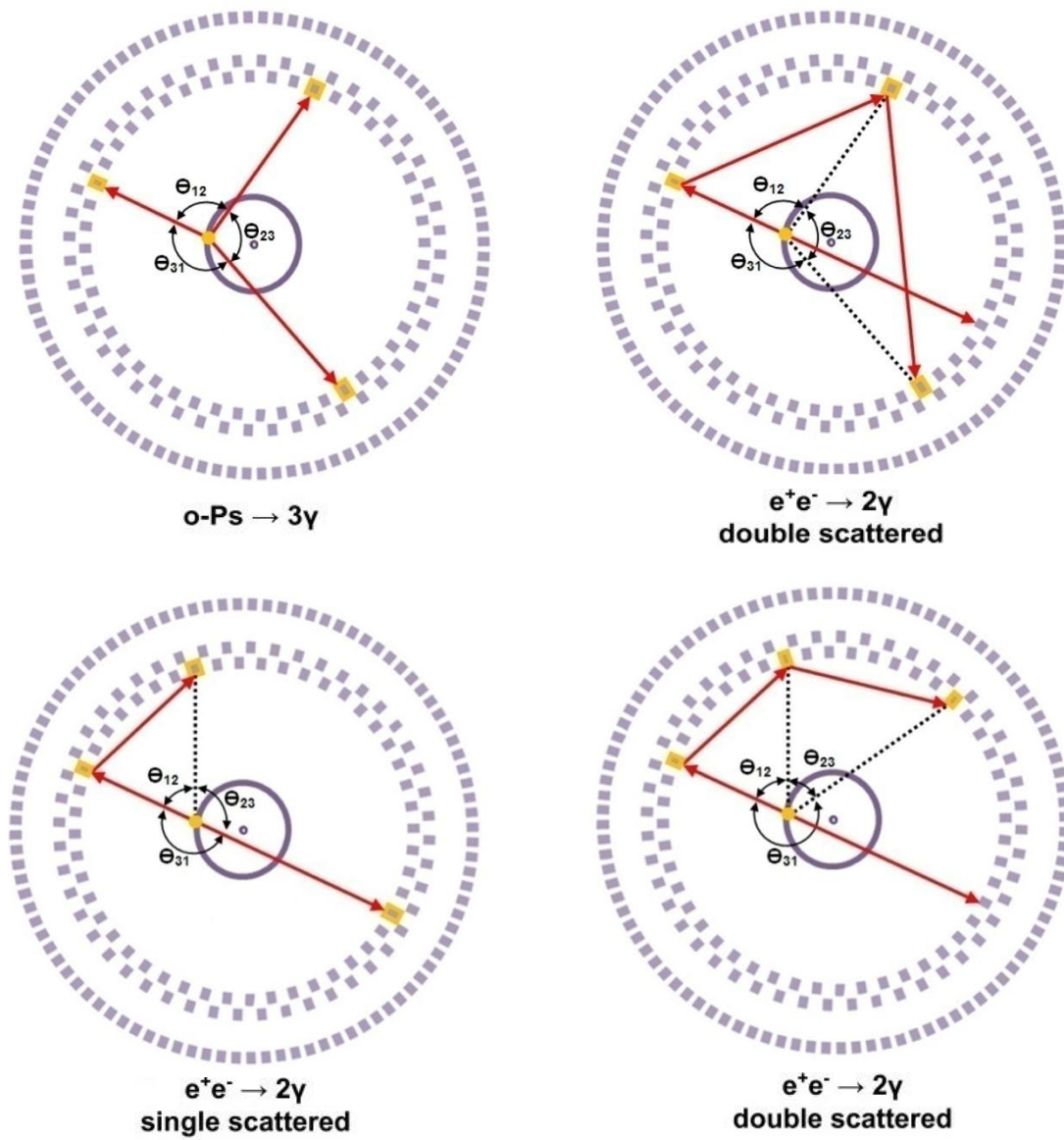
Figure 7.19: The pictorial illustration of the four possible responses of the J-PET detector to three gamma quanta annihilation o-Ps→3γ (top-left) and annihilation of e+e− →2γ. Circularly arranged purple rectangles represent scintillator strips, purple and orange colors indicate strips where the gamma quanta were registered. The solid red arrows represent gamma quanta occurring in the events, while dashed black lines indicate the artificially identified primary photons. Θ_{ij} are the ordered angles between registered gammas.

7.6.6. The study of the angular configuration of the events

The analysis of the obtained J-PET experimental data revealed that the main source of the background for the o-Ps annihilation studies is composed by the contribution of different processes like pick-off annihilations and ortho-para spin conversion due to the spin-orbit interaction or due to the exchange of electron [7], which leads to 2γ back to back annihilations, which may scatter and mimic the o-Ps $\rightarrow 3\gamma$ decay. The contribution from these processes depends on the used target material [102].

The background can be suppressed by considering the distribution of the sum versus the difference of the two smallest angles between the momenta of the reconstructed decay photons. Background events will correspond to points at the broadening line at 180°. It should be noted that two kinds of angles have been calculated, the first kind of angles (2-D angles) were calculated with respect to the geometrical center of the detector as shown in Figures 7.20 and 7.22, where the 2γ band is visible. The possible selection criteria can be applied to the ordered values of the opening angles ($\Theta_{12} < \Theta_{23} < \Theta_{13}$) between registered photons.

We cannot cut on the 2D angles because the o-Ps region partially overlaps with the 2γ band, so such a cut would reject a lot of signals. We expected that the o-Ps (3-hit) events in the rightmost part of the above figures [103], where this was confirmed with simulations.

The second kind of angles (3-D angles) were measured with respect to the position of the reconstructed o-Ps annihilation points as you can see in Figures 7.21. In the case of o-Ps $\rightarrow 3\gamma$ decay and due to the conservation of the momentum, the two smallest angles fulfill: $\Theta_{12} + \Theta_{23} > 180^o$, which means that the events corresponding to the o-Ps $\rightarrow 3\gamma$ decay lie in the right part of the triangle, as shown in Figure 7.21.
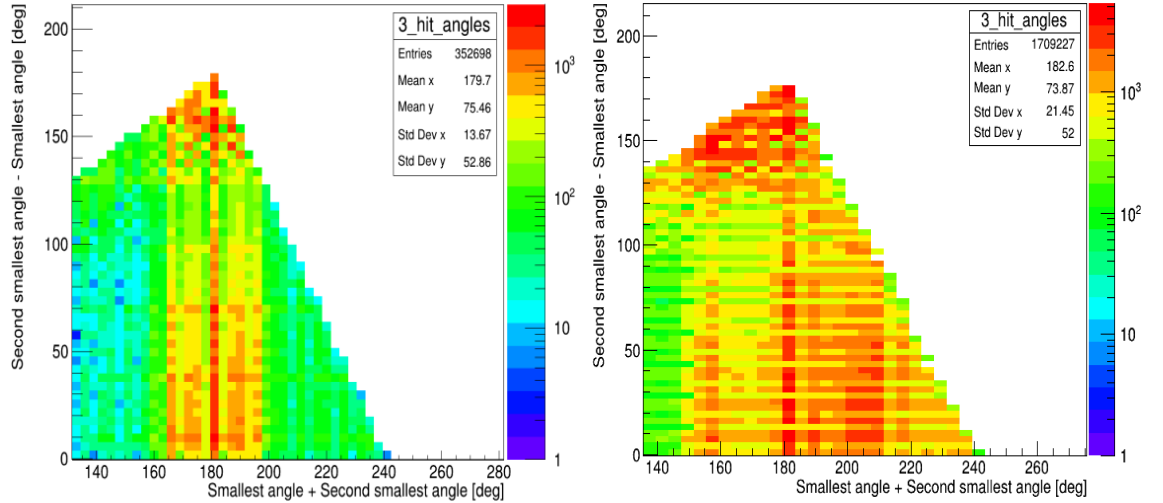
Figure 7.20: The sum of the 1st and 2nd smallest angles vs. the difference between them measured with respect to the center of J-PET detector. Left: The case of small Al annihilation chamber. Right: The case of large annihilation chamber with a layer of porous material. The broadening of the band around 180° is caused by calculating the angles between 2-hit with respect to the center of the detector as explained in Section 7.5.1.

Before use the scatter test criterion, we tried to use another criterion, by simply cut the small angles between hits, where the minimum angular distance in the XY-plane between two strips which registered ɣ quanta was set to 20 degrees. This condition allowed for the reduction of scattered photons from the neighboring strips in the J-PET detector, see Figure 7.21 (right).

One can consider this cut to remove the scattering events but it is not optimal, because while this sharp cut remove all the events at the top part of the triangle were most of the scattering expected to be located, there might be some scatterings in the other populated regions of the distribution. Instead of this cut a more sophisticated criterion was used, as described in Section 7.6.7. In the result of the scatter test criterion, one can see that this criterion by looking at the properties of the events not only the angles. The scatter test remove everything from the top part of the triangle but also identified a lot of events as a scatterings in the rest of the regions (as shown in the Figure 7.24).
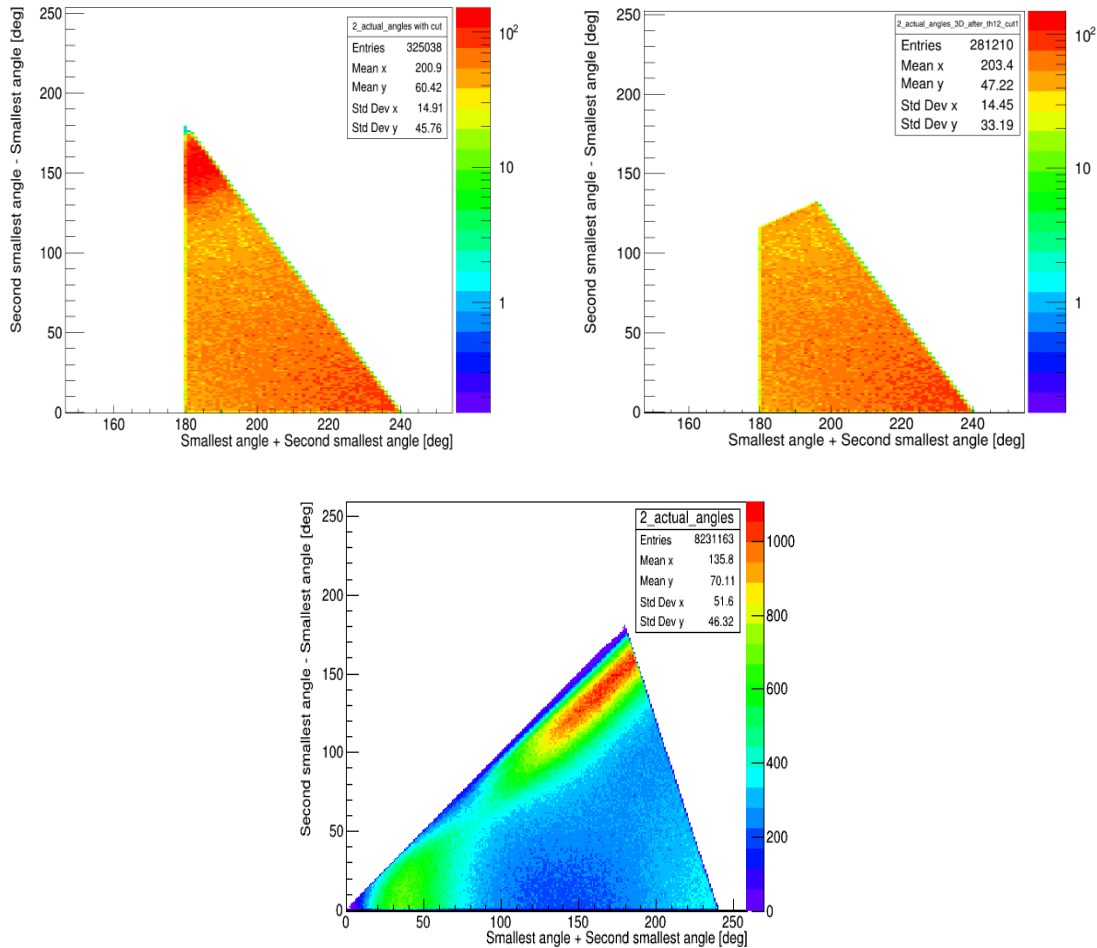
Figure 7.21: Left: The sum of the 1st and 2nd smallest angles versus the difference between them which was measured with respect to the o-Ps annihilation points in the case of large annihilation chamber with a layer of porous material. The part of the sum of the smallest angles which less than 180º has been removed by the criterion of the allowed kinematics configuration. Right: The distribution after cut of the smallest angle. Bottom: The distribution before applying the pre-selection cuts.
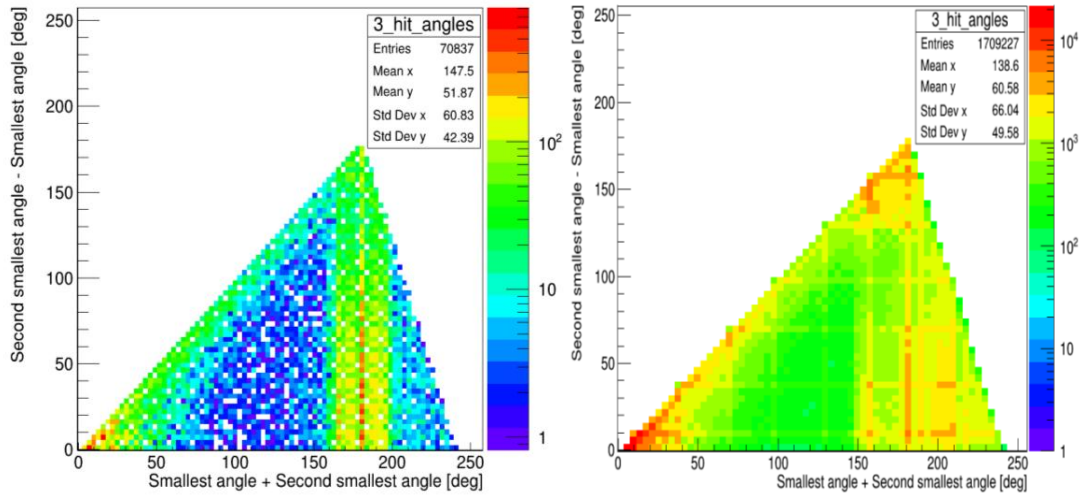
Figure 7.22: Left: The distribution of the difference versus the sum of the two smallest angles measured with respect to the geometrical center of the detector in the case of a small annihilation chamber experiment. With such a choice of variables on the x, y axes, events from two gamma photons annihilations, which contain two photons with opposite momenta, are congregated in a vertical band symmetrically around 180°. Right: The distribution of the difference versus the sum of the two smallest angles with respect to the geometrical center of the detector for the case of a large chamber experiment. With such a choice of variables on the x, y axes, events from two gamma photons annihilations, which contain two photons with opposite momenta, are congregated in a vertical band symmetrically around 180°. This band is wider comparing to the band in the case of the small chamber, also it's unsymmetrical, where there are more counts on the right of 180° because of o-Ps which is overlapping in this region.

7.6.7. The scatter test

The main source of the background in the case of 3γ annihilations comes from single scattering or double scattering of one of the 2 gamma (back to back) photons due to the secondary interactions of primary photons Compton-scattered in the neighboring scintillators strips as presented in Figure 7.19. The registration of such scattered photons mostly happens in the detection modules neighboring to that where the primary photon interacted and was registered, therefore, events were rejected if they contained a pair of gamma interactions recorded in modules whose azimuthal coordinates were equal or closer than 7.5 degrees. This criterion removes all the possible scatterings in modules next to each other in a single layer of J-PET detector as well in pairs neighboring between the layers.

The secondary interactions of primary photons Compton-scattered in the scintillators strips, are registered mostly in the detection modules neighboring those ones where the primary photons are recorded. The best way to remove those events is to reject the events if they contained a pair of neighboring modules regardless if they belong to the same detector layer or two neighboring layers. This criterion removes the most Compton scatterings in modules next to each other. This selection criterion which is intending to remove the scattered photons was based on testing a hypothesis that the time difference between the registration of any 2-hit out of 3-hit in an event

corresponding to a time of flight of a hit photon between the reconstructed locations of the two subsequent interactions, which was performed via calculation of the parameter: $\delta_{ij} = |d_{ij} - c*dt_{ij}|$

where: $dt_{ij} = |t_i - t_j|$

$d_{ij} = |r_i - r_j|$

then:

$\delta_{min} = \min_{i \neq j = 1, 2, 3} \{ \delta_{ij} \}$

where t_i and r_i denote the recording time and position vector of i-th photon interaction in an event respectively, and c is the velocity of light. A value of δ_{ij} close to zero corresponds to a pair of hits created by subsequent Compton scatterings of the same photon in different detection modules. Distribution of δ_{min}, defined as the smallest (in terms of absolute value) of three possible δ_{12}, δ_{23} and δ_{31} values for each event is displayed in Figure 7.23.

To reduce the contamination of the 3-hit event sample with secondary scatterings of the primary photons, a three-hit event was rejected if its δ_{min} was less than 17 cm as indicated in Figure 7.23.
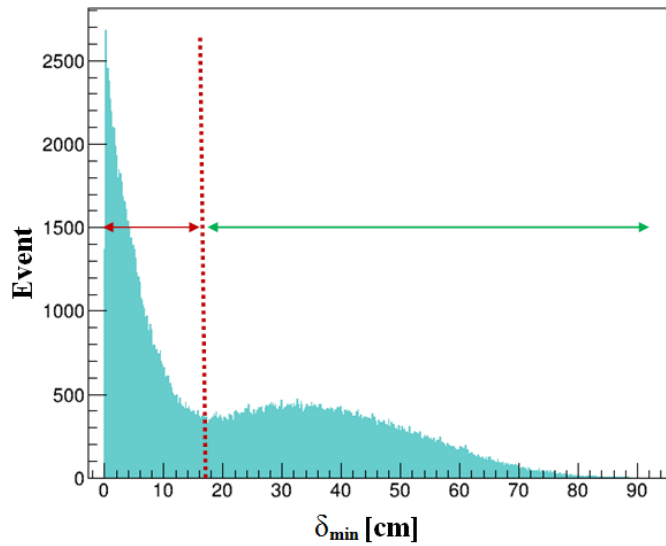
Figure 7.23: Distribution of the minimal discrepancy between inter-hit distance and hypothetical TOF times the velocity of light among all hit pairs in a 3-hit event. The events with $\delta_{min} > 17$ cm are considered in further analysis as marked with the dashed line and green arrow.

To remove the remaining scattering events, another selection criterion was additionally used which is based on testing a hypothesis that the time difference between recorded hits corresponds to a time of flight of a photon between the two reconstructed interaction positions. This hypothesis was tested for all possible choices of 2-hit pairs out of 3-hit in an event. The method includes the calculation of the discrepancies between inter-hit distance and hypothetical TOF for all hit pairs in a 3-hit event.

Figure 7.24, (right) shows the effect of the applied scatter test on the relation between the sum of the smallest angles versus the difference between them in the case of large annihilation chamber, comparing with the same relation in the case of large chamber before apply the scattering cuts which are shown in Figure 7.24 (left).
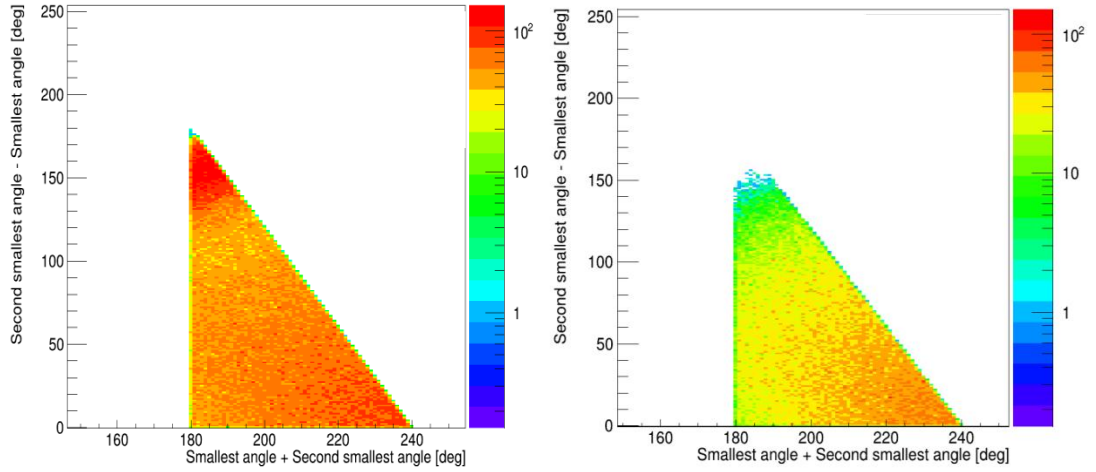
Figure 7.24: Left: The sum of the 1st and 2nd smallest angles versus the difference between them in the case of a large chamber with a layer of porous material before application of the scatter test. Right: The sum of the 1st and 2nd smallest angles versus the difference between them measured with respect to the o-Ps annihilation points in the case of large annihilation chamber with a layer of porous material after application of the scatter test (17 cm cut).

7.7. The study of the distribution of the o-Ps annihilation points

Reconstruction of annihilation points for a clean sample of o-Ps→3gamma annihilations at the walls of the target chamber should reproduce the chamber cylinder. To verify this, the transverse images of the chamber were obtained with the annihilation points reconstructed using the trilateration method presented in Section 3.5. In order to evaluate the reconstruction of annihilations at the chamber walls, the transverse view images of the annihilation points are shown separately for the complete projection along the z-axis of the J-PET detector as well as for the region of |z| > 5 cm, after excluding the annihilations in the source holder rather than in the chamber walls (as previously demonstrated with the 2-gamma images).

Figure 7.25 shows the image before rejection of the secondary scattering events, where no structure of the chamber is discernible due to the amount of background events clustered in the central region.

After application of the scatter test, a ring structure becomes visible (Figure 7.26, left), corresponding to the chamber shape smeared by the resolution of the annihilation points reconstruction (of the order of a few centimeters). This resolution is largely dependent on the quality of time calibration of the detector, thus after application of the refined time calibration described in Section 6.2.2, the reconstructed annihilation points of 3ɣ annihilations are grouped and become more dense and closer around the geometrical limits of the large annihilation chamber as demonstrated in Figure 7.26, right.
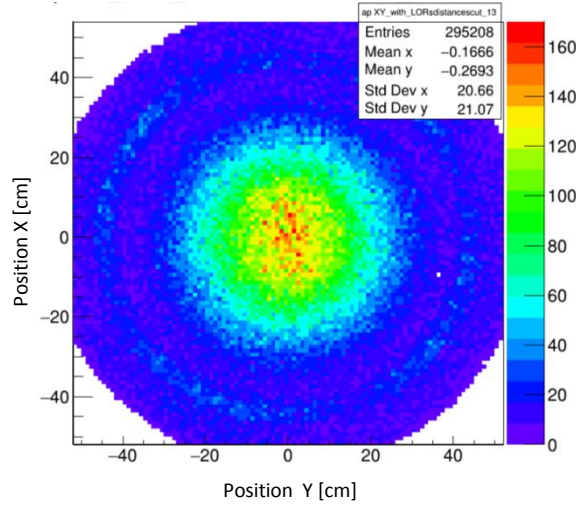
Figure 7.25: The distribution of the reconstructed o-Ps→3ɣ annihilation points (the transverse view of the large annihilation chamber with 10 MBq source without time calibration nor a scatter test cut).
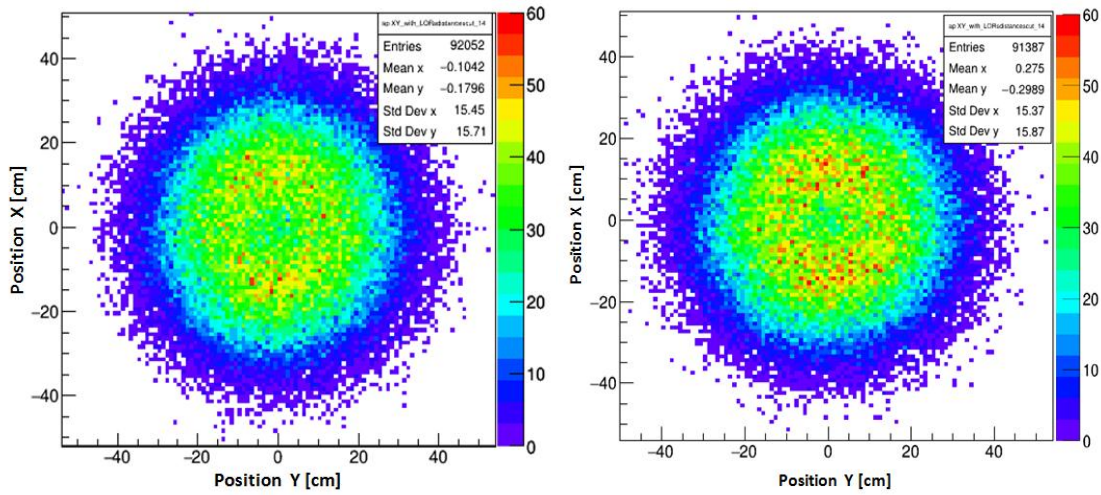
Figure 7.26: The distribution of the reconstructed annihilation points of target cylinder obtained using Ps→3ɣ annihilations (the transverse view of the large annihilation chamber with 10 MBq source) after application of the scatter test cut before (left) and after (right) the refined time calibration described in Section 6.2.2.

The annihilation points were reconstructed using the trilateration method presented in Section 3.5. In order to evaluate the reconstruction of annihilations at the chamber walls, the transverse view images of the annihilation points are shown for the region of $|z| > 5$ cm, after excluding the annihilations in the source holder rather than in the chamber walls as demonstrated with the 2-gamma images. Figure 7.27 shows the transverse plane location of 3-gamma annihilation points after excluding the annihilation points with $|z| \leq 5$ cm. The geometrical acceptance of the J-PET detector is reduced for annihilations taking place closer to its edges.

As a final step of event selection for the study of the angular correlation between o-Ps spin and the normal to the o-Ps decay plane which is discussed in Section 8.3, a new selection criterion was applied by selecting only the annihilation points located in the range of 4-20 cm on the transverse radius of the large annihilation chamber, with the radius of 12 cm.

This cut was important to remove the events which were produced close to the central region of the annihilation chamber which most likely are due to the direct annihilation on the holder of the source. Also, for genuine o-Ps→3γ events reconstructed close to the source, the o-Ps spin resolution would be worse because of the smaller distance between the source and the annihilation points.
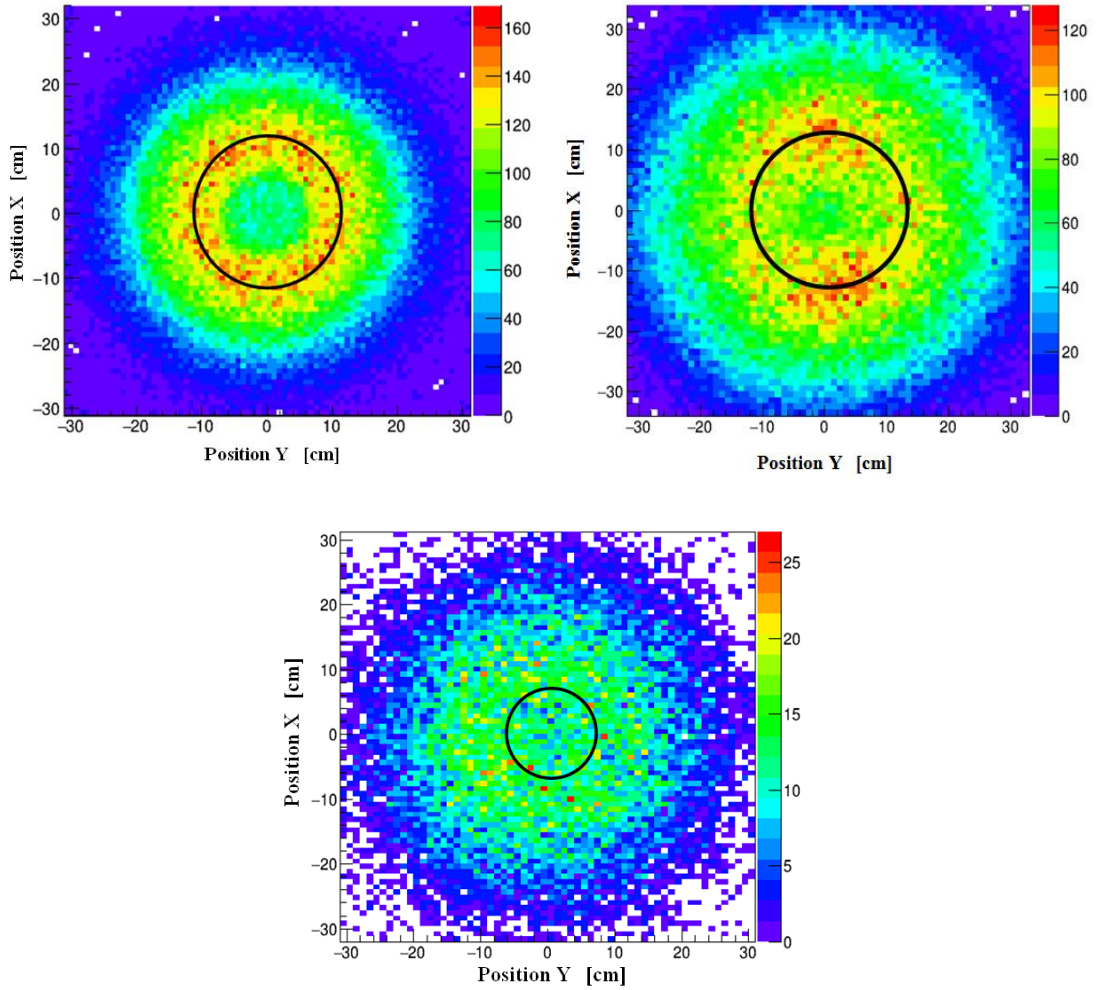
Figure 7.27: The distribution of the reconstructed annihilation points of target cylinder obtained using o-Ps→3γ annihilations. (Top-left) The transverse view of the large annihilation chamber with 1 MBq source. (Top-right) The transverse view of the large annihilation chamber with 10 MBq source. (Bottom) The transverse view of the small annihilation chamber with 10 MBq source. The black circle indicates the wall location of the large cylindrical decay chamber. Also z=±5 cm has been excluded to reduce the effect of annihilations taking place in the β⁺ source setup.

8. Determination of the CPT violation sensitive angular correlation

8.1. The CPT symmetry test by J-PET

The test measurement of CPT violating effects in the leptonic system constituted by positronium would be a signature of physics beyond the Standard Model. The positronium atom offers the opportunity to test the CP and CPT symmetry in a charged lepton system. So far, the recent measurements of CPT-violating parameter C_{CPT} are consistent with zero at 3.1×10^{-3} precision. The ultimate goal of J-PET is to improve this precision by at least one order of magnitude.

The result of the best experiment to date searching for CPT symmetry violation in positronium decays is consistent with zero, with a statistical uncertainty of about 3.1×10^{-3} [5]. The J-PET detector allows determining those values with an improved precision, thanks to the unique time and angular resolution combined with a high geometrical acceptance of the detector. This experiment has been performed using silica R60G as a porous material target which allows collecting the required 3-hit events with a good statistics. As discussed in section 3.1 the positrons from the e+ decay of ^{22}Na are a linearly spin polarized along their velocity vector due to the violation of parity, thus knowing the direction of e+ velocity defines the spin direction of the positron with an average uncertainty which is changing with the mean energy of the emitted positrons [7]. The spin of the o-Ps has an average uncertainty depending also on the amount of linear polarization loss through the thermalization process of the positron [104], and on the fact that only 2/3 of the formed positronium atoms possess the same spin of the positrons [6].

The most general form of the angular correlation operator studied in this work is $\vec{S} \cdot (\vec{k}_1 \times \vec{k}_2)$, where $\hat{S}$ is the vector of the positronium spin, while $\vec{k}_1$ and $\vec{k}_2$ are the vectors of the directions of the highest and second-highest energy photons from the three-photon decay of ortho-positronium.

This operator is even under the charge conjugation (C). The above product is also symmetric under the parity transformation as shown in Figure 8.1 left, where the spin $\vec{S}$ of polarized o-Ps, and the normal to the decay plane $\vec{N}$ does not reverse and all the annihilated photons vectors are reverse. But it is odd under the transformation of time reversal (T) as shown in Figure 8.1 right, where the o-Ps spin $\vec{S}$ is reversed and k_1 and k_2 are the momenta of the two most energetic photons emitted by o-Ps decay into three-photons. The three photons must be co-planar, and the quantity $(\vec{k}_1 \times \vec{k}_2)$ unambiguously defines the decay plane. So $\vec{S} \cdot (\vec{k}_1 \times \vec{k}_2)$ is the correlation between the spin direction of the initial o-Ps atom and the decay plane. In order not to violate the time-reversal symmetry, there should be no preference for the decay plane either

parallel or antiparallel. Under the time reversal, the o-Ps spin and the momenta of the photons all reverse, and $(\vec{k}_1 \times \vec{k}_2)$ does not reverse as shown in Figure 8.1, so it is T-odd and since the operator is P-symmetric and C-symmetric as mentioned above, thus it is CPT odd.
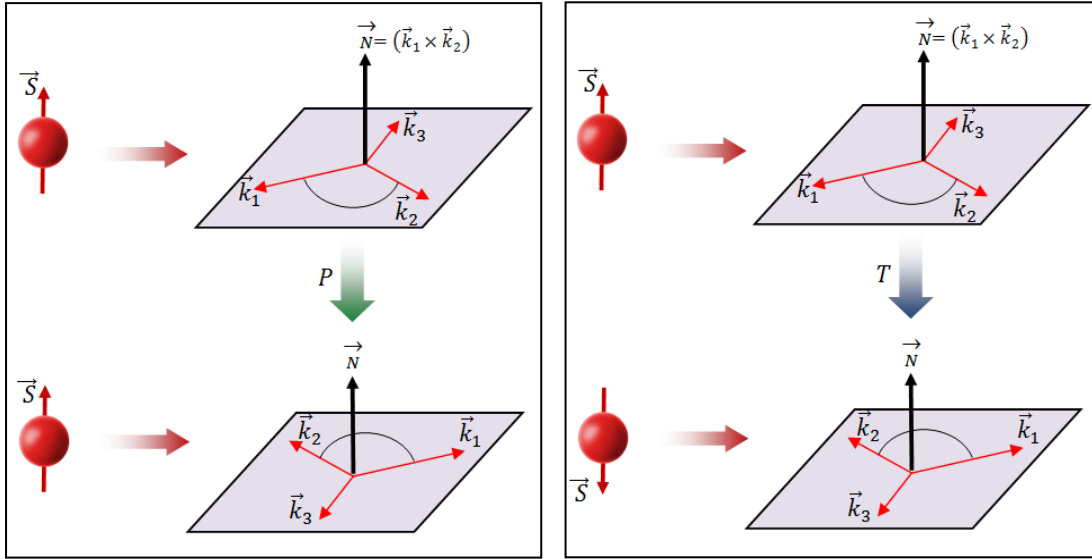
Figure 8.1: Definition of the geometry and of the quantities used for the experimental tests of CPT symmetry in the positronium. The vectors $\vec{k}_1$ and $\vec{k}_2$ are the momenta of the first and second highest energy photons, respectively. The $\vec{S}$ vector indicates the spin of the o-Ps atom. Left: In the case of parity transformation (P), the studied operator $\vec{S} \cdot (\vec{k}_1 \times \vec{k}_2)$ is P-symmetric, where o-Ps spin $\vec{S}$ and the normal to the decay plane $\vec{N}$ do not reverse and the momenta of the photons are reversed. Right: In the case of time reversal transformation (T), the operator is T-odd, where the spin $\vec{S}$ and the momenta of the photons all reverse, and the normal to the decay plane $\vec{N}$ does not reverse. As positronium and the final state photons are all C-symmetric, the total $\vec{S} \cdot (\vec{k}_1 \times \vec{k}_2)$ operator is thus CPT-odd.

So far, the results on the discrete symmetries tests including CP and CPT in the positronium system show that there is no violation signal. The most precise measurements studied the angular correlation operators in the o-Ps decays into three photons and determined mean values of the odd final state operators under the conjugations of CP and CPT, without indicating symmetry violation at the level of precision of 3.1×10^{-3} [3,5].

8.2. Observable of CPT symmetry test

In this study, we focus on a special case of the CPT-violation sensitive operator defined as:

$$O_{CPT} = \hat{S} \cdot (\vec{k}_1 \times \vec{k}_2)/|\vec{k}_1 \times \vec{k}_2| = \cos \phi \tag{8.1}$$

Using the J-PET detector the CPT symmetry may be tested by searching for the possible non-zero expectation value of $\vec{S} \cdot (\vec{k}_1 \times \vec{k}_2)/|\vec{k}_1 \times \vec{k}_2|$ operator, which is the angular correlation between the spin of the o-Ps atom and the normal to the decay plane in o-Ps→3γ. The non-zero expectation value of the tested CPT-odd operator would imply a violation of the CPT symmetry. The non-zero expectation value indicates a difference in the probability of the events between cases when the normal to the decay plane is pointing up and down with respect to the spin vector $\vec{S}$ of the o-Ps atom before its decay. It means that the CPT-symmetry violation would manifest itself as asymmetry in the orientation of the normal to the decay plane which is defined as $\vec{k}_1 \times \vec{k}_2$ with respect to the direction of initial spin of the o-Ps atom [**7**].

8.3. Determination of the CPT-odd angular correlations in the ortho-positronium decay

The aim of this study was to determine the expectation value of the angular correlation $\vec{S} \cdot (\vec{k}_1 \times \vec{k}_2)$ operator. The direction of the o-Ps spin $\hat{S}$ was estimated via the linear polarization of the positron as discussed in Section 3.1, therefore, to estimate the direction of the o-Ps spin we take the direction of the emission of the positron estimated as a vector from the source location to the annihilation point.

$$\hat{S} = \frac{\vec{S}}{|\vec{S}|} = \frac{\vec{r}_{An}}{|\vec{r}_{An}|} \tag{8.2}$$

where $\vec{S}$ is the spin vector of the ortho-positronium assumed to be the same as that of the spin of the positron. Its direction is estimated by subtracting the coordinates of the decay point from the coordinates of the center, where the β^+ source is located.

The values of the O_{CPT} operator (8.1) for the CPT symmetry test have been calculated using the above positronium spin estimation and photon's momenta obtained as in equation (7.1), and the results are shown in Figures 8.2 and 8.3. The Figures show the distributions of $\cos \phi$ defined in equation (8.1) for the measurements with a large annihilation chamber using 1 MBq source and 10 MBq source respectively, while Figure 8.4 shows the combined results of both measurements.

The mean values obtained from these two measurements are:
$$\langle O_{CPT}^{(1)} \rangle = (-0.0068 \pm 7.2) \times 10^{-4}$$
for the measurement with the large annihilation chamber using 1 MBq source
and
$$\langle O_{CPT}^{(2)} \rangle = (-7.3 \pm 4.3) \times 10^{-4}$$
for the measurement with the large annihilation chamber using 10 MBq source.

Figure 8.2: The distribution of the $\hat{S} \cdot (\vec{k}_1 \times \vec{k}_2)/|\vec{k}_1 \times \vec{k}_2|$ operator, which is the observable of the CPT symmetry test for the measurement with the large annihilation chamber using 1 MBq source.

Figure 8.3: The distribution of the $\hat{S} \cdot (\vec{k}_1 \times \vec{k}_2)/|\vec{k}_1 \times \vec{k}_2|$ operator, which is the observable of the CPT symmetry test for the measurements with the large annihilation chamber using 10 MBq source.
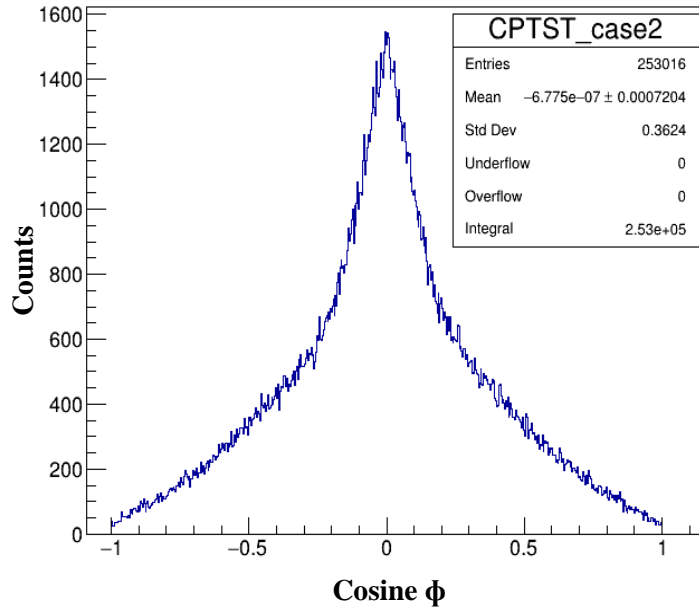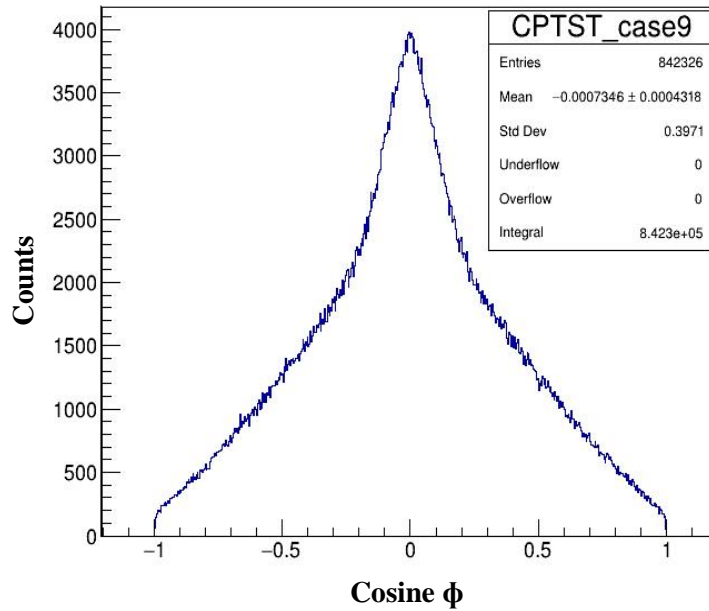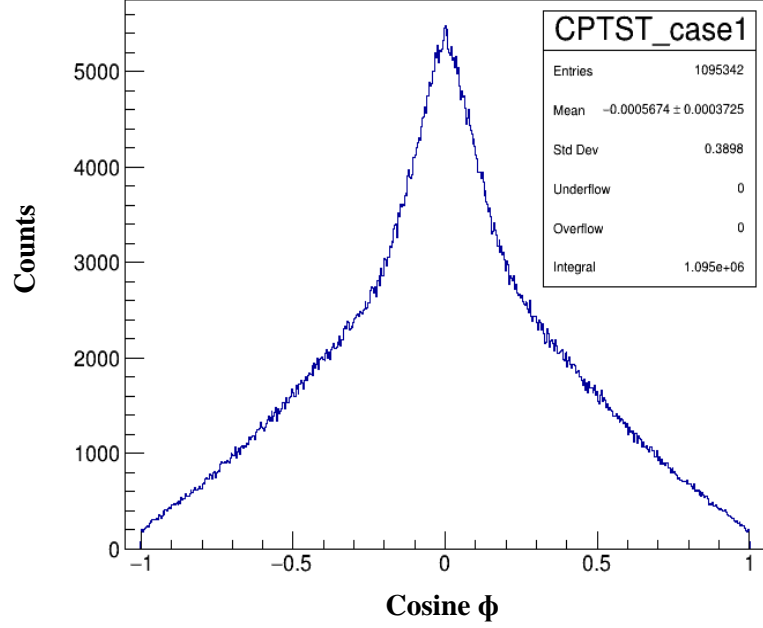
Figure 8.4: The distribution of the $\hat{S} \cdot (\vec{k}_1 \times \vec{k}_2)/|\vec{k}_1 \times \vec{k}_2|$ operator, which is the observable of the CPT symmetry test for the combined results of measurements with the large annihilation chamber.

8.4. Analysis of the systematic uncertainties of the test of CPT symmetry

The sources of systematic uncertainties in such kind of measurements should be carefully considered and discussed. Possible sources of systematic uncertainty comprise the cosmic radiation, non-uniform detector geometry and instability of the setup of the annihilation chamber, radioactive source, and J-PET detector during the whole measurements as well as imprecision of the determination of the angles between the three hits positions for o-Ps decays region with respect to the geometrical center of the J-PET detector, also the determination of the angles between the three hits positions with respect to the location of the annihilation point. The other types of uncertainties, for example those caused by electronic devices instability are much smaller and it can be eliminated. The dominant sources of systematic uncertainty were identified as the influence of cosmic rays during the measurement as well as uncertainty in the positioning of the radioactive source in the detector. The uncertainty of the annihilation chamber geometric center determination was around 1 mm, and from the knowledge of the positron source "positron source-target" was shifted about 6 mm as discussed in Section 7.5.1. In order to investigate the systematic uncertainty due to the variation of the source position, a dedicated study has been performed as discussed in Section 8.4.2.

8.4.1. The systematic uncertainties due to the cosmic rays background

The cosmic radiation can be identified as one of the main sources of the background in our measurements, therefore, a cosmic ray measurement was done to estimate the impact of cosmic radiation recorded during the main measurements. We calculate the cosmic contribution separately for both experiments because the number of true o-Ps

events passing the selection criteria per time of the measurement is different because of using different source activity for each experiment (see Table 8.1).

Table 8.1: Summary of the results for the measurements with large annihilation chamber using two different sources and cosmic rays-only measurement (without source).

Measurements with:	Measurement time (days)	No. Of entries	O_{CPT} mean value	O_{CPT} uncertainty
10 MBq source	9.9	842326	-7.3 x 10^{-4}	4.3 x 10^{-4}
1 MBq source	18.3	253016	-6.8 x 10^{-7}	7.2 x 10^{-4}
cosmic ray	3	10	-0.125	0.1392

The rate of cosmic contribution is the same for both experiments, but the rate of o-Ps events is different, thus the final ratio of cosmic ray events to o-Ps events expected in each experiment is also different.

The upper limit of the contribution of the cosmic events to the systematic error can be calculated as follows:

$$S = \frac{N_{cosmic\_Measurement}}{N_{OPS\_Measurement}} \tag{8.3}$$

where $N_{cosmic\_Measurement}$ is the expected number of cosmic events recorded during the radioactive source measurements which passed the selection criteria, and $N_{OPS\_Measurement}$ is the total number of events obtained with the source.

$$N_{cosmic\_Measurement} = N_{cosmic} * \frac{T_{OPS\_meas.}}{T_{Cosmic\_meas.}} \tag{8.4}$$

where N_{cosmic} is the number of cosmic events in the cosmic measurements (without source) which were done for time $T_{Cosmic\_meas.}$.
$T_{OPS_{meas.}}$ is the time of the measurement with the source.

The O_{CPT} mean value obtained from the 10 cosmic events passing the event selection in the measurement without source is equal to around 1σ (see Figure 8.5). However, because of very low statistics, we decided not to rely on this value and instead calculated the cosmic contribution to the systematic uncertainty assuming a maximum asymmetry (i. e. $\langle 0 \rangle_{cosmic\_meas.} = 1$) in order to obtain a conservative estimation of the systematic effect from cosmic events. As a result, we obtained:

$\sigma_{cosmic}^{syst} = S.\left|\langle 0 \rangle_{cosmic\_meas.}\right| = 1 * 3.9 \text{x} 10^{-5} = 3.9 \text{x} 10^{-5}$

for the measurement with the 10 MBq source and
$\sigma_{cosmic}^{syst} = S.\left|\langle 0 \rangle_{cosmic\_meas.}\right| = 1 * 2.4 \text{x} 10^{-4} = 2.4 \text{x} 10^{-4}$

$\left.\begin{array}{c}\\\\\\\\\\\\\end{array}\right\} \tag{8.5}$

for the measurement with the 1 MBq source.
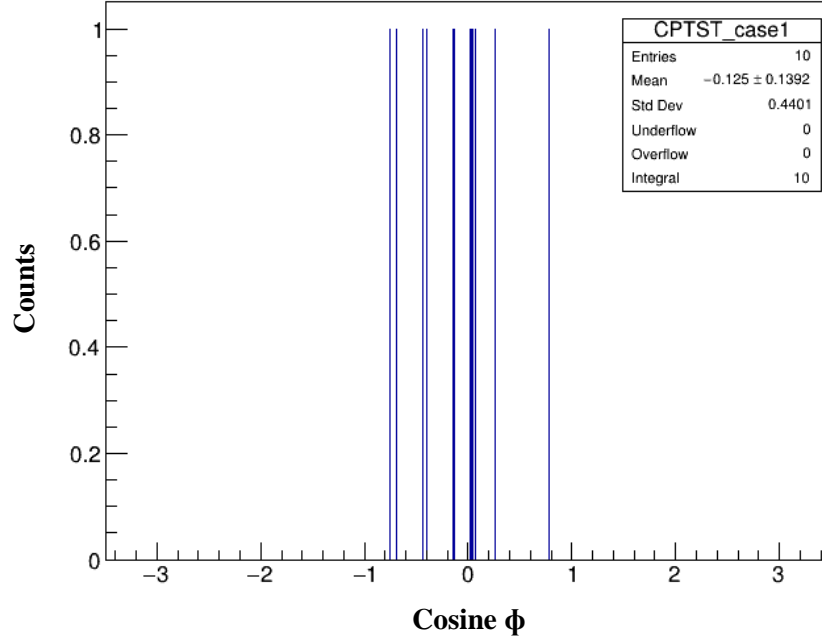
Figure 8.5: The distribution of $\hat{S} \cdot \left(\vec{k}_1 \times \vec{k}_2\right)/\left|\vec{k}_1 \times \vec{k}_2\right|$ operator obtained with cosmic events only (measurements without using a radioactive source) during a 3 days of measurements.

8.4.2. The systematic uncertainty due to the misalignment of the central position of the radioactive source

The another important contribution to the systematic uncertainty is the uncertainty in the positioning of the ^{22}Na source along the z-axis. As discussed in Section 7.5, in the measurement with 10 MBq source the source was shifted by about 0.6 cm along the z-axis with respect to the detector center, which was identified in 2γ images. Although this effect has been taken into account in the analysis of the corresponding data, the impact of possible misalignment along the z-axis was carefully checked.

In order to study the effect of shifted source along z-axis, we reanalyzed the data assuming the source position with an error along z-axis in the range $\pm$ 1 cm with a step of 0.1 cm and checking the $<$O$_{CPT}>$ value resulting from every assumed error in the source z coordinate. Results of such scans for the measurements with 10 MBq and with 1 MBq sources are presented in Tables 8.2 and 8.3 respectively as well as in Figures 8.6 and 8.7. In order to estimate the systematic uncertainty in the final measurement we used the shift of the O$_{CPT}$ mean value for the source position z-axis offset of 3 mm which corresponds to about three times the resolution of the source positioning in our measurements.

In the measurement with 10 MBq source, we discovered that the source was shifted by about 6 mm as shown in Section 7.5.1 (with respect to the center of the detector). However this effect has been taken in to account, even if this effect was not accounted for from the result of the scan presented in Table 8.2 we can see that the possible error would amount to only 4.8 x10^{-6}. Since we knew the actual source position, we only account for the systematic uncertainty from the resolution of the estimation of the

source position which was at the level of 1 mm, so for the possible contribution to the systematic uncertainty, we take the shift of 3 mm with respect to the measured position, which corresponds to about 3 times the resolution of the measured position. Also for the measurement with 1 MBq source, the source position was identified to be shifted by 1 mm which was taken into account. For the systematic uncertainty estimation, we took the difference of the O$_{CPT}$ operator ($\Delta O_{CPT}^{(2)}$) between this position and position shifted by 3 times the resolution.

Table 8.2: Summary of test of influence of the error in β^+ source z position on the final result in the case of the measurements with 10 MBq source.

Shift [cm]	Mean value	Uncertainty	Shift [cm]	Mean value	Uncertainty
0	-7.394 x 10^{-4}	4.333 x 10^{-4}	0	-7.394 x 10^{-4}	4.333 x 10^{-4}
0.1	-7.385 x 10^{-4}	4.338 x 10^{-4}	-0.1	-7.378 x 10^{-4}	4.325 x 10^{-4}
0.2	-7.400 x 10^{-4}	4.344 x 10^{-4}	-0.2	-7.384 x 10^{-4}	4.322 x 10^{-4}
0.3	-7.403 x 10^{-4}	4.351 x 10^{-4}	-0.3	-7.370 x 10^{-4}	4.320 x 10^{-4}
0.4	-7.406 x 10^{-4}	4.359 x 10^{-4}	-0.4	-7.363 x 10^{-4}	4.319 x 10^{-4}
0.5	-7.411 x 10^{-4}	4.362 x 10^{-4}	-0.5	-7.354 x 10^{-4}	4.321 x 10^{-4}
0.6	-7.413 x 10^{-4}	4.379 x 10^{-4}	-0.6	-7.346 x 10^{-4}	4.318 x 10^{-4}
0.7	-7.412 x 10^{-4}	4.384 x 10^{-4}	-0.7	-7.348 x 10^{-4}	4.319 x 10^{-4}
0.8	-7.415 x 10^{-4}	4.398 x 10^{-4}	-0.8	-7.351 x 10^{-4}	4.326 x 10^{-4}
0.9	-7.417 x 10^{-4}	4.407 x 10^{-4}	-0.9	-7.363 x 10^{-4}	4.330 x 10^{-4}
1	-7.423 x 10^{-4}	4.414 x 10^{-4}	-1	-7.375 x 10^{-4}	4.332 x 10^{-4}

Figure 8.6: The change of the mean value and the uncertainty of the distribution of the operator $\hat{S} \cdot (\vec{k}_1 \times \vec{k}_2)/|\vec{k}_1 \times \vec{k}_2|$ as a function of an assumed error in the position of the 10 MBq radioactive source in the range ± 1 cm along the z-axis.

In the case of shift 3mm along z-axis, the tested O_{CPT} mean value offset $\Delta O_{CPT}^{(1)}$ of the result using 10 MBq radioactive source is:

$$\Delta O_{CPT}^{(1)} = |\langle 0 \rangle_m - \langle 0 \rangle_s| = 1.70 \times 10^{-6}$$

where: $\langle 0 \rangle_m$ and $\langle 0 \rangle_s$ is O_{CPT} mean value for the measured central position and 3 mm shifted position respectively. Also the change of the O_{CPT} mean value result using 1 MBq radioactive source is:

$$\Delta O_{CPT}^{(2)} = |\langle 0 \rangle_m - \langle 0 \rangle_s| = 1.91 \times 10^{-5}$$

(8.6)

Table 8.3: Summary of test of influence of the error in β^+ source z position on the final result in the case of the measurements with 1 MBq source.

Shift [cm]	Mean value	Uncertainty	Shift [cm]	Mean value	Uncertainty
0	5.005×10^{-6}	7.205×10^{-4}	0	5.005×10^{-6}	7.205×10^{-4}
0.1	-6.775×10^{-7}	7.204×10^{-4}	-0.1	1.084×10^{-5}	7.207×10^{-4}
0.2	-9.029×10^{-6}	7.206×10^{-4}	-0.2	1.584×10^{-5}	7.212×10^{-4}
0.3	-1.007×10^{-5}	7.209×10^{-4}	-0.3	2.211×10^{-5}	7.219×10^{-4}
0.4	-1.979×10^{-5}	7.215×10^{-4}	-0.4	2.884×10^{-5}	7.227×10^{-4}
0.5	-2.219×10^{-5}	7.222×10^{-4}	-0.5	3.611×10^{-5}	7.238×10^{-4}
0.6	-2.555×10^{-5}	7.232×10^{-4}	-0.6	4.234×10^{-5}	7.251×10^{-4}
0.7	-3.499×10^{-5}	7.244×10^{-4}	-0.7	4.733×10^{-5}	7.266×10^{-4}
0.8	-3.654×10^{-5}	7.257×10^{-4}	-0.8	5.398×10^{-5}	7.282×10^{-4}
0.9	-4.317×10^{-5}	7.273×10^{-4}	-0.9	6.385×10^{-5}	7.301×10^{-4}
1	-4.877×10^{-5}	7.291×10^{-4}	-1	6.968×10^{-5}	7.322×10^{-4}

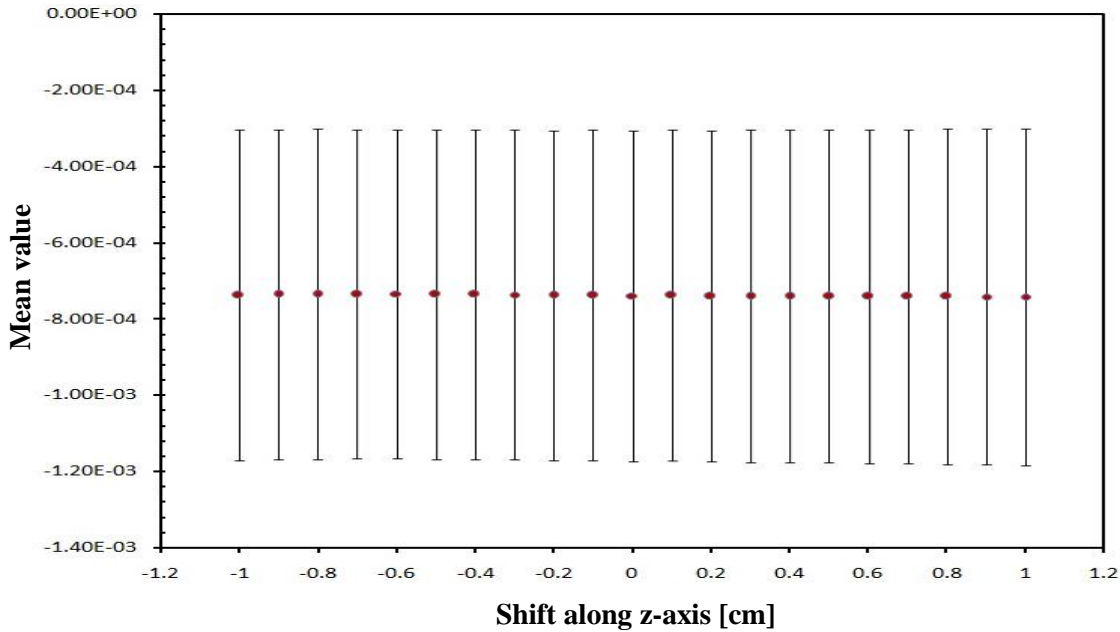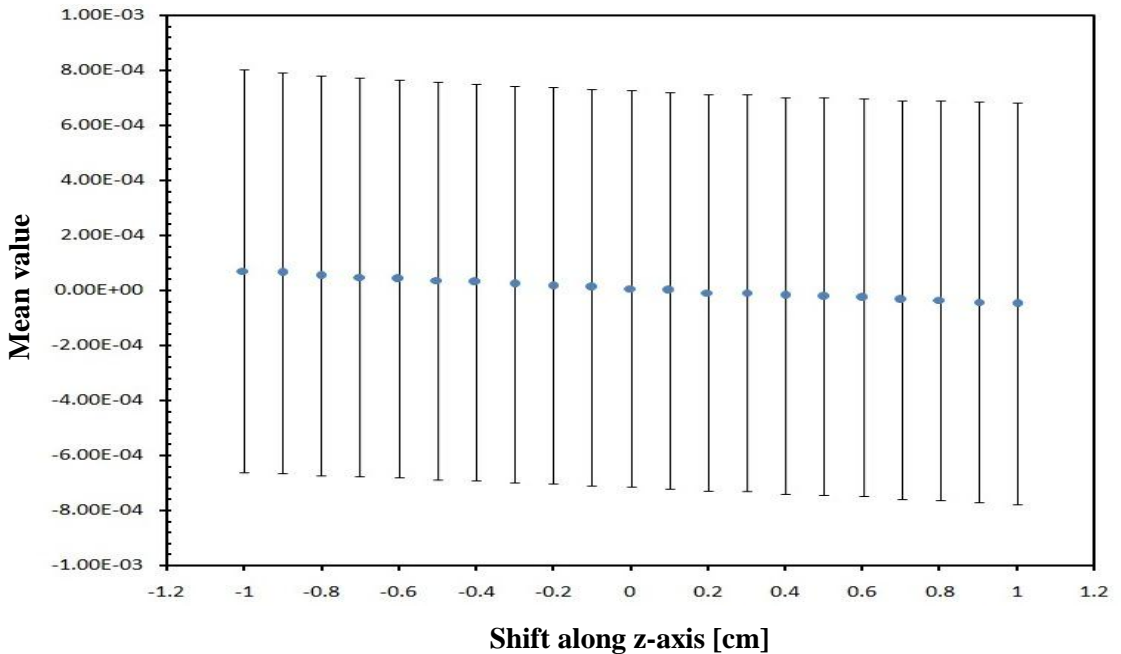Figure 8.7: The change of the mean value and the uncertainty of the distribution of the operator $\hat{S} \cdot (\vec{k}_1 \times \vec{k}_2)/|\vec{k}_1 \times \vec{k}_2|$ as a function of an assumed error in the position of the 1 MBq radioactive source in the range ± 1 cm along the z-axis.

8.4.3. Study the symmetry of the geometry of J-PET detector

The rotational symmetry of the J-PET detector and the positronium production setup used in the measurements, combined with recording a broad range of geometrical configurations of o-Ps→3γ events at the same time, is expected to cancel out possible false geometrical asymmetries to a large extent.

In order to validate this assumption, we are checking the distribution of another angular correlation operator defined as:

$$O_{CP} = \frac{\vec{S}\cdot\vec{k}_1}{|\vec{S}\cdot\vec{k}_1|} \cdot \frac{\vec{S}\cdot(\vec{k}_1\times\vec{k}_2)}{|\vec{S}|\cdot|\vec{k}_1\times\vec{k}_2|} = (\hat{S}\cdot\hat{k}_1)\left(\hat{S}\cdot\left(\frac{\vec{k}_1\times\vec{k}_2}{|\vec{k}_1\times\vec{k}_2|}\right)\right) \tag{8.7}$$

This operator would be sensitive to CP-violating effects in the presence of specific tensor polarization of ortho-positronium. However, as such tensor polarization could only be produced using an external magnetic field, we do not expect to see any physical asymmetries in the distribution of this operator in our current measurements without a magnetic field. Therefore, any asymmetries manifested in the O_{cp} distribution must come only from the detector geometry and analysis efficiency.

The distributions of O_{CP} operator which were used as a cross-check for false symmetries via O_{CP} operator are shown in Figures 8.8 and 8.9 for the measurements with a large annihilation chamber using 1 MBq source and 10 MBq source respectively, also Figure 8.10 shows the combined results of both measurements.
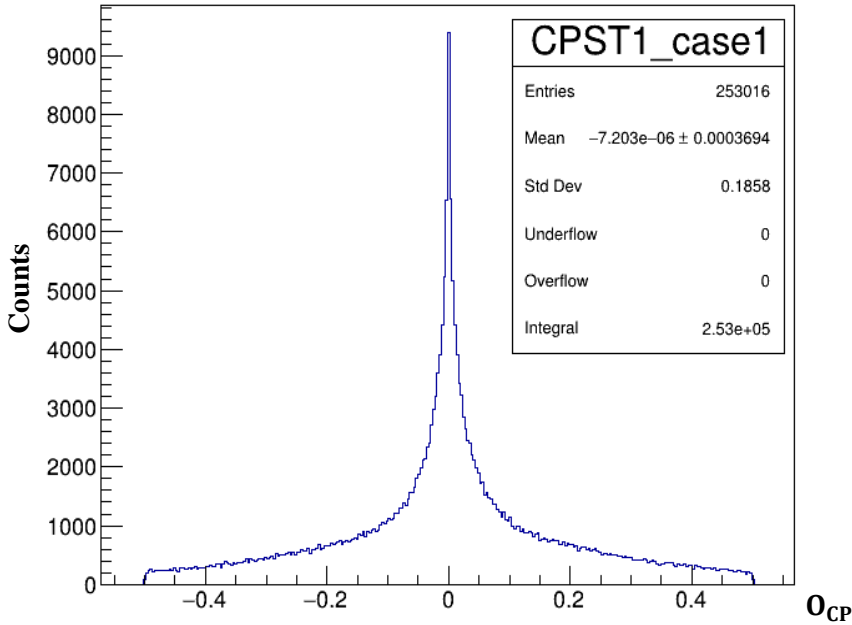
Figure 8.8: The distribution of O_{CP} operator, used as a cross-check for false symmetries for the measurements with large annihilation chamber using 1 MBq source.
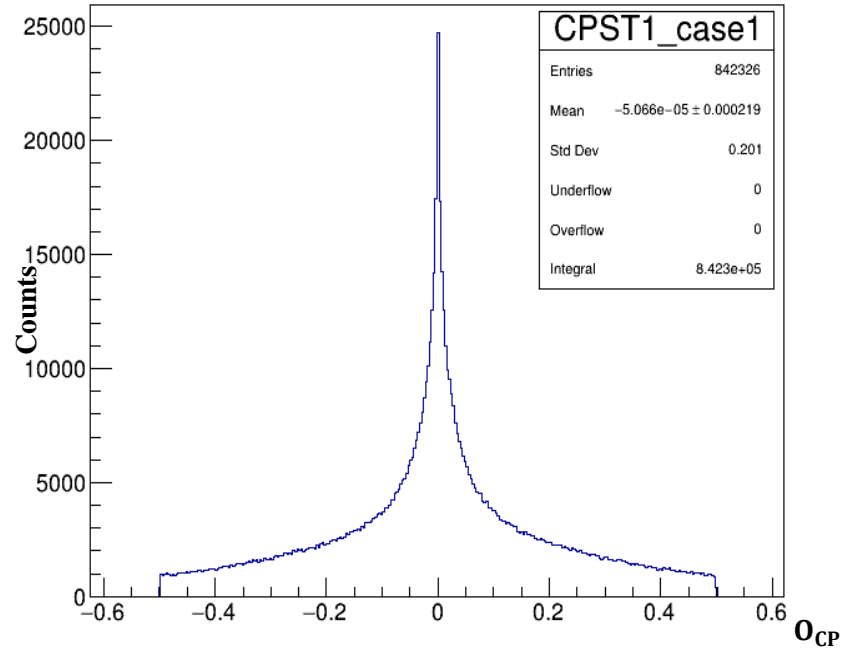
Figure 8.9: The distribution of O_{CP} operator, used as a cross-check for false symmetries for the measurements with a large annihilation chamber using 10 MBq source.
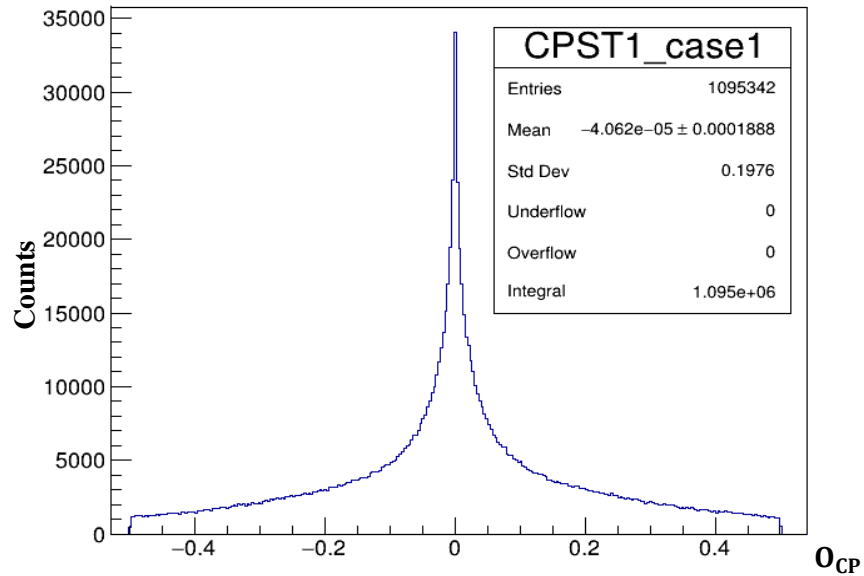
Figure 8.10: The distribution of O_{CP} operator, used as a cross-check for false symmetries for the combined results of measurements with a large annihilation chamber.

The expectation values of the O_{CP} operators are well consistent with zero within their statistical uncertainty (at the level of 2×10^{-4}), therefore, no significant effects from the J-PET detector geometry are expected in the measurements of O_{CPT}.

8.4.4. The comparison of systematic effects with respect to the previous experiments

The decrease in the decay rate of the ^{22}Na source ($T_{1/2}$ = 2.6 yr) was one of the predominant sources of uncertainty in the previous experiments. The deceasing of the radioactivity of ^{22}Na is not a source of systematic uncertainty in our experiment, because we are not changing anything of the setup during the whole measurements. The ^{22}Na radioactive source activity is decreasing, but in the meantime, there was no change in the geometry which could cause asymmetry, which can be considered as an advantage of the J-PET detector with respect to the previous experiments [**3**]. In that case, the authors had to perform the measurements using a given direction of the magnetic field, so they made the measurements for certain time when the magnetic field was oriented up, and then repeated the measurements for the same time with inversed magnetic field (down) to cancel out possible systematic effects related to the magnetic field generation setup, but since the source was more active in the first measurement comparing to the 2nd part of the measurements, the number of events was higher which could result in artificial asymmetry. In case of measurements described in this work, this is not a problem, since we do not perform measurements with magnetic field, therefore there is no distinguished direction in our measurements. Instead, the J-PET detector is recording the broad range of possible orientations between the decay plane and the o-Ps spin as well as possible orientations of both with respect to the detector. This results in the cancellation of many false asymmetry effects due to the geometry of the setup, as demonstrated in the previous section.

8.4.5. The combined result of both measurements

The estimates of the various types of systematic uncertainty for both measurements studied in this work are summarized in Table 8.4.

Table 8.4: The various types of systematic uncertainty contributions in the two studied J-PET measurements.

Source of systematic uncertainty	Measurements with 10 MBq source	Measurements with 1 MBq source
The cosmic background	3.93 x10^{-5}	2.41 x10^{-4}
The source alignment at the center	1.70 x10^{-6}	1.91 x10^{-5}
Total systematic uncertainty	3.93 x10^{-5}	2.41 x10^{-4}
The statistical uncertainty	4.31 x10^{-4}	7.20 x10^{-4}
Total uncertainty	4.33 x10^{-4}	7.59 x10^{-4}

The systematic uncertainties discussed above are regarded as independent contributions such that the total systematic uncertainty can be estimated as their quadratic sum.

The results of both measurements presented in Table 8.4 were combined to obtain an average value of <O$_{CPT}$> weighted by total uncertainty of each measurement.
The weighted average and its uncertainty based on both sets of measurements can be obtained as:

$$\langle\overline{O_{CPT}}\rangle = \frac{\langle O_{CPT}^{(1)}\rangle\,\omega_1 + \langle O_{CPT}^{(2)}\rangle\,\omega_2}{\omega_1 + \omega_2} \tag{8.8}$$

$$S_{\langle\overline{O_{CPT}}\rangle} = (\omega_1 + \omega_2)^{-1/2}$$

where:

$$\left.\begin{aligned}
\omega_1 &= \frac{1}{S^2\!\left(\langle O_{CPT}^{(1)}\rangle\right)} \\[1em]
\omega_2 &= \frac{1}{S^2\!\left(\langle O_{CPT}^{(2)}\rangle\right)}
\end{aligned}\right\} \tag{8.9}$$

ω_1 and ω_2 are the weights for 1st measurement and 2nd measurement respectively, $\langle O_{CPT}^{(1)}\rangle$ and $\langle O_{CPT}^{(2)}\rangle$ are the mean values for 1st measurement and 2nd measurement respectively.
$S\langle O_{CPT}^{(1)}\rangle$, $S\langle O_{CPT}^{(2)}\rangle$ denote the total uncertainty (variance of the distribution of the CPT operator) for 1st measurement and 2nd measurement respectively.

The weighted average of the mean value and the total uncertainty for the combined both sets of the measurements reads:

$$\langle\overline{O_{CPT}}\rangle = (-5.5 \pm 3.7) \times 10^{-4} \tag{8.10}$$

8.5. The calculation of the CPT violation coefficient (C$_{CPT}$)

The Gammasphere [5] was the only experiment to date which performed a CPT-test by measuring the whole angular dependence and not only the competition between up and down alignments, where the other experiments for the previous CPT and also CP test measurements include only a comparison of the number of configurations of up and down alignments. Therefore, it was the first study were the Monte Carlo simulation where used to extract the CPT violation for efficiency. As we also determine the distribution of the angular correlation operator, in order to extract the CPT violation coefficient from the measurements presented in this thesis, use of Monte Carlo simulations of CPT-odd signal would be preferred in a similar manner. To properly account for the geometrical efficiency of the detector as well as efficiency of the event selection, high level of consistency between the MC simulations and the experimental setup must be ensured. As of writing of this thesis, the Monte Carlo simulations of the J-PET detector are still under elaboration, therefore we decided to present and draw conclusions from the raw experimental result. It should be noted, however, that despite the absence of precise description of the detector and analysis

efficiencies, these are expected to be symmetric functions of O_{CPT} which is confirmed by preliminary tests done with the MC simulations.

In the previous experiments the asymmetry was defined as a difference between the number of up and down configurations over the sum of them.

This is a special case of the expectation value, because if we have an operator which have only two possible values +1/-1, then the expectation value is reduced to:

$$\langle \overline{O_{CPT}} \rangle = \frac{N_+ \cdot (+1) + N_- \cdot (-1)}{N_+ + N_-} \tag{8.11}$$

In the previous experiments, the measurements of the above asymmetry were corrected for the analyzing power mostly dominated by the polarization which is also the case in the J-PET experiment.

If the degree of true CPT violation effect in the data is quantized with the C_{CPT} coefficient, the analyzing power Ap accounts for the ability to observe this effect through measurement of the asymmetry (A):

$$A = Ap * C_{CPT} \tag{8.12}$$

In our case we can use the expectation value of the C_{CPT} operator which was calculated in (8.10), since it is equivalent to the asymmetry *(A)* in equation (8.12). Given that the analyzing power Ap in our measurements is dominated by the average polarization (calculated in Equation (3.1)), we can extract the CPT-violation parameter as follows:

$$C_{CPT} = \frac{A}{P} \equiv \frac{\langle \overline{O_{CPT}} \rangle}{P} \tag{8.13}$$

Thus, the CPT violation coefficient determined for the measurements described in this thesis reads:

$$C_{CPT} = \frac{A}{P} = (-13.6 \pm 9.2) \times 10^{-4} \tag{8.14}$$

This is consistent with the hypothesis of no CPT violation in the examined process. In terms of sensitivity of the symmetry test, it is improving the best measurment to date (3.1×10^{-3} [5]) by more than a factor of 3, and it is the first measurement with the sensitivity going beyond the level of 10^{-3}.

9. Conclusions and perspectives

9.1. Conclusions

As the lightest system consisting purely of charged leptons, positronium is viable to search for new effects not included in the Standard Model in the leptonic sector. The discrete symmetries can be tested by searching for the forbidden decays of positronium atom, e.g. p-Ps→3ɣ decay, or by measurement of the expectation values of symmetry-odd operators.

The aim of this thesis was to test the CPT symmetry by searching for the possible non-zero expectation values of the operator $O_{CPT} = \hat{S} \cdot (\vec{k}_1 \times \vec{k}_2)/|\vec{k}_1 \times \vec{k}_2| = \cos\phi$, in the o-Ps→3ɣ annihilations, where $\hat{S}$ is the spin unit vector of the o-Ps atom, and $\vec{k}_1$, $\vec{k}_2$ are momenta of the most energetic o-Ps decay photons, and ϕ is the angle between the o-Ps spin and the normal to the photons decay plane.

Determining the value of this operator is equivalent to measuring the angular correlation between the spin of the o-Ps atom and the normal to the decay plane of o-Ps→3ɣ. The experiment was performed using the J-PET detector at the Jagiellonian University. The experiment was done using the large annihilation chamber for a set of measurements dedicated to the identification and reconstruction of the 3ɣ events from o-Ps decay. This chamber together with silica R60G as a porous material target on the internal surface wall of the chamber and using the reconstruction method for the annihilation points on the chamber allowed us to estimate the spin of o-Ps atoms on an event-by-event basis. From these measurements, we determined the mean value of the CPT-sensitive angular correlation operator $\langle \overline{O_{CPT}} \rangle = (-5.5 \pm 3.7) \times 10^{-4}$, which corresponds to the CPT violation coefficient of $C_{CPT} = (-13.6 \pm 9.2) \times 10^{-4}$.

The result is consistent with zero, where no violation has been found at the precision level of 9.2×10^{-4}, which is more than a factor of 3 better than the previous experimental results (The best previous result obtained by the Gammasphere experiment resulted in $(2.6 \pm 3.1) \times 10^{-3}$ [5]).

We have demonstrated that the J-PET detector with its present setup is able to test discrete symmetries in the charged leptonic system with higher sensitivity than all the published results to date.

The possible improvement of precision of the CPT test achievable with the same dataset could be obtained e.g. by using the kinematic fit discussed in Section 7.6.2 which should not only improve the angular resolution of the spin direction estimation and thus the level of average polarization but also better resolution of the annihilation point should increase performance of several cuts used in the analysis which rely on the annihilation point determination. Therefore, both average o-Ps polarization and signal selection efficiency could be improved as a result of the kinematic fit.

The efficiency of the analysis could also be improved by lowering the TOT window used to identify candidates for annihilation photon interactions (see Figure 7.10) provided that additional selection criteria can be devised to discriminate the scattered photons abundant in the low-TOT region.

In the future J-PET experiments, statistical uncertainty can be easily reduced by extending the measurements. Moreover, in the near future, two upgrades to the setup are planned [62,105] which will increase the rate of recorded o-Ps→3ɣ events. Next Section gives an overview of the planned setup upgrades.

9.2. The perspectives

The uncertainty of the measurement of CPT-violation sensitive operator O_{CPT} depends on the number of reconstructed o-Ps decays and the accuracy of o-Ps spin measurements. Using a cylindrical positronium production chamber and porous silica R60G as a target material, about 10^6 decay points of o-Ps into 3 photons were recorded and reconstructed after 3 months of continuous measurement.

In the future measurements, this figure can be improved by either increasing the detector efficiency for recording complete three-photon annihilations or by enhancing the rate of produced o-Ps→3ɣ events. The former can be obtained by use of an additional layer of scintillators with higher acceptance, whereas the latter is achievable with a new annihilation chamber which allows for more positrons forming o-Ps and their 3ɣ annihilation can be recorded in the most sensitive region of the J-PET detector.

In the next set of measurements, the annihilation chamber will be realized as the positron source with a porous material sphere around it, where we plan to use porous target materials on the internal surface of the sphere chamber inside an additional cylindrical chamber. Once a spherical chamber with o-Ps production medium is included in the setup of the new chamber, the yield of 3 annihilations is expected to be significantly increased, due to the higher probability of positrons interacting in the porous layer and due to the fact than all of the porous target will be contained within the detector region where the efficiency of recording 3ɣ events is highest.

Regardless of the ability for long measurements with a high activity source, the J-PET detector will be upgraded by an additional layer of plastic scintillators modules with advanced signal reconstruction methods. This detection layer have been recently prepared and tested to be implemented to the J-PET detector prototype and their inclusion in the future experiments would provide more precision enhancement to the measurement results. The fourth layer of detectors modules is read out by a silicon photomultipliers (SiPM) and will provide almost full coverage acceptance in azimuthal angle and provide more resolution enhancement to the final results. The CPT symmetry operator can be investigated at J-PET more precisely taking advantages of the additional layer of detectors.

The improvement can also performed by reducing the systematic uncertainties by improved resolution with SiPM's which will be included in the additional digital layer. The influence of the cosmic rays was found to be a significant source of systematic uncertainty and it was described as one of the main sources of the background in our measurements, therefore a cosmic ray veto detector is being designed in order to use it in the J-PET future experiments.

Acknowledgments

First of all, I would like to express my sincerest gratitude to my supervisor Prof. Dr. hab. Paweł Moskal for giving me the opportunity to work within his research group, for sharing his vast knowledge and experience and motivating guidance.

I convey my special thanks to my co-supervisor Dr. Aleksander Gajos for his valuable advice, his support and guidance during the preparation of this thesis.

I want to thank professors from Jagiellonian University who provided interesting courses that I attended in the frame of the Ph.D studies program: Prof. Dr. hab. Józef Spałek, Prof. Dr. hab. Piotr Salabura, Prof. Dr. hab. Elżbieta Richter-Wąs, and Dr. hab. Adam Rycerz.

I would also express my deepest gratitude to my colleagues, Dr. Eryk Czerwiński, Dr. Michal Silarski, Dr. Wojciech Krzemień, and Dr. Grzegorz Korcyl for their suggestions and remarks during our group meetings.

I also thank my colleagues: Dr. Tomasz Bednarski, Dr. Szymon Niedźwiecki for letting me a hand with many challenges I have met during my work in our laboratory.

I also thank my colleagues: Dr. Magdalena Skurzok, Dr. Łukasz Kapłon, Dr. Daria Kisielewska, Dr. Marek Gorgol, Monika Pawlik-Niedźwiecka, Dr. Sushil Sharma, Dr. Raffaele Del Grande, Kamil Dulski, Ewelina Kubicz, Kamil Rakoczy, Nikodem Krawczyk, Dominika Alfs, Juhi Raj, Shivani Choudhary, and Krzysztof Kacprzak because each of them contributed something to this work as well.

I would express my appreciation to Mr. Wojciech Migdał for helping me with experimental details and showing me how to solve the technical problems easily.

I also would like to thank my friends particularly, Dr. Kacper Topolnicki, Dr. Damian Gil, Thomas Williams, and Krzysztof Nowakowski for their friendship and emotional support through all these last years.

Finally, I wish to thank my parents and the rest of my family for their love, my wife and my children for their endless patience and infinite support not only with this thesis but throughout my entire life.
Thanks once more to all the people listed here, this Ph.D thesis would not be existing without them.

Bibliography

[1] B. Aubert et al., Phys. Rev. Lett. 87, 091801 (2001).

[2] B. Grinstein, R. Soo-Jong, and B. Wise Mark, Phys. Rev. D 33, 1495 (1986).

[3] T. Yamazaki et al., Phys. Rev. Lett. 104, 083401 (2010).

[4] W. Bernreuther et al., Z. Phys. C 41, 143 (1988).

[5] P. A. Vetter and S. J. Freedman, Phys. Rev. Lett. 91, 263401 (2003).

[6] B. K. Arbic et al., Phys. Rev. A 37, 3189 (1988).

[7] P. Moskal,... , M. Mohammed et al., Acta Phys. Polon. B 47, 509 (2016).

[8] C. S. Wu et al., Phys. Rev. 105, 1413 (1957).

[9] R. L. Garwin et al., Phys. Rev. 105, 1415 (1957).

[10] J. P. Lees et al., Phys.Rev.Lett. 109, 211801 (2012).

[11] E. Bellotti et al., Physics Letters B 124, 435 (1983).

[12] C. N. Yang, Physical Review 77, 242 (1950).

[13] Y. C. Jean, D. M. Schrader and P. E. Mallon, "Principles and Applications of Positron and Positronium Chemistry". World Scientific Publishing Co Inc (2003).

[14] M. Eldrup, D. Lightbody, and J. N. Sherwood, Chemical Physics. 63, 51 (1981).

[15] M. Deutsch, Phys. Rev. 82, 455 (1951).

[16] G. S. Adkins, R. N. Fell, and J. Sapirstein, Annals of Physics 295, 136 (2002).

[17] S. G. Karshenboim, Int. J. Mod. Phys. A 19, 3879-3896 (2004).

[18] D. B. Cassidy, Eur. Phys. J. D 72, 3, 53 (2018).

[19] S. D. Bass, Acta Phys. Polon. B50, 7, 1319 (2019).

[20] A. H. Al-Ramadhan and D. W. Gidley, Phys. Rev. Lett. 72, 1632 (1994).

[21] I. B. Khriplovich, and A. S. Yelkhovsky, Phys. Lett. B 246, 520 (1990).

[22] R. S. Vallery, P. W. Zitzewitz, and D. W. Gidley, Physical Review Letters 90, 20 (2003).

[23] G. S. Adkins, Physical Review A 72, 032501 (2005).

[24] A. Czarnecki, K. Melnikov, and A. Yelkhowsky, Phys. Rev. Lett. 83, 1135 (1999).

[25] S. G. Karshenboim, Zh. Eksp. Teor. Fiz. 103, 1105-1117 (1993).

[26] G. S. Adkins, and F. R. Brown, Phys. Rev. A28, 1164 (1983).

[27] A. Ore and J. L. Powell, Phys. Rev. 75, 1696 (1949).

[28] G. P. Lepage et al., Phys. Rev. A28, 3090 (1983).

[29] A. Vértes, S. Nagy, and Z. Klencsár, "Handbook of Nuclear Chemistry", Volume 3 Kluwer Academic Publishers (2003).

[30] C. G. Fischer et al., Phys. Rev. B 71, 18, 180102 (2005).

[31] B. Blomquist, B. Helgee, and F. H. Maurer, Chem. Phys. 202, 2742 (2001).

[32] J. McGervey and S. DeBenedetti, Phys. Rev. 114, 495 (1959).

[33] Z. A. Qiao et al., Journal de Physique IV, 3, 105 (1993).

[34] P. Hedvig, "Experimental Quantum Chemistry", Academic Press (1975).

[35] M. Charlton, and J. W. Humberston, "Positron Physics", Cambridge University Press, (2000).

[36] Y. Nagashima, Physics Reports 545, 3, 95 (2014).

[37] S. V. Stepanov et al., Journal of Physics Conference Series, 618 (1) 012003 (2015).

[38] J. Mitroy, and S. A. Novikov, Phys. Rev. Lett. 90, 183202 (2003).

[39] O. Halpern, Phys. Rev. 94, 904 (1954).

[40] S. Rochanakij, and D. M. Schrader, Radiat. Phys. Chem. 32, 557 (1988).

[41] D. B. Cassidy, V. E. Meligne, and A. P. Mills Jr, Phys. Rev. Lett. 104, 17, 173401 (2010).

[42] V. Vanyashin, Letters in Mathematical Physics 31, 143-149 (1994).

[43] H. K. Avetissian, A. K. Avetissian, and G. F. Mkrtchian, Phys. Rev. Lett. 113, 023904 (2014).

[44] D. B. Cassidy, and A. P. Mills Jr, Physica Status Solidi C 4, 10, 3419-3428 (2007).

[45] M. Mohammed et al., Acta Phys. Polon. A 132, 5, 1486 (2017).

[46] A. Gajos,... , M. Mohammed et al., Nucl. Inst. and Meth. A819, 54 (2016).

[47] A. Gajos, "A novel algorithm for the K->pi0pi0->gggg decay vertex reconstruction for the KLOE-2 experiment", Diploma thesis, Jagiellonian University in Krakow, Poland (2013).

[48] P. Coleman, "Positron Beams and Their Applications", World Scientific, (2000).

[49] J. Yang et al., Jpn. J. Appl. Phys. 36, 3764 (1997).

[50] P. Moskal,... , M. Mohammed et al., Eur. Phys. J. C 78, 970 (2018).

[51] D. Kaminska,... , M. Mohammed et al., Eur. Phys. J. C 76, 8, 445 (2016).

[52] M. Felcini, Int. J. Mod. Phys. A19, 3853-3864 (2004).

[53] M. Maekawa et al., Journal of Physics: Conference Series 505, 012033 (2014).

[54] R. Ley, Applied Surface Science 194, Issues 1–4, 301-306 (2002).

[55] S. M. Curry, R. Cubeddu, and T. W. Hänsch, Applied physics 1, 153–159 (1973).

[56] K. F. Canter, P. G. Coleman, T.C. Griffith, and G. R. Heyland, J. Phys. B 5, L167 (1972).

[57] N. F. Mott, Proc. Roy. Soc. A135 429-458 (1932).

[58] J. Van House and P. W. Zitzewitz, Phys. Rev. A 29, 96 (1984).

[59] W. Bernreuther and O. Nachtmann, Z. Phys. C 11, 235-245 (1981).

[60] B. C. Hiesmayr and P. Moskal, Scientific Reports 7, 15349 (2017).

[61] B. C. Hiesmayr and P. Moskal, Scientific Reports 9, 8166 (2019).

[62] P. Moskal,... , M. Mohammed et al., Phys. Med. Biol. 64, 055017 (2019).

[63] P. Moskal et al., Nature Reviews Physics 1, 527-529 (2019).

[64] P. J. Slomka et al., Semin. Nucl. Med. 46, 5–19 (2016).

[65] N. N. Shehad et al., IEEE 2005 Nuclear Science Symposium Conference Record 5, 2895 (2005).

[66] L. Sun et al., IEEE 2007 Nuclear Science Symposium Conference Record 5, 3337 (2007).

[67] A. Blanco et al., IEEE Trans. Nucl. Sci. 53, 2489 (2006).

[68] S. J. Park et al., Nucl. Instrum. Methods A 570, 543–555 (2007).

[69] T. Doke et al., Nucl. Instrum. Methods A 569, 863–871 (2006).

[70] P. Moskal et al., Bio-Algorithms Med. Syst. 7, 73 (2011).

[71] P. Moskal et al., Nucl. Instrum. Methods A 775, 54 (2015).

[72] M. Pałka et al., Bio-Algorithms and Med-Systems 10, 41 (2014).

[73] P. Moskal et al., Nucl. Instrum. Methods A 764, 317 (2014).

[74] M. Palka,... , M. Mohammed et al., JINST 12, P08001 (2017).

[75] Ł. Kapłon, "Synthesis and characterization of polystyrene scintillators and their application in positron emission tomography", PhD thesis, Jagiellonian University in Krakow, Poland (2018).

[76] S. Niedzwiecki, "Double-strip prototype of polymer time-of-flight positron emission tomograph based on multi-level analog electronics", PhD thesis, Jagiellonian University in Krakow, Poland (2019).

[77] A. Strzelecki, "Image reconstruction and simulation of strip Positron Emission Tomography scanner using computational accelerators ", PhD thesis, Jagiellonian University in Krakow, Poland (2016).

[78] T. Hakamata et al., "Photomultiplier Tubes Basics and Applications", 3rd edition, Hamamatsu Photonics, Tokyo-Japan (2007).

[79] G. F. Knoll, "Radiation Detection and Measurement", 4th edition, John Wiley & Sons (2010).

[80] D. Bailey, Positron Emission Tomography Basic Sciences, Springer (2005).

[81] S. Niedźwiecki,... , M. Mohammed et al., Acta Physica Polonica B 48, 1567 (2017).

[82] G. Korcyl,... , M. Mohammed et al., IEEE Transactions On Medical Imaging 37, 11, 2526 (2018).

[83] W. Krzemien et al., Acta Phys. Polon. A 127, 1491 (2015).

[84] P. Bialas et al., Acta Phys. Polon. B Proceed. Suppl. 6, 1027 (2013).

[85] P. Bialas et al., Bio-Algorithms and Med-Systems 10, 9 (2014).

[86] A. P. Dempster et al., Journal of the Royal Statistical Society, Series B (methodological), 1 (1977).

[87] G. McLachlan and T. Krishnan, "The EM algorithm and extensions", John Wiley & Sons (1996).

[88] M. Conti, Physica Medica, 25, 1-11 (2009).

[89] The annihilation chambers and the radioactive sources were constructed at Maria Curie-Skłodowska University in Lublin, Poland, by the group of Prof. B. Jasinska, Dr. J. Wawryszczuk, and M. Gorgol. The details of the sources and chambers based on private communication (2018).

[90] R. Ferragut et al., Journal of Physics: Conference Series 262, 012020 (2011).

[91] R. Nagarale, A. Heller, and W. Shinb, Journal of The Electrochemical Society 159 (1)14-17 (2012).

[92] N. Koshida, "Device Applications of Silicon Nanocrystals and Nanostructures", Springer (2009).

[93] C. Hugenschmidt, Positron sources and positron beams, Proceedings of the International School of Physics, Enrico Fermi, Course CLXXIV, Physics with Many Positrons, Bologna, Italy, July 7-17 (2009).

[94] Z. A. Qiao et al., Chem. Mater., 21, 3823–3829 (2009).

[95] E. Kubicz,... , M. Mohammed et al., Acta Phys. Polon. B 47, 537 (2016).

[96] K. Dulski et al., Acta Phys. Pol. B 51, 1, 195 (2020).

[97] G. Korcyl,... , M. Mohammed et al., Acta Phys. Polon. B47 (2016).

[98] F. Gonnella et al., Nucl. Instrum. Meth. A791, 16-21 (2015).

[99] K. Shimazoe et al., IEEE Transactions on Nuclear Science, 59, 6 (2012).

[100] M. Pawlik-Niedzwiecka,... , M. Mohammed et al., Acta Phys. Polon. A 132, 1645–1648 (2017).

[101] M. Mohammed and A. Gajos, EPJ Web Conf. 199, 05027 (2019).

[102] B. Jasinska,... , M. Mohammed et al., Acta Phys. Pol. B 47, 453 (2016).

[103] D. Kamińska et al., Nukleonika 60, 729-732 (2015).

[104] P. W. Zitzewitz et al., Phys. Rev. Lett. 43, 1281–1284 (1979).

[105] L. Raczynski,... , M. Mohammed et al., Phys. Med. Biol. 62, 5076 (2017).